Title
Solar energy storage through the homogeneous electrocatalytic reduction of carbon dioxide : photoelectrochemical and photovoltaic approaches

Permalink
https://escholarship.org/uc/item/23k9v8zv

Author
Sathrum, Aaron John

Publication Date
2011

Peer reviewed|Thesis/dissertation

UNIVERSITY OF CALIFORNIA, SAN DIEGO

Solar Energy Storage through the Homogeneous Electrocatalytic Reduction of Carbon Dioxide: Photoelectrochemical and Photovoltaic Approaches

A dissertation submitted in partial satisfaction of the requirements

for the degree of Doctor of Philosophy

in

Materials Science and Engineering

by

Aaron John Sathrum

Committee in charge:

Professor Clifford P. Kubiak, Chair
Professor Peter M. Asbeck
Professor Prabhakar R. Bandaru
Professor Michael J. Tauber
Professor Paul K. L. Yu

2011

The dissertation of Aaron John Sathrum is approved, and it is acceptable in quality and form for publication on microfilm and electronically:

_____

_____

_____

_____

_____

Chair

University of California, San Diego

2011

iii

DEDICATION

To Jesus Christ, my Lord and Savior: for his faithfulness and guidance in my life.

To my loving wife Jenny: for her support, forgiveness, and encouragement. Her gentleness, smile, and care help anchor my ambition to reality.

To my parents, Robert and Sandra: for nurturing my love of life and wonder of science.

To all who work on sustainable energy solutions for a hungry and thirsty world. Energy is the key to humanities most basic needs–clean water, adequate nutrition, and shelter. May we truly understand the meaning of, and implement a sustainable energy economy.

"There are only two ways to live your life. One is as though nothing is a miracle. The other is as though everything is a miracle." – Albert Einstein

EPIGRAPH

The heavens declare the glory of God;
  the skies proclaim the work of his hands.
Day after day they pour forth speech;
  night after night they display knowledge.
There is no speech or language
  where their voice is not heard.
Their voice goes out into all the earth,
  their words to the ends of the world.
  In the heavens he has pitched a tent for the sun,
which is like a bridegroom coming forth from his pavilion,
  like a champion rejoicing to run his course.
It rises at one end of the heavens
  and makes its circuit to the other;
  nothing is hidden from its heat.

Psalm 19:1-6 New International Version ©1984

TABLE OF CONTENTS

LIST OF FIGURES

LIST OF TABLES AND SCHEMES

ACKNOWLEDGEMENTS

The volume of work presented here would not have been possible without the help of many people. This section is not exhaustive in mentioning everyone who helped, however, I have highlighted those that were critical in creating new knowledge and a new scientist.

First I want to thank my family for supporting me throughout the past six years. Most of all, I thank my wife Jenny– the love of my life. She listened while I complained about experiments not working, helped to keep me fed, looking good, wearing clean clothes, and being the best friend that I could ever hope for.

Next I want to thank Dr. Kubiak for the opportunity to work under his supervision. Thank you for the big ideas and the bravery to try to answer hard questions in regards to carbon dioxide chemistry and sunlight driven processes. Thank you for providing the funding and space to try my own ideas and the freedom to explore, try, fail, try again, succeed, and push for excellence. I also want to thank the members of the Kubiak lab that helped me through graduate school, and helped improve my dissertation manuscript. I especially want to thank my officemates who played basketball with me and made me laugh my last year to help me de-stress: "Viking" Mike Doud, "MJ" Mark Llorente, "Froehlich Factor" Jesse Froehlich, and "T-bag" Travis Blane. I wish them success in whatever they do.

Special thanks to my committee members. Dr. Tauber, for his many helpful discussions on light sources and quantification techniques. Dr. Bandaru, for his advice and help with the engineering as well as defining fundamental research versus

development and scale-up design. Dr. Asbeck, for his help in compound semiconductors and cheerful smile every time I spoke with him. And Dr. Yu, for his knowledge of compound semiconductors as well.

I am indebted to Dr. Jacobs for his generous fellowship for the first three years of graduate school– I hope to be able to give back in a similar fashion throughout my career. I would not have returned to school without the encouragement of scientists at China Lake. I thank Dr. Guenthner, Dr. Wright, Dr. Lindsey, and Dr. Davis for getting me started. Thank you to my high school chemistry and physics teacher Mr. Benzinger for teaching me to think and use my brain instead of relying on a computer or calculator.

Chapter 2 and 3, in part, are currently being prepared for submission for publication of the material, entitled, "Light Assisted Homogeneous Electrocatalytic Reduction of Carbon Dioxide on p-Type Silicon Evidenced by Cyclic Voltammetry," written by Aaron J. Sathrum and Clifford P. Kubiak. The dissertation author was the primary investigator and author of this material.

Chapter 4, in part, is currently being prepared for submission for publication of the material, entitled, "Artificial Photosynthesis of CO from CO_2: How Efficient is it?" written by Aaron J. Sathrum and Clifford P. Kubiak. The dissertation author was the primary investigator and author of this material.

Chapter 5, in part, is a reprint of material that has been submitted to the Journal of Physical Chemistry C Letters, entitled, "Kinetics and Limiting Currents of Homogeneous and Heterogeneous Electrocatalytic EC' Systems for Solar Generated Fuels," written by Aaron J. Sathrum and Clifford P. Kubiak. The dissertation author was the primary investigator and author of this material.

VITA

1980   Born, Eureka, California

1998-2002   Fieg-Tucker Humboldt-Del Norte 4-H Scholarship

2000   Energy Efficiency Intern - Title 24, California Energy Commission

2002   Bachelor of Science in Electrical Engineering and Materials Science and Engineering, University of California, Davis

2003-2005   Electronic Failure Analysis Engineer, NAVAIR, China Lake

2005-2008   Joan and Irwin Jacobs Fellowship

2006   Master of Science, Materials Science and Engineering, University of California, San Diego

2006-2010   Research Assistant, Materials Science and Engineering, University of California, San Diego

2011   Doctor of Philosophy, Materials Science and Engineering, University of California, San Diego

PUBLICATIONS

Aaron J. Sathrum, Clifford P. Kubiak. **Kinetics and Limiting Currents of Homogeneous and Heterogeneous Electrocatalytic EC' Systems for Solar Generated Fuels.** Submitted to *J. Phys. Chem. C. Lett*, June 2011.

Aaron J. Sathrum, Clifford P. Kubiak. **Photovoltaic Driven Homogeneous Electrolysis of Carbon Dioxide**. To be submitted.

Aaron J. Sathrum, Clifford P. Kubiak. **Light Assisted Homogeneous Electrocatalytic Reduction of Carbon Dioxide on p-Type Silicon Evidenced by Cyclic Voltammetry.** To be submitted.

Bhupendra Kumar, Aaron J. Sathrum, Mark J. Llorente, Jesse D. Froehlich, Clifford P. Kubiak. **Solar Splitting of Carbon Dioxide and Formation of Liquid Fuels**. Submitted to *Annual Review of Physical Chemistry*, Summer 2011.

Aaron J. Sathrum. **Debating Science and Religion**. *Chemical & Engineering News*. (2009), **87**, p. 5-6.

Eric E. Benson, Clifford P. Kubiak, Aaron J. Sathrum, Jonathan M. Smieja. **Electrocatalytic and Homogeneous Approaches to Conversion of CO_2 to Liquid Fuels.** Chemical Society Reviews. (2009), **38**, p. 89-99

Matthew C. Davis, Aaron J. Sathrum. **Solvent–free Claisen Condensation of Isophorone and Verbenone with *para*–hydroxyethylaminobenzaldehydes.** *Synthetic Communications*. (2007), **37,** p. 921-6

Andrew J. Guenthner, Aaron J. Sathrum. **Relative Stability Measurements of Chromophores in Polymer Optical Waveguide Materials**. *Proceedings of the SPIE - The International Society for Optical Engineering*. (2005), **5935**, p. Q-1-12

Matthew C. Davis, Andrew C. Chafin, Aaron J. Sathrum. **Convenient Preparation of N,N'-diphenyl-N,N'-bis(4-aminophenyl)-p-phenylenediamine**. *Synthetic Communications*. (2005), **35**, p. 2085-90

PROFESSIONAL AND ACADEMIC SOCIETIES

American Chemical Society (ACS)

American Solar Energy Society (ASES)

California Center for Sustainable Energy (CCSE)

Graduate Student Association (GSA)

ABSTRACT OF THE DISSERTATION

Solar Energy Storage through the Homogeneous Electrocatalytic Reduction

of Carbon Dioxide: Photoelectrochemical and Photovoltaic Approaches

by

Aaron John Sathrum

Doctor of Philosophy in Materials Science and Engineering

University of California, San Diego, 2011

Professor Clifford P. Kubiak, Chair

The sun is the most abundant resource of renewable energy available to the Earth. More energy strikes the surface of the earth in one hour than all primary energy consumption by humanity in an entire year. However, solar energy is intermittent, and if it is to become a major contributor to the electricity supply, an inexpensive and reliable

form of massive energy storage will be necessary. The ability to convert solar electricity into a liquid fuel is an attractive solution to the energy storage problem. A challenging goal will be to use only H_2O and CO_2 as feedstocks for making synthetic hydrocarbon fuels. Electroreduction of CO_2 to liquid fuels necessitates the use of efficient electrocatalysts to increase efficiency and rate for the essential development of practical industrial processes.

Two approaches towards the storage of energy in chemical bonds are investigated. The photoelectrocatalytic production of CO using CO_2 as a feedstock demonstrates the capture of solar energy and subsequent electrochemical conversion into a useful chemical commodity. CO_2 is reduced at illuminated p–Silicon (p–Si) cathodes using the electrocatalyst *fac*–Re(2,2'–bipyridyl)CO_3Cl at a 440 mV less anodic potential when compared to a glassy carbon electrode. Cyclic voltammograms of the electrocatalyst with CO_2 show an increase in current at the second reduction wave.

In the second approach, a fully integrated system for a directly coupled solar photovoltaic driven CO_2 electrolyzer was built and characterized. The design and theoretical voltage requirements show a minimum practical voltage of 3.4 V even though the thermodynamic minimum is only 1.33 V. The balancing of a non-linear power supply to a non-linear load reveals a self–stabilizing nature. An overall solar conversion efficiency (η_{TOT}) of 2.1% is achieved by using the electrocatalyst Re(4,4'-di-*tert*-butyl-2,2'-bipyridine)(CO)$_3$Cl. Theoretical calculations predict an upper efficiency limit of 21% for a single junction solar cell coupled to an electrolyzer. This stand-alone performance shows great promise and demonstrates the need for further development of more efficient CO_2 electrocatalysts.

CHAPTER 1

SOLAR ENERGY AND THE NEED FOR ENERGY DENSE STORAGE

1.1   ABSTRACT

The storage of renewable energy is needed on an immense scale. The worldwide energy consumption is presented with information on the sources of energy and the end uses. The 2008 average power for the globe was 16.6 TW with 86% supplied by fossil fuels. Because fossil fuels are non-renewable they will eventually be depleted and a replacement source of energy will need to be harnessed. Already the U.S. domestic oil production has peaked, in 1970. The sun is the most abundant resource of renewable energy available to the Earth. More energy strikes the surface of the earth in one hour than all primary energy consumption by humanity in an entire year. However, solar energy is intermittent, and if it is to become a major contributor to the electricity supply, an inexpensive and reliable form of massive energy storage will be necessary. The ability to convert solar electricity into a liquid fuel is an attractive solution to the energy storage problem. A challenging goal will be to use only H_2O and CO_2 as feedstocks for making synthetic hydrocarbon fuels. If the reduction of carbon dioxide to liquid fuels is to be accomplished through photovoltaic or other electrochemical means, the use of efficient electrocatalysts to increase efficiency and rate will be essential for the development of practical industrial processes.

1.2   WORLDWIDE ENERGY

There is no planet B. Energy is at the heart of all of the benefits of modern day society and is the largest economic market in the world. While many today enjoy the rich

benefits of inexpensive energy, one third of the world population still does not have adequate access to electricity.[1] The Earth is the only home we have, and as the population continues to grow and advance, our collective impact on the globe further stresses our ecosystems. Think of the many issues facing the world today: clean water, food shortages, access to electricity, adequate shelter, clean transportation, and many more. Which of these issues could not be improved by a readily available, sustainable, and an inexpensive supply of energy? Practical benefits, for example, include food, water, shelter, heating, cooking, transportation, lighting, and manufacturing. As more people gain access to energy, the need for an environmentally responsible and renewable energy supply becomes even more imperative.

In 2008 the world consumed 5.22×10^{20} J of total energy,[2] which when averaged over an entire year equates to a constant power production of 16.6 TW. This staggering number demonstrates the scale at which the human population uses energy. Electronics, homes, cars, planes, industrial processes, etc. consume energy at a pace not previously witnessed before in our world. To supply this growing hunger, we use fossil fuels obtained from oil, coal, and natural gas, which accounted for 86% of all energy consumed in 2008. The U.S. ranked as the #1 worldwide energy consumer at around 15% of the total. The global energy consumption is growing rapidly and the average power consumption is predicted to increase to 22.7 TW by 2030.[3] As the rest of the world continues to develop, especially India, China, and Africa, more energy will need to be supplied in a sustainable fashion. Solar energy has the potential to supply a significant portion of our energy needs, is geographically available to all citizens, and is within reach technically.

1.3   FINITE AMOUNT OF OIL

1.3.1 U.S. Energy History

By definition, a non-renewable resource is finite, will have a limited lifetime, and eventual scarcity. The United States has transitioned from using wood as its primary energy source, to coal, and most recently to petroleum over the last 236 years. These transitions were not driven by scarcity, but rather by convenience, versatility, and energy return on energy investment. Figure 1-2A shows the energy consumption timeline for the U.S. since 1775, according to the Energy Information Administration (EIA).[2] During the entire time period, the amount of energy consumed has grown enormously as the uses of energy thrived and provided a higher quality of living. Energy consumption from coal surpassed wood in 1885, petroleum surpassed coal in 1950, while hydroelectric and nuclear emerged as small contributors in the latter half of the 20th century. The use of fossil fuels is predicted to remain the major provider of energy for the next 25 years with non-hydroelectric renewable sources doubling by 2035.[3] The per capita energy consumption in the U.S. has grown slowly, increasing from 62.3 MWh in 1949 to 90.3 MWh in 2009, decreasing slightly after the 1970's oil price shocks and holding steady.[2] The U.S. has successfully navigated transitions to new sources of energy without economic disaster and can do so again. However, if nothing is done to significantly change the current path to more sustainable solutions, it will only be a matter of time before an unavoidable energy and environmental crisis will occur.

1.3.2 Peak Oil in the U.S.

The U.S. was self–sufficient in energy production until around 1960, as shown in Figure 1-2B. Since then the reliance on foreign imports has increased to 24% of all energy consumed as of 2009. Domestic oil production peaked in 1970 at 9.4 million barrels per day and has decreased 46% to 5 million barrels per day in 2009, as shown in Figure 1-2C. The argument over peak oil in the U.S. is not open to debate given that the domestic peak occurred over 40 years ago. In 2009, Canada was the largest petroleum exporter to the U.S. while 41% of petroleum imports came from the Organization of Petroleum Exporting Countries (OPEC), down from its peak in 1977 of 70%. In 2009, transportation was the single largest consumer of petroleum, accounting for 71% (13.3 million barrels per day) of the total used. With domestic sources of oil decreasing, the increased dependence upon foreign oil sources may create geopolitical tensions that could be avoided by harnessing some of the immense renewable resources in the U.S.

1.3.3 Use of Petroleum for Transportation

Fossils fuels are some of the most dense, transportable, and easily dispensable forms of energy. One liter of gasoline contains an incredible 35 MJ of energy, and is limited by the Environmental Protection Agency (EPA) to a transfer rate of 37.8 liters per minute for motor vehicles. This allows for example, cars with large ranges, and airplanes with fast speeds, to be replenished with energy quickly. The EPA limit to motor vehicles is power being transferred (i.e. energy rate), and is the electrical equivalent to a 22 MW operating power plant to refuel a single car. There is no known technology for storing and

rapidly transferring electrical energy of this magnitude to a motor vehicle. In 2009 the transportation sector of the U.S. consumed 27% of all energy, and 94% of this was obtained from petroleum sources. Figure 1-3 shows the relationships between energy supplies and energy consumers in the U.S. in 2009.[2] Only 3% of the transportation energy demand was supplied by renewable resources. A major reason for this low value is that most renewable sources produce electric power that is not readily integrated into the existing transportation energy infrastructure. Although hybrid and electric vehicles are emerging on the market, they still lack the range and rapid refueling capabilities of modern cars. A process that could convert electricity into a liquid fuel would be revolutionary and transformational. This would store renewable energy in chemical bonds as a liquid fuel that can be readily integrated into the existing infrastructure for transportation.

1.4 THE SOLAR RESOURCE

The sun is the most abundant resource of renewable energy available on the Earth. Other renewable sources include hydroelectricity, ocean, biomass, wind, and geothermal. Altogether these resources can provide a sustainable energy balance for a growing economy and increased quality of living for society. The average amount of solar energy incident at the top of the atmosphere is 1367 W m^{-2}.[4] With a radius of 6,378 km, the projected disc of the Earth collects an astounding 173,600 TW of constant power. For comparison, the average global power consumption was 16.6 TW in 2009, and in one year humanity consumes 145,500 TWh of energy. Therefore, more energy strikes the

surface of the earth in one hour than all primary energy consumption by humanity in an entire year. To be more realistic however, approximately 30% of this energy is lost due to absorption and reflection in the atmosphere, leaving approximately 120,000 TW at ground level.[5] Since only 30% of the Earth's surface is covered by land, and for most applications solar is installed on land, the practical amount is further reduced to 36,500 TW. Solar energy is available across the globe irrespective of geographic borders over a range of values,[6] as shown in Figure 1-4. Desert regions and mid–latitude areas have the largest potential for solar energy harvesting. With solar photovoltaic efficiencies approaching 20%, 7,300 TW of power could be harnessed, if we covered all land surfaces. Nonetheless, to reach the average global power consumption of 16.6 TW, only 0.2% of the land would need to have photovoltaics exposed to the sun.

The solar resource is variable, primarily due to the day/night diurnal cycle, seasonal changes, and clouds from weather. The demand, for example, from electricity is also variable and does not correlate well with the variation in solar production. Behavior changes and smart grid controls can help shift some of the electrical demand, but this alone cannot alleviate the entire mismatch. Figure 1-5 shows lights at night on Earth,[7] highlighting the regions with dense populations and reliable access to electricity. The ability to power these lights at night would require an immense and rapid storage system for solar electricity. Figure 1-6 shows supply and demand data for electricity from the California independent system operator. The solar production of electricity peaks in the middle of the day and is only a small fraction of power, ~1.5% at noon, decreasing to 0% at night. Solar is currently only 0.01% on average of the total primary energy supplied in the U.S.[2] No large scale system exists for storing massive amounts of electricity needed

for the U.S. electrical grid. A small scale example is water pumped uphill at hydroelectric dams that can store some energy, but is limited in scope and subject to the hydrological cycle.[8] If solar energy is to become a major contributor to the electricity supply, some inexpensive and reliable form of massive energy storage will be necessary.

1.5 ELECTROCATALYSIS FOR RENEWABLE SOLAR FUELS

1.5.1 Electricity Storage in CO_2 and H_2O Conversion

The ability to convert solar electricity into fuel is an attractive solution to the energy storage problem. Solar fuels are concentrated energy carriers with long–term storage capacity.[9] The technology for the capture and conversion of solar energy into electricity using photovoltaic technology has experienced tremendous growth recently. The demand for solar electricity has grown by an average 30% per year over the past 20 years.[10] The costs have been declining primarily due to economies of manufacturing scale, manufacturing technology improvements, and the increasing efficiency of solar cells. Even with growing renewable resource harvesting, there is currently no large scale solution to storing the massive quantities of energy. A challenging goal will be to use only H_2O and CO_2 as feedstocks for making synthetic hydrocarbon fuels.[11]

1.5.2 Inspiration from Photosynthesis

Natural photosynthesis in green plants, algae, and cyanobacteria use solar energy to convert water and atmospheric carbon dioxide to energy rich carbohydrates at room

temperature and a biological pH range of 6–8. However natural systems operate at low thermodynamic efficiency, with an estimated maximum efficiency of 8–9%.[12] Additionally biofuels require substantial supplies of water and may displace basic food supplies that can lead to higher food prices. Photosynthetic water oxidation in photosystem II (PSII) is known to use metal based catalysis to guide the chemistry. At the heart of the PSII system is a Mn_4Ca cluster.[13] In PSII, oxygen is generated and released, while electrons and protons are extracted. In a separate photoreaction in photosystem I (PSI), atmospheric CO_2 is reduced by the incorporation of the electrons and protons from PSII. Photosynthesis is proof that such reactions can be driven solely by the sun, and a source of inspiration for those that try to create similar processes. These attempts, often termed artificial photosynthesis, are chemical processes that mimic the natural template providing a direct pathway for storing solar energy in chemical bonds.

If the reduction of carbon dioxide to liquid fuels is to be accomplished through photovoltaic or other electrochemical means, the use of efficient electrocatalysts will be essential for the development of practical industrial processes. An electrocatalyst participates in an electron transfer reaction and facilitates acceleration of a chemical reaction.[14] Figure 1-7 shows a generic reaction scheme for upgrading CO_2 into a higher energy state using an electrocatalyst to lower the overpotential barrier (η). This example produces CO which can be used to produce hydrogen via the water–gas shift reaction.[15] A combination of CO and H_2 can then be transformed into liquid fuels via Fischer–Tropsch chemistry.[16] Both the electron transfer and chemical kinetics must be fast for an efficient electrocatalyst. Additionally, an optimal electrocatalyst must display a good thermodynamic match between the redox potential (E°) for the electron transfer reaction

and the chemical reaction that is being catalyzed (e.g. reduction of CO_2 to CO). These factors can be optimized by chemical tuning of the electrocatalyst metal centers via appropriate ligand design. Electrocatalysts are typically screened for their redox potentials, current efficiencies, electron transfer rate and chemical kinetics in order to determine the best overall catalysts.

In this thesis, two approaches towards artificial photosynthesis are presented. The first is through the use of a CO_2 electrocatalyst with reductive semiconductor photoelectrochemistry. Light is efficiently captured and converted to electrical energy that is directly transferred at the semiconductor surface to fuel formation reactions directed by the solution phase (homogeneous) electrocatalyst. In the second approach, the photocollector and electrode surface are decoupled and optimized separately. This involves using commercial solar cells and the construction of an efficient homogeneous CO_2 electrolyzer. The objective of this thesis is to investigate the energetics involved in CO_2 conversion and to develop a scalable approach to efficient CO_2 electrolysis.

Figure 1-1 NASA "blue marble" image of the Earth showing the western hemisphere of our planet. This beautiful image was taken February 2002 from the Moderate Resolution Imaging Spectroradiometer (MODIS).[17]
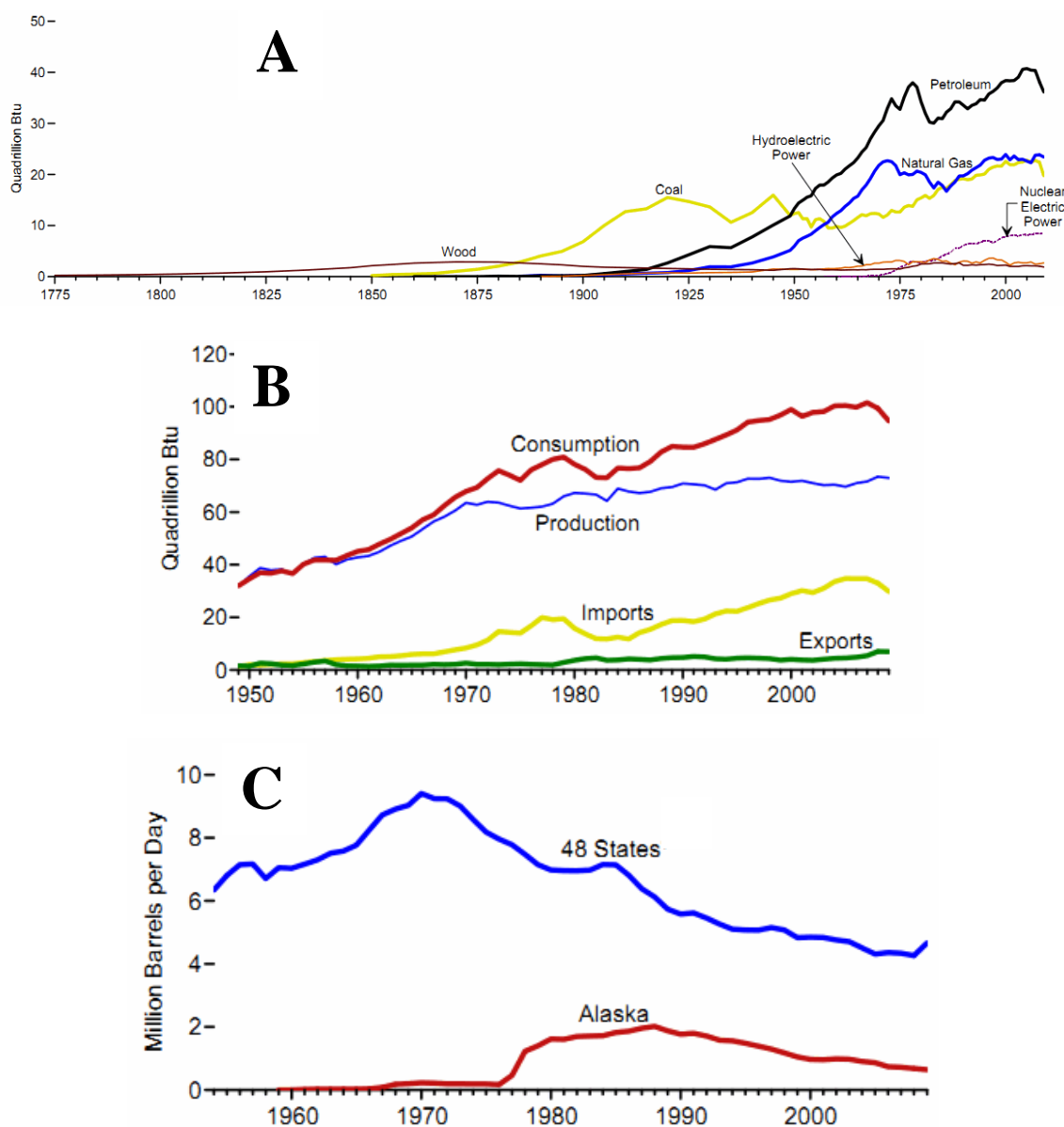
Figure 1-2 Energy consumption and production in the U.S. from the EIA.[2] **(A)** Historical primary energy consumption by source in the U.S. **(B)** Total energy consumption and production in the U.S. including imports and exports. **(C)** Domestic oil production of crude oil in the U.S.

(quadrillion Btu and percent)

2009 Total = 94.6 quadrillion Btu
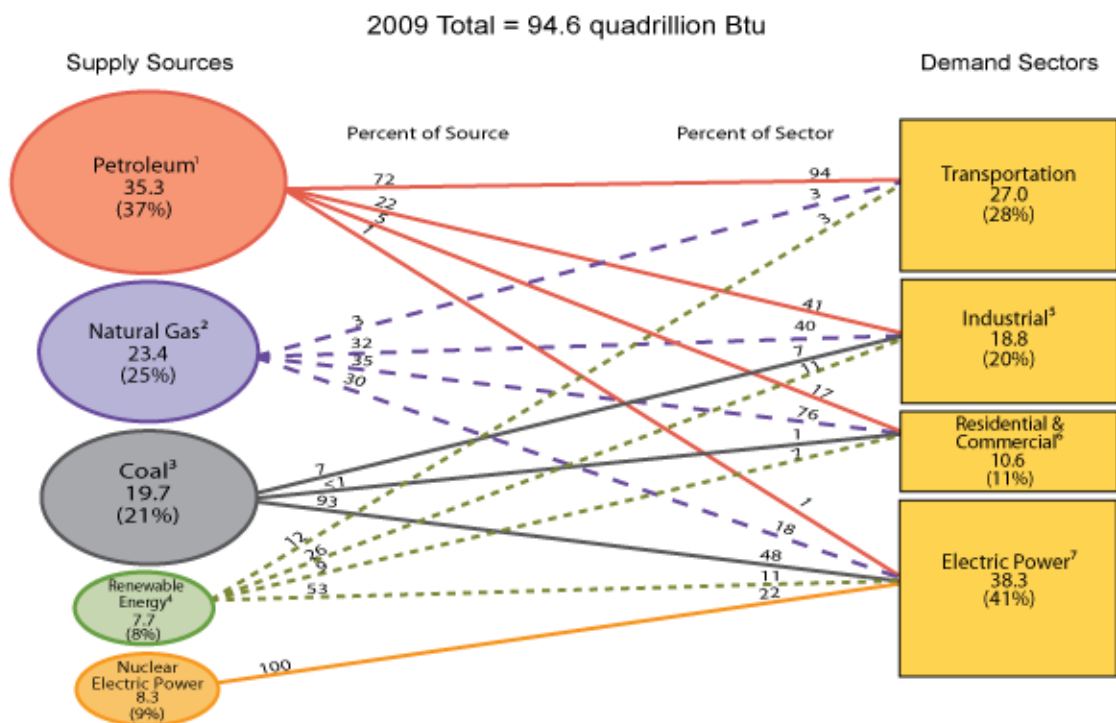
Figure 1-3 U.S. primary energy flow by source and sector from 2009.[2] The transportation sector relies heavily on petroleum sources. Fossil fuels from petroleum, natural gas, and coal supplied 83% of the total energy.
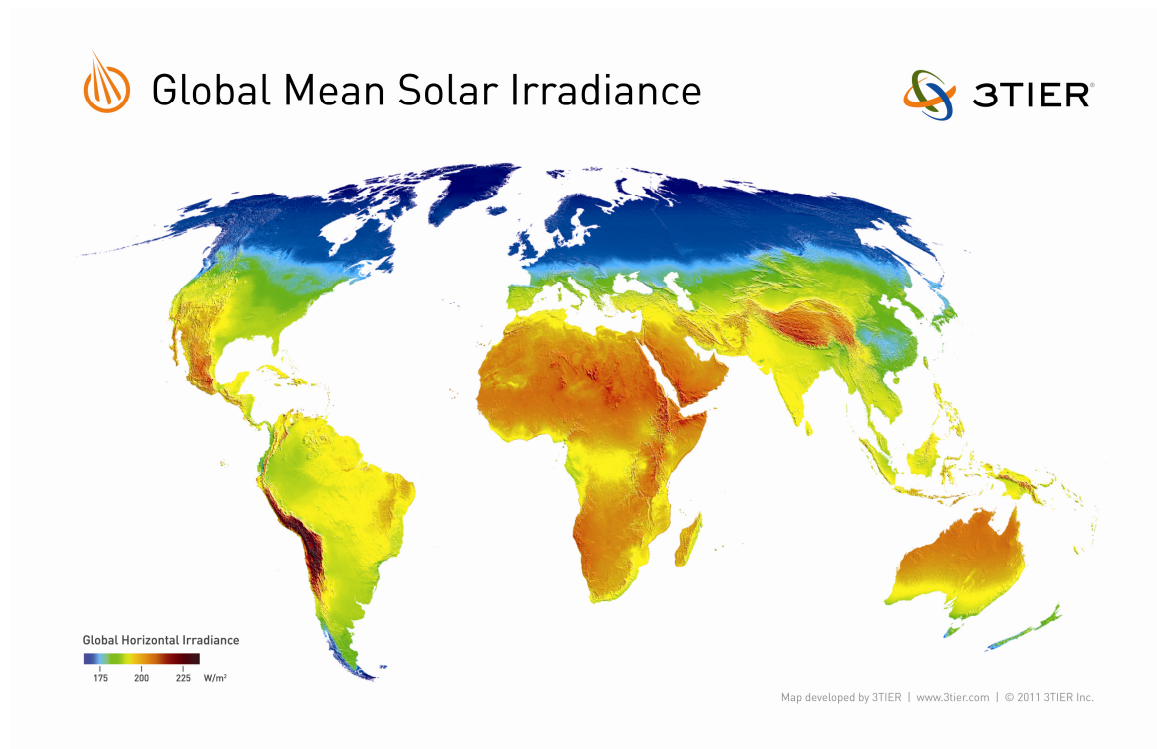
Figure 1-4 A map of the land masses on Earth showing the solar resource available.[6]
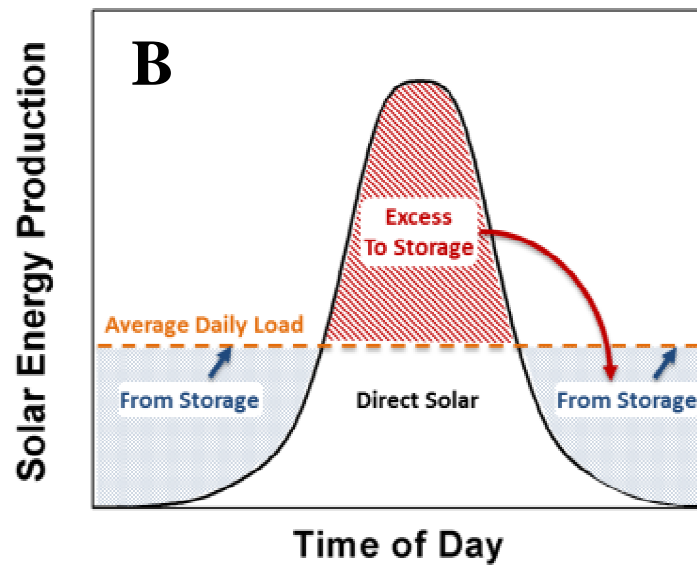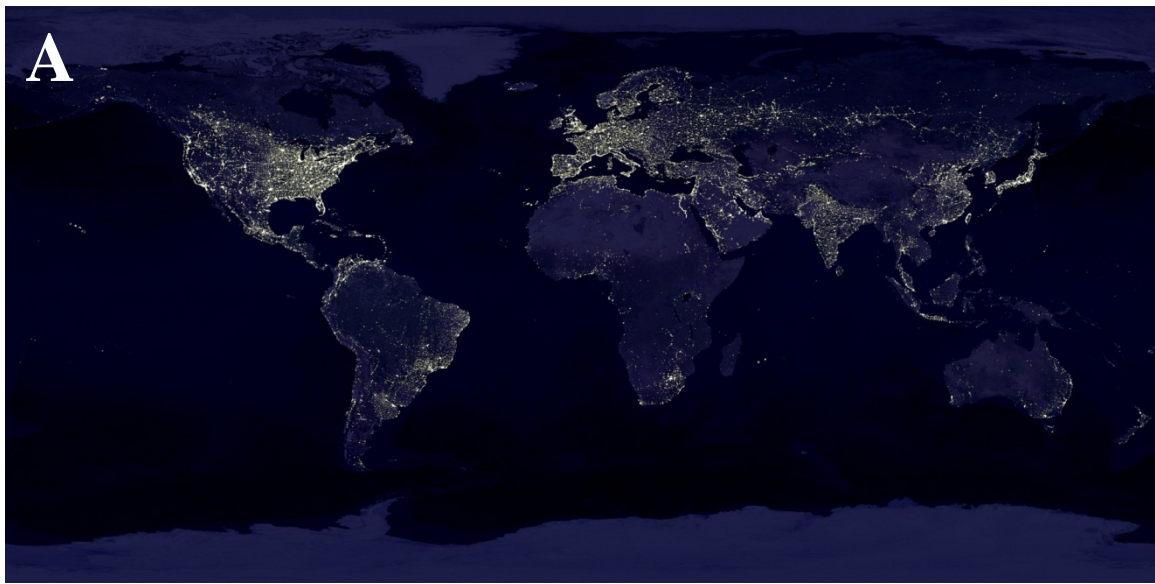
Figure 1-5 (A) NASA image of the Earth at night showing lights from human activity. The image was taken October 2000 from the Defense Meteorological Satellite Program (DMSP) Operational Linescan System (OLS).[7] (B) The conceptual storage of excess solar energy during the day and withdrawing it at nighttime.
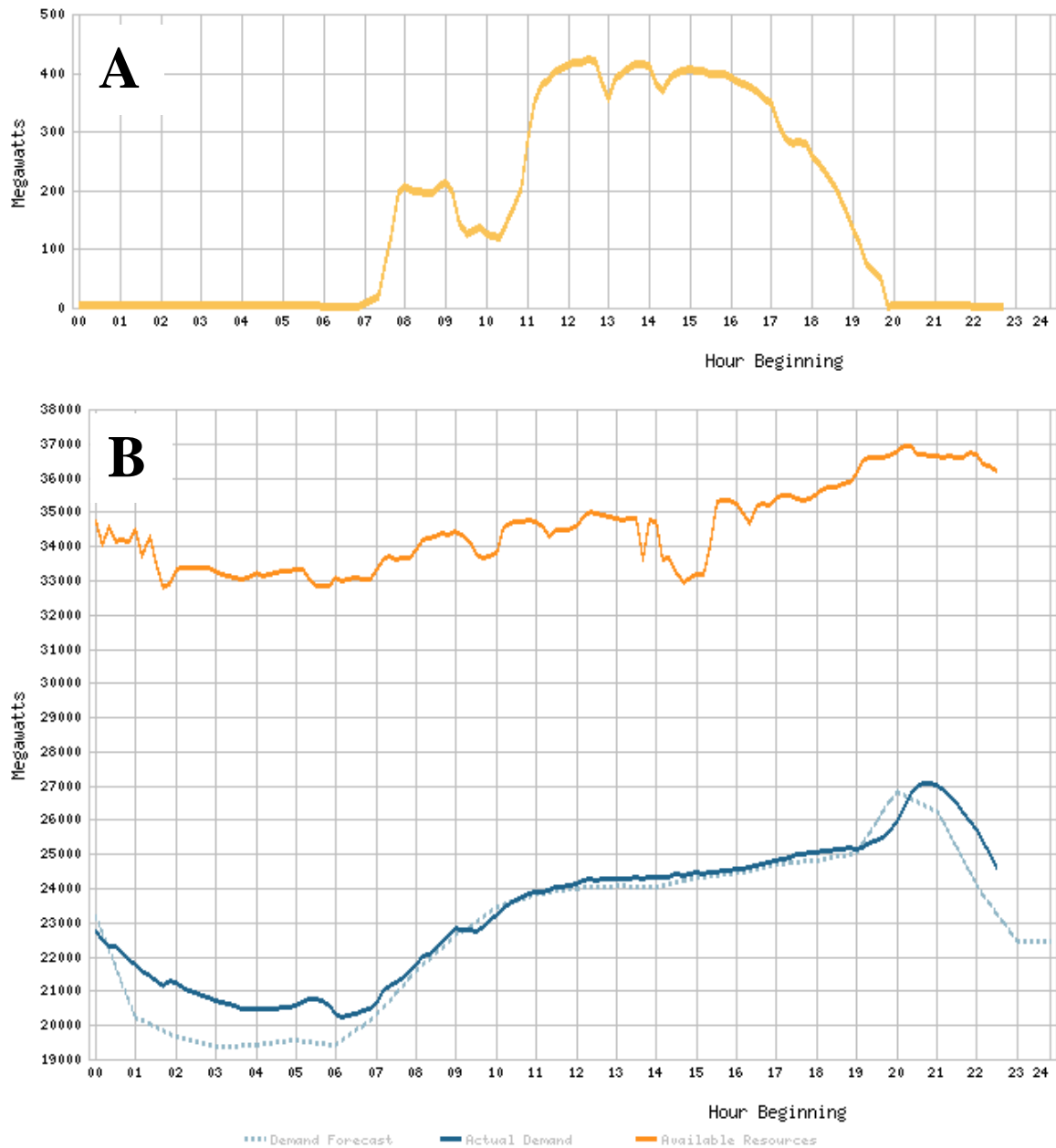
Figure 1-6 An example of a daily power production and consumption (megawatts) in California from the independent system operator on June 5th 2011.[18] **(A)** The total daily solar power production peaks at ~430 MW around 12 PM, morning intermittency possibly due to clouds between 8 and 11 AM decreased the expected power. **(B)** The total daily power demand peaks around 9PM at ~27,000 MW. The dashed line is the demand forecast and the orange line shows the available resource (reserve capacity).
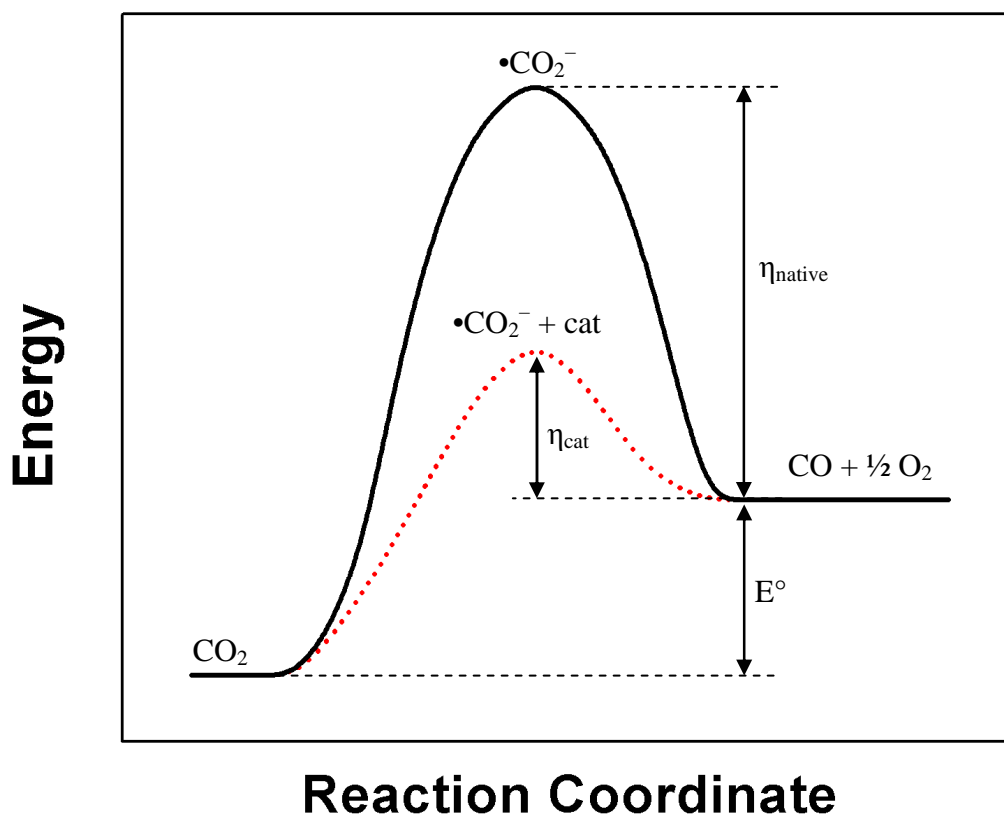
Figure 1-7 Qualitative reaction scheme for the conversion of CO_2. An electrocatalyst can decrease the input energy and increase the rate to improve the energy efficiency. η is the additional voltage required (overpotential).

1.6   REFERENCES

(1)   Goldemberg, J. *World Energy Assessment*; United Nations Development Programme: New York, NY, 2000.

(2)   "Annual Energy Review 2009," U.S. Energy Information Administration, DOE/EIA−0384.

(3)   "Annual Energy Outlook 2010," U.S. Energy Information Administration, DOE/EIA−0383.

(4)   ASTM, Reference Solar Spectral Irradiance: Air Mass 1.5, http://rredc.nrel.gov/solar/spectra/am1.5/, May 25, 2011

(5)   Gust, D.; Moore, T. A.; Moore, A. L. Solar Fuels via Artificial Photosynthesis. *Acc. Chem. Res.* **2009**, *42*, 1890-1898.

(6)   Global Solar Irradiance Map, http://www.3tier.com/en/support/resource-maps/, June 7, 2011

(7)   Mayhew, C.; Simmon, R., Earth's City Lights, http://visibleearth.nasa.gov/view_rec.php?id=1438, May 25, 2011

(8)   Lewis, N. S.; Nocera, D. G. Powering the planet: Chemical challenges in solar energy utilization. *Proc. Natl. Acad. Sci. U. S. A.* **2006**, *103*, 15729-15735.

(9)   McDaniel, N. D.; Bernhard, S. Solar fuels: Thermodynamics, Candidates, Tactics, and Figures of Merit. *Dalton Trans.* **2010**, *39*, 10021-10030.

(10) Solar Energy Market Growth, http://solarbuzz.com/facts-and-figures/markets-growth/market-growth, June 9, 2011

(11) Roeb, M.; Müller-Steinhagen, H. Concentrating on Solar Electricity and Fuels. *Science* **2010**, *329*, 773-774.

(12) Bolton, J. R.; Hall, D. O. The Maximum Efficiency of Photosynthesis. *Photochem. Photobio.* **1991**, *53*, 545-548.

(13) Dau, H.; Zaharieva, I. Principles, Efficiency, and Blueprint Character of Solar-Energy Conversion in Photosynthetic Water Oxidation. *Acc. Chem. Res.* **2009**, *42*, 1861-1870.

(14)   Benson, E. E.; Kubiak, C. P.; Sathrum, A. J.; Smieja, J. M. Electrocatalytic and Homogeneous Approaches to Conversion of CO_2 to Liquid Fuels. *Chem. Soc. Rev.* **2009**, *38*, 89-99.

(15)   Navarro, R. M.; Peña, M. A.; Fierro, J. L. G. Hydrogen Production Reactions from Carbon Feedstocks:☐ Fossil Fuels and Biomass. *Chem. Rev.* **2007**, *107*, 3952-3991.

(16)   Klerk, A. d. Fischer−Tropsch Fuels Refinery Design. *Energy Environ. Sci.* **2011**, *4*, 1177-1205.

(17)   Stöckli, R.; Simmon, R., The Blue Marble, http://visibleearth.nasa.gov/view_rec.php?id=2429, May 25, 2011

(18)   California ISO: System Status, http://www.caiso.com/outlook/SystemStatus.html, June 5, 2011

CHAPTER 2:

PHOTOELECTROCHEMISTRY OF

P-GAP AND *P*-SI

2.1 ABSTRACT

An introduction to the field of semiconductor-liquid junctions is presented. This is then applied to the conversion of light into chemical energy on *p*-type gallium phosphide and *p*-type silicon. The degree of band bending, which creates a built–in electric field for efficient photon capture and charge separation is discussed. Fermi level pinning due to surface states explains the observed deviation from the ideal case. The construction of photoelectrodes, the making of ohmic contacts, and surface pretreatment are shown. The photoresponse of *p*-Si shows: 1) a 475 mV shift in the required voltage as compared to platinum, 2) reversible electrochemical behavior, and is 3) Fermi level pinned. The photoresponse of *p*-Gap shows a varying degree of photovoltage from 200-900 mV as compared to platinum depending on the redox couples. The *p*-GaP photoelectrochemical behavior is not well defined and shows poor surface kinetics. To conclude, the relative band positions to specific redox couples are shown to aid in the understanding of the photoresponse.

2.2 INTRODUCTION

The conversion of light or photonic energy into a useful and storable form is fundamentally demonstrated in living plants. Through photosynthesis life is continued on Earth. Stemming from this inspiration is a fundamental knowledge that it can be done, and moreover that is sustainable. As pointed out in the first chapter, the sun is the most powerful source of renewable energy available to the Earth. The use of solar power is not

a new concept or practice. For example, it is known that the ancient Romans lined water channels with black slate to preheat water for bathhouses.[1] However heat is not always desired, nor is it the most useful form of energy. Electricity is one of the most useful forms of energy used today. It can be transported rapidly over long distances and efficiency converted into useful work on demand. However it does have an Achilles heel: the lack of large scale storage. Currently, research into the development of solar energy storage via liquid fuels is currently being pursued with great enthusiasm.

In 1839 Becquerel discovered the photoelectric effect[2] using platinum electrodes. This was the first photovoltaic device, and it may surprise many that it was produced at a solid-liquid interface. Illumination between two platinum electrodes immersed in AgCl produced a current because the silver halide behaved as a semiconductor and produced an electric field at the electrode surface. This was not fully understood for more than 100 years when Brattain and Garrett[3] at Bell Laboratories demonstrated and explained a similar effect at the Germanium electrolyte interface. Further fundamental physics and groundwork for photoelectrochemistry was done by Gerischer[4] and many good reviews[5-34] can be found on the subject. In this chapter, photoelectrochemistry, or "Interfacial Photoinduced Charge Separation and Redox Chemistry" as called by Nozik[15] will be explained along with specific experiments involving the semiconductors gallium phosphide (GaP) and silicon (Si).

2.3 PHOTOELECTROCHEMISTRY OF SEMICONDUCTOR-LIQUID JUNCTIONS

2.3.1 Electronic Structure of Semiconductors

When describing the general conductivity of a material, there are three major classifications: conductor, semiconductor, and insulator. Since in the bulk solid state there are a large number of atoms, the atomic orbitals combine in what is termed energy bands. Figure 2-1 shows a simple diagram of these concepts.[35] A band is a continuum of energy levels with the highest occupied state defined as the valence band (E_V) and the lower unoccupied state called the conduction band (E_C). For conductors the valence band and conduction band overlap resulting in excellent conductivity. In semiconductors there is a separation in these two bands called the band gap (E_G) that is equal to E_C-E_V. Natively at room temperature a semiconductor does not conduct, but electrons can be promoted to the conduction band by various physical driving forces, e.g. thermal, or photonic. Finally an insulator has a large band gap such that it is very difficult to change into a conducting state.

2.3.2 Doping of Semiconductors, i-, n- and p-type

A pure semiconductor material is called intrinsic (e.g. *i*-Si) and has a very small number of electrons that can contribute to conduction. The number of charge carriers can be increased by intentionally adding an impurity or dopant. Figure 2-2 shows the relevant energy levels that are discussed in this chapter. Silicon is the most common

semiconductor used today, and belongs to the group IV series with four outer-shell (valence) electrons. If a group V element such as phosphorus is added to bulk silicon, the dopant will have five valence electrons and the extra electron produces a donor level (E_D) near the conduction band that can easily be promoted. This results in an excess of negative carriers in the conduction band, hence the designation *n*-type. Conversely if a group III element such as boron is added, the dopant will have only three valence electrons and produces an acceptor level (E_A) near the valence band. An electron from silicon can now be easily promoted to the acceptor level resulting in a hole (mobile positive charge carrier). An excess of positive carriers results, and is designated *p*-type. The Fermi level (E_F) is defined as the energy level where the probability of occupation by an electron is one half. For an intrinsic semiconductor this lies at $\frac{1}{2}E_G$. For doped semiconductors the Fermi level moves according to the shift in induced electron population. For *n*-type it is between the E_D and E_C and called $E_{F,n}$, while for *p*-type the Fermi level is between E_A and E_V and called $E_{F,p}$. These new levels are shown in figure 2-2(b-c). It is important to note that while this level is inside E_G, no electrons are actually at this level because it is in the forbidden region where there are no states. The Fermi level of a semiconductor can also be externally moved by applying a potential. More negative applied potentials raise the Fermi level (more reducing potential) whereas positive potentials lower (more oxidizing) it. The location of the Fermi level determines the behavior when in contact with an electrolyte and in the next section it will be shown how the bands bend in order to equilibrate to the solution Fermi level.

2.3.3 Band Positions

Now that the electronic band structure of semiconductors has been explained, the location of the valence and conduction bands with respect to an absolute energy scale is needed. In physics, the location is measured from the absolute vacuum level and all energies are negative with respect to E_{vacuum}. Measurement of the band positions is often determined from Mott-Schotkky[36-38] plots of capacitance versus voltage according to equation 2-1.

$$\frac{1}{C^2} = \frac{2kT}{\varepsilon\varepsilon_0 n_0 e^2}\left(\frac{eV}{kT} - 1\right) \qquad \textbf{(2-1)}$$

Where ϵ is the dielectric constant of the semiconductor, ϵ_0 is the permittivity of free space, k is the Boltzmann constant, T is the temperature, n_0 is the equilibrium carrier concentration of the conduction band, C the measured capacitance, V the applied voltage, and e the elementary charge of an electron. Figure 2-3 shows a summary of selected semiconductor positions and several redox couples. Note that since many semiconductors are oxides or have surface groups with protons, and the band positions will directly vary with the pH of the solution according to the Nernst equation (59mV per pH unit).[39]

2.3.4 Band Bending at the Interface

In order for the two phases to be in equilibrium the electrochemical potential must be the same. For a semiconductor this is determined by the Fermi level, and for the solution it is determined by the redox potential of the electrolyte solution. If these two levels are not the same, then charge will flow between the semiconductor and the solution

until the levels are the same. The change in charge extends into the semiconductor in what is called the space charge region and therefore has a built in electric field. For the solution the change in charge extends into the double layer. The exact thickness of each region will depend on 1) doping level, 2) difference in energy levels (E_F-E_{redox}), and 3) electrolyte concentration. Doped semiconductors are used in order to maximize the amount of band bending, increase the theoretical photovoltage of the system, and produce a large amount of photocurrent.

2.3.4.1 *p-type at Open Circuit, Dark*

For a *p*-type semiconductor at open circuit, with $E_{F,p}$ at a more positive potential than E_{redox}, electrons will be transferred from the solution to the electrode to attain equilibrium. This is illustrated in Figure 2-4(a-b), where (a) is before contact, and (b) is after contact. Since the number of majority charge carrier (holes) has been decreased near the surface, the region is called the depletion layer. This generates a downward band bending shown in Figure 2-4(b). When E_{redox} is negative of $E_{F,p}$, electrons will be transferred from the electrode to the solution. This will result in a surplus of majority charge carriers near the surface shown in Figure 2-5(c). The bands bend upward, and the region is now called the accumulation layer because of the larger amount of positive charges. When $E_{redox} = E_F$, the junction is already at equilibrium and no charge flows, this situation is referred to as the flat band potential (E_{FB}) and shown in Figure 2-5(b).

2.3.4.2 n-type at Open Circuit, Dark

For a *n*-type semiconductor at open circuit, with $E_{F,n}$ at a more negative potential than E_{redox}, electrons will be transferred from the electrode to the solution to attain equilibrium. This is illustrated in Figure 2-6(a), with a decrease of negative charges near the surface resulting in a depletion layer. This generates an upward band bending. When E_{redox} is positive of $E_{F,n}$, electrons will be transferred from the solution to the electrode. This will result in a surplus of majority charge carriers, downward band bending, and an accumulation layer of negative charges.

2.3.4.3 Semiconductor-Liquid Junction Under Illumination

When light with energy $E_{h\nu} > E_G$ strikes the semiconductor surface, its absorption can promote an electron from the valence band to the conduction band. The lower the band gap, the more of the solar spectrum that can be absorbed, but at the cost of a lower maximum voltage. If this absorption occurs in the bulk of the semiconductor, the promoted electrons and resulting holes will recombine, producing heat. However if the absorption occurs in the space-charge region, the built in electric field will separate the charge. The convention for movement of charge is electrons will drop to a lower energy with respect to vacuum level (sink) and holes will rise to a lower energy (float). In the case of a *p*-type semiconductor liquid–junction with downward band bending, the built in electric field will drive the electrons to the surface and the holes into the bulk. If driven to a sufficient positive potential in the dark, the accumulation layer can pull electrons from

the solution. Therefore *p*-type semiconductors are photocathodes (reduction) and dark anodes (oxidation). The *n*-type arrangement is the reverse, as they will behave as photoanodes and dark cathodes.

The current that flows under illumination is called the photocurrent:

$$i_{photo} = i_{light} - i_{dark} \qquad \textbf{(2-2)}$$

Where *i* is the current measured in amperes. A better measurement normalizes the electrode surface area by reporting current density *j*, so that differences in electrode size are properly adjusted. The absorption, separation, and collection efficiency of the junction can be measured in terms of the quantum efficiency:

$$Quantum\ Efficiency = \phi_{QE} = \frac{electrons\ out}{photons\ in} = \frac{\dfrac{j}{F}}{\dfrac{P}{N_A h f}} \qquad \textbf{(2-3)}$$

Where *j* is the current density in A cm^{-2}, *F* is the faraday constant in C mol^{-1}, P is the monochromatic power density in W cm^{-2}, N_A is Avogadro's number, *h* is planck's constant, and *f* is the monochromatic frequency of the incident light. It is easiest to measure φ_{QE} via a monochromatic light source so that the flux of photons can be precisely measured.

The theoretical induced shift in the bands is termed the photovoltage or photopotential and is measured as:

$$V_{photo} = \left| V_{FB} - V_{redox} \right| \qquad \textbf{(2-4)}$$

Where V_{FB} is the flatband voltage and V_{redox} the redox electrochemical potential. Therefore in order to maximize the photovoltage, it is desired to have the V_{redox} slightly

less reducing than the E_{CB} for *p*-type semiconductors, and slightly more oxidizing than E_{VB} for *n*-type. Note to convert V to E use the relationship $V = E/e$. The V_{FB} can be found by measuring the photopotential as a function of radiation intensity, the position of the onset of photocurrent,[40] and/or the capacitance of the space charge region[41] as discussed in section 2.3.3. As a final note, E_G is a measure of the chemical bond strength. Large band gap materials tend to show greater surface stability, but the larger E_G results in a lower conversion efficiency of the visible spectrum.

2.3.4.4 Fermi Level Pinning

There is a very important deviation from the previously presented idealized junction theory. The concept of Fermi level pinning at illuminated semiconductor liquid-junctions was introduced by Wrighton, Bard, et al. in 1980[42-45] as adapted from Green.[46] Instead of the band edges being pinned (fixed) as shown in Figure 2-4, with the Fermi level free to float with applied bias, the Fermi level is pinned by surface states (as low as $\sim 10^{12}$ cm^{-2}), and the bands now move to accommodate. This modified view includes a Schottky barrier photocell in series with the electrochemical cell. The photovoltage is now independent of the redox couple in direct contradiction to equation 2-4. As a consequence of this similar photovoltages have been observed for redox potentials over a range larger than the band gap.[42] A new measure of the photovoltage can be defined as follows:

$$V_{photo,pinned} = \left| V_{photoelectrode} - V_{metal\ electrode} \right| \quad \textbf{(2-5)}$$

Where V is the measured voltage position of a redox couple on a reference metal electrode and on an illuminated semiconductor electrode. It was also observed that photoreduction can occur outside the band gap for E_{redox} more reducing than E_{CB}. Finally, in the ideal case when two redox potentials are within the E_G, one combined two-electron wave is expected. However in the pinning case it is observed as two separate one-electron waves with equal photovoltages.

Not all semiconductors exhibit Fermi level pinning. In general metal oxides and metal sulfides do not exhibit pinning, whereas elemental and compound semiconductors show pinning. Both Silicon[43] and GaP[47] show evidence that they are Fermi level pinned. Not all E_{redox} will pin the Fermi level. Redox couples need to be sufficiently negative in order to pin *p*-type and sufficiently positive to pin *n*-type. The exact degree of interaction will depend on the specific semiconductor–redox system and can be easily probed by judicious choice of various redox couples. The main disadvantage of Fermi level pinning is that the V_{photo} is limited to a fixed value. However since this effect is based on surface states, surface modification via functionalization and pretreatments can directly affect the fixed V_{photo}. A final advantage is a wider range of redox couples that can be driven by the photoelectrode.

2.3.5 Two Major Types of Photoelectrochemical Cells

The word photoelectrochemistry (PEC) is used to describe the resulting behavior of the semiconductor liquid junction under illumination. One advantage to PEC over a solid state photovoltaic is that they can have two very different products. The first is

voltage and current, essentially a photovoltaic producing power. The second is unique, as the product is a direct electrochemical reaction, essentially storing chemical energy. These two types are referred to as a regenerative cell and as a synthetic cell respectively. The regenerative cell is a closed loop system where at the photoelectrode a redox species is reduced (or oxidized), the electron travels through a load circuit where work can be extracted, and then the reduced (or oxidized) species is re-oxidized (or re-reduced) at the counter electrode. The redox couple acts as a charge shuttle with no net chemical change. A well studied example of a regenerative cell is the dye sensitized TiO_2 PEC solar cell by Grätzel.[48,49] The synthetic cell is an open loop system where at the photoelectrode a redox species is permanently reduced (or oxidized), and the electron travels to the counter electrode where a second species is oxidized (or reduced). The result is two new electrochemical products. A well studied example of a synthetic cell involves reactions of the splitting of water[50,51] or of carbon dioxide.[52,53] In this thesis, synthetic based PECs are investigated with a specific focus on the electrochemical reduction of carbon dioxide.

2.4 CONSTRUCTION OF *P*-GAP AND *P*-SI SEMICONDUCTOR ELECTRODES

2.4.1 Properties of GaP and Si

Gallium phosphide is a compound semiconductor with an indirect E_G of 2.26 eV and a direct E_G of 2.78 eV. It is primarily used for light emitting diodes. A wafer is transparent orange in color. Silicon is an elemental semiconductor with an indirect E_G of

1.12 eV and a direct E_G of 3.375 eV. It is used for integrated circuits and photovoltaics. It is metallic in color when polished. Table 2.1 summarizes the relevant properties of GaP and Si. The location of the conduction band is sufficiently reducing (see Figure 2-3) to drive the reduction of CO_2 and the valence band is sufficiently oxidizing to drive the oxidation of water. This makes this material attractive for a monolithic device for the splitting of CO_2.

2.4.2 p-GaP and p-Si Wafer Specifications as Received

Two inch diameter double polished (100) oriented *p*-GaP wafers were purchased from Promecome (now Azelis) electronics (France). With a zinc doped carrier concentration N_A, of $1\text{-}2\text{x}10^{18}$ cm^{-3} and an etch pitch density (EPD) less than $2\text{x}10^5$. They were grown via the liquid encapsulated Czochralski (LEC) method.

Three inch diameter single side polished (111) oriented *p*-Si wafers were purchased from University Wafer. With a boron doped carrier concentration, N_A of $1\text{-}2\text{x}10^{15}$ cm^{-3} and a resistivity of 5-7 ohm-cm.

2.4.3 Wafer Dicing of p-GaP and p-Si

Wafers were manually cut into smaller pieces by using a diamond tip scribe to notch the edge of wafer. In doing so, a crack propagates along an atomic plane yielding straight edges. The surface area of each piece was between 0.5 and 1 cm^2.

2.4.4 Ohmic Contacts to p-GaP and p-Si

Ohmic behavior describes a linear electrical current response to applied voltage as described by Ohm's law. In order to make ohmic contacts to *p*-type materials, a connection to the valence band is required, and conversely to the conduction band for *n*-type materials. In experiments performed for this thesis, the first electrical contacts to GaP were made by using a liquid indium-gallium (In-Ga) eutectic solder. A diamond tipped scribe was used to scratch the surface on one side of the GaP in the middle of a diced wafer piece. This was done to break through the native surface oxide layer. Then a small amount of the In-Ga was immediately applied. A copper wire inside a glass tube was placed in contact with the liquid solder and then the entire backside encapsulated by Devcon 5-minute epoxy. The glass tube was placed around the wire in order to prevent contact with the electrolyte solution during experiments. Example photographs of finished electrodes are shown in Figure 2-7. Multiple contacts were made to one GaP surface and the current voltage (I-V) characteristics probed using a potentiostat with the auxiliary electrode and reference electrode shorted (two electrode configuration). From the data it became apparent that the contacts were not ohmic due to the non-linear response. Rideout has reviewed III-V contacts describing the contact mechanism and behavior.[54] In-Ga contacts made to bare GaP showed Schottky behavior as show in Figure 2-8. When the surface was scribed the response improved, however it still showed a non-linear response. The pseudo-ohmic behavior near the origin resulted in measured values of 255 ohms (non-scribed) and 17.5 ohms (scribed). Other metals were also tried including evaporation of gold and palladium with subsequent annealing under nitrogen,

but did not yield ohmic contacts. For *p*-Si the In-Ga scribed contacts showed good ohmic behavior with 0.5 ohms of resistance and did not require further refinement.

The only literature graphs showing a linear I-V response are based on Au/Ni/Au-Ge on (111) and (100) *p*-GaP with either a hydrogen or nitrogen anneal at 400°C.[55] These metals showed improved behavior but still had a high contact resistance. One common practice to make ohmic contacts to a semiconductor is to dope a region heavily so that it is degenerate and behaves like a metal. This is often called a p++ region (or n++ for n-doped) and facilitates a low resistance metal contact pad area. Since the dopant of *p*-GaP is Zn, efforts were made to create such a region. Knowing that indium is a low melting point metal, and that an appropriate alloy will result in a melting point reduction at the eutectic point, the In-Zn phase diagram by Zakulski and Dutkiewicz[56] was consulted. Figure 2-9 shows the In-Zn phase diagram in the eutectic region, with $T_{eutectic} = 143.5°C$ at 2.2 weight % (wt%) zinc. Zn shot (99.99% Sigma-Aldrich) was cleaned via an HCl dip to remove surface oxide and rinsed with water. In wire (99.99% Sigma-Aldrich) was then added to a ceramic crucible and heated on a hot plate to the melting point, under a nitrogen atmosphere by using an inverted Büchner funnel. 4.6 wt% zinc was added and stirred until dissolution. An oxidized slag was removed from the liquid surface, resulting in an alloyed melting point ~190°C. The resulting soft metal alloy was then cut into small pieces with a razor blade. Scribed contacts were made to *p*-GaP and then the In-Zn alloy applied using a standard soldering iron. During this process the GaP substrate changes from orange to an orange-red color. The resulting final I-V trace is shown in Figure 2-7, with a measured resistance of 5.3 ohms and good ohmic behavior over several volts.

2.5   PHOTOELECTROCHEMISTRY OF *P*-GAP

2.5.1 Electrochemistry Preparation of Redox Species, Solvent, and Electrolyte

Electrochemistry is an analytical technique and very sensitive to impurities. In order to ensure reproducibility and accuracy, all aspects of the electrochemistry–the glass cell, electrodes, solvent, electrolyte, and redox species were kept extremely pure and clean. Redox couples were purified by recrystallization and counter ion exchange techniques as described below. The solvent was degassed and dried on a custom dry solvent system. The electrolyte was recrystallized in methanol. Electrochemistry was performed in a Vacuum atmospheres HE-493 dry box using a standard three electrode setup with a Bioanalytical systems CV-50 voltammetric analyzer.

2.5.1.1 Preparation of N,N'-dimethyl-4,4'-bipyridinium(PF$_6$)$_2$ [Methyl Viologen]

In a 50 mL round bottom flask 240 mg (1.5 mmol) of ammonium hexafluorophosphate (white solid, 99.5% Alfa-Aesar) was dissolved in 4 mL water. 100mg (0.4 mmol) of methyl viologen dichloride hydrate (white solid, 98%, Aldrich) was dissolved in 2 mL water and added dropwise to the solution. A white solid precipitate was collected over a medium glass frit, rinsed with water and dried overnight in a vacuum oven at 130 °C. Purity was confirmed via NMR and electroanalytical techniques.

2.5.1.2 *Preparation of Ru(2,2'-bipyridyl)$_3$(PF$_6$)$_2$ [Ru(bpy)$_3$]*

In a 50 mL round bottom flask 240 mg (1.5 mmol) of ammonium hexafluorophosphate (white solid, 99.5% Alfa-Aesar) was dissolved in 4 mL water. 200mg (0.27 mmol) of tris(2,2′-bipyridyl)dichlororuthenium hexahydrate (orange-red solid, 99.95%, Aldrich) was dissolved in 2 mL water and added dropwise to the solution. A bright orange solid precipitate was collected over a medium glass frit, rinsed with water and dried overnight in a vacuum oven at 130 °C. Purity was confirmed via NMR and electroanalytical techniques.

2.5.1.3 *Preparation of Tetrabutylammonium(PF)$_6$ [TBAH]*

In a 1000 mL beaker 100 g (258 mmol) of tetrabutylammonium hexafluorophosphate (white solid, 98% aldrich) was dissolved in 400 mL of methanol, continuously stirred, and brought to a boil for 15 minutes on a large hotplate. The beaker was placed in a freezer for 1 hour, along with 100 mL of methanol. The solution was then filtered in a large Büchner funnel with #1 Whatman filter paper and rinsed three times with cold methanol. The white precipitate collected was dried overnight in a vacuum oven at 130 °C.

2.5.2 *Native Oxide Etch of p-GaP*

GaP will spontaneously grow an oxide when exposed to air, reported to consist of Ga_2PO_4.[57] The oxide refractive index has been reported as $n_{GaP\ ox}$ = 1.5-1.6 and the GaP substrate n_{GaP} = 3.4-3.44.[58] Ellipsometry was used to confirm the native oxide thickness of ~3nm. The surface oxide will not have the electronic properties of the bulk and must be removed before performing any experiments. Kaminska and coworkers[58] have reported a very comprehensive list of acid combinations specifically for GaP and shown their respective etch rates, selectivity, and surface roughness characteristics. For the experiments performed in this thesis, a mixture of 3:1 $HCl:HNO_3$ (aqua regia) was used to remove the native oxide by dipping the electrode for one minute, then rinsing with water, and then drying with nitrogen immediately before electrochemistry.

2.5.3 *UV-VIS Measurement of the Band Gap of p-GaP*

A UV-VIS spectrophotometer is typically used to determine extinction coefficients and energetics of specific transitions of species in solution. However it can also be used to measure the band gap of a semiconductor. When light impinges on a surface it will be 1) reflected, 2) absorbed, and 3) transmitted. When the light has energy greater than the bandgap of a semiconductor, a portion is now absorbed, exciting an electron-hole pair (exciton). Equation 2-6 shows how to convert between energy (eV) and wavelength (λ) in nm using Planck's equation.

$$\lambda\,(nm) = \frac{1240}{E\,(eV)} \qquad \textbf{(2-6)}$$

By placing a piece of GaP in the beam path and then sweeping the wavelength of light the spectral response of GaP was obtained as shown in Figure 2-10. By normalizing the photoresponse curve (to account for reflection), the E_G will be at 50% relative transmission. The measured value of 2.27eV agrees well with the literature value in Table 2-1. This methodology is a rapid tool that can be used to verify the band gap, especially for compound semiconductors which can vary depending on the processing conditions.

2.5.4 Cyclic Voltammograms of p-GaP with Ru(bpy)₃ and Methyl Viologen

The original attempts at electrochemistry on *p*-GaP produced very frustrating results. Low photovoltages and photocurrents were observed and the electrochemistry was inconsistent. After consultations with Dr. Yu-Hwa Lo, Dr. Peter Asbeck, and Dr. Charles Tu, it became apparent that poor, non-ohmic contacts could be responsible for the observed behavior. Improvements in the contacts as explained in section 2.4.4 resulted in a greatly improved photoresponse. Figure 2-11 shows the cyclic voltammetry of *p*-GaP with and without broadband illumination with Ru(bpy)₃. A scan with a platinum electrode serves as an example of a more ideal electrochemical response. Note that the Saturated Calomel Electrode (SCE) is +241mV vs. the Normal Hydrogen Electrode (NHE),[59] and Ferrocene is +400mV with respect to SCE.[60] The observed photocurrent onset is around 900mV more anodic (positive) than the 1st reduction of Ru(bpy)₃. While this result is impressive, there are no distinct redox shapes on *p*-GaP. Moving to another good electron accepting redox couple, figure 2-12 shows the cyclic voltammetry using

methyl viologen. The photocurrent again shows no peaks and the resulting photovoltage is only 200mV to the onset. The poor photoresponse of GaP could be due to one or more of the following conditions: 1) poor surface kinetics, 2) no Fermi level pinning, or 3) insufficient photon flux so that the recombination dominates. Whichever the case may be, a change in semiconductor type to the well understood silicon was made to help elucidate the photoresponse. Nonetheless, GaP remains an attractive photoelectrode material for driven fuel forming reactions.

2.6 PHOTOELECTROCHEMISTRY OF *P*-SI

2.6.1 Native Oxide Etch of p-Si

Silicon possesses a native oxide SiO_2 of ~1nm that interferes with the electronic properties of the bulk and must be removed before performing any experiments. A common selective etch used in the processing of integrated circuits is buffered oxide etch (BOE), consisting of a 6:1 ratio of 40% NH_4F (aq) and 49% HF (aq). Extreme caution must be used when handling HF. Fresh BOE will remove the native oxide at a rate of 2nm s^{-1}. Only Teflon or plastic containers should be used, labeled, and disposed of properly. All work must be conducted in a fume hood using protective goggles, gloves, and acid smock. Fresh calcium gluconate must be available in case of accidental skin exposure. Piranha acid, 3:1 H_2SO_4: 30% H_2O_2 (aq) was first used to clean the surface of all organics. This is also a very dangerous procedure and should be exercised with caution. The acid must be slowly added to the water solution as it will get very hot and is

extremely oxidizing. A qualitative approach is to visually inspect the interaction of water and the surface. The silicon oxide surface is hydrophilic and the silicon surface is hydrophobic. A quantitative approach is to measure the surface contact angle as discussed in the next chapter. By dipping the electrode for five minutes in BOE and then rinsing with water, the silicon is ready for immediate electrochemistry. If the electrode is kept under an inert atmosphere, the surface will remain stable and oxide free.

2.6.2 Cyclic Voltammograms of p-Si with Ru(bpy)₃ and Methyl Viologen

Freshly etched silicon surface showed excellent reversible electrochemistry and consistent photocurrents with clearly defined photovoltages. Figure 2-12 and Figure 2-13 show the cyclic voltammetry of *p*-Si with and without broadband illumination. A scan with a platinum electrode serves as a reference electrochemical response. The observed photocurrent onset in Figure 2-12 is 470 mV more anodic (positive) than platinum for each reduction of Ru(bpy)₃. This observed behavior is consistent with Fermi level pinning because each individual redox couple is observed as separate waves.[42] When plotted the peak current versus the square root of the scan rate were linear on both platinum and on the *p*-Si surface, verifying freely diffusing homogeneous behavior.[59] The observed voltage shift reflects a direct conversion and transfer of photonic energy to electrochemical energy. The three electrode setup supplies the additional required voltage to drive reduction. It is worth noting that this configuration only observes the half reaction involved and ignores the auxiliary electrode reaction. While this is advantageous for probing the photoresponse, a complete two electrode system requires that the entire

voltage be provided by PEC and the counter electrode reaction is critical. Ideally if the voltage produced by the photoelectrode is large enough for both cathodic and anodic then the reduction and oxidizing reactions can be driven solely by light. The observed photocurrent onset in Figure 2-13 is 400 mV more anodic than platinum for each reduction of methyl viologen. This voltage is only slightly lower than the Ru(bpy)$_3$ case and shows excellent electrochemical reversibility. The response was stable and repeatable on additional substrates. The *p*-Si provides a good example of a more behaved system than *p*-GaP. This knowledge and experience is applied to electrocatalytic systems as will be explained in the next chapter.

2.6.3 Band Positions of p-GaP and p-Si With Redox Couples

The distance to the bottom of the conduction band from absolute vacuum level is given by the electron affinity χ as shown in Table 2-1. This is not to be confused with the work function φ, which measures the distance to the Fermi level, which will vary with dopant type and dopant concentration. For silicon χ occurs at -4.05 vs. vacuum (-0.631 vs. SCE) and for GaP -3.8 vs. vacuum (-0.881 vs. SCE). Equations 2-7 show how to convert χ from vacuum to NHE or SCE.[12]

$$E_{NHE} = -4.44 - E_{vacuum} = -4.44 + \chi_{semiconductor} \quad \textbf{(2-7a)}$$

$$E_{SCE} = -4.68 - E_{vacuum} = -4.68 + \chi_{semiconductor} \quad \textbf{(2-7b)}$$

With this understanding the results of *p*-Si and *p*-GaP can be further analyzed by showing the location of the bands and redox couples on the same reference scale. This is

shown schematically in Figure 2-15. For Silicon at pH = 0 only one of the redox couples ($MV^{+2/+1}$) is within the band gap. The others are at a more negative potential, yet we see a similar photovoltage shift for all couples. This strongly supports a surface pinning of the Fermi level as discuss in section 2.3.4.4. For GaP at pH = 0 both MV couples are inside the band gap region, while $Ru(bpy)_3$ couples are outside at more negative potentials. This may partially explain the large difference in observed photovoltage for the specific redox systems. A low 200mV photovoltage for MV is observed in figure 2-12, and a high photovoltage of 900mV for $Ru(bpy)_3$ in figure 2-13. Some sensitivity is therefore seen with the redox couple and may be only weakly pinned or not pinned at all. However as was mentioned earlier this could be a surface kinetic effect and needs further experimental evidence to be decided. The location of the band edges is a critical element of any photoelectrochemical device and the redox couple choice will affect the photoresponse.

2.7   CONCLUSIONS

An introduction to the field of semiconductor-liquid junctions was presented. There are five major factors in photoelectrochemistry that are presented in this chapter. They are: 1) band gap energy, 2) semiconductor doping type, 3) band edge positions, 4) surface pretreatment, and 5) redox couple location. The band gap determines the wavelengths of light that can be absorbed and converted to a photocurrent and photovoltage. Doping directly affects the PEC: *n*-type semiconductors are photoanodes

and dark cathodes, whereas *p*-type are photocathodes and dark anodes. The band edge position and redox couple location determines the direction and degree of band bending with the exception of Fermi level pinning. On *p*-Si the photovoltage is independent, whereas on *p*-GaP the photovoltage varies with redox species. Methodology for constructiong photoelectrodes for PEC experiments was shown. Removal of the surface native oxide improves the electronic properties of the photoelectrodes and yields excellent electrochemistry on *p*-Si. The photoresponse of *p*-Si shows: 1) a 475 mV shift in the required voltage as compared to platinum, 2) reversible electrochemical behavior, 3) and is Fermi level pinned. The photoresponse of *p*-Gap shows a varying degree of photovoltage from 200-900 mV as compared to platinum depending on the redox couples.

Chapter 2 and 3, in part, are currently being prepared for submission for publication of the material, entitled, "Light Assisted Homogeneous Electrocatalytic Reduction of Carbon Dioxide on p-Type Silicon Evidenced by Cyclic Voltammetry," written by Aaron J. Sathrum and Clifford P. Kubiak. The dissertation author was the primary investigator and author of this material.
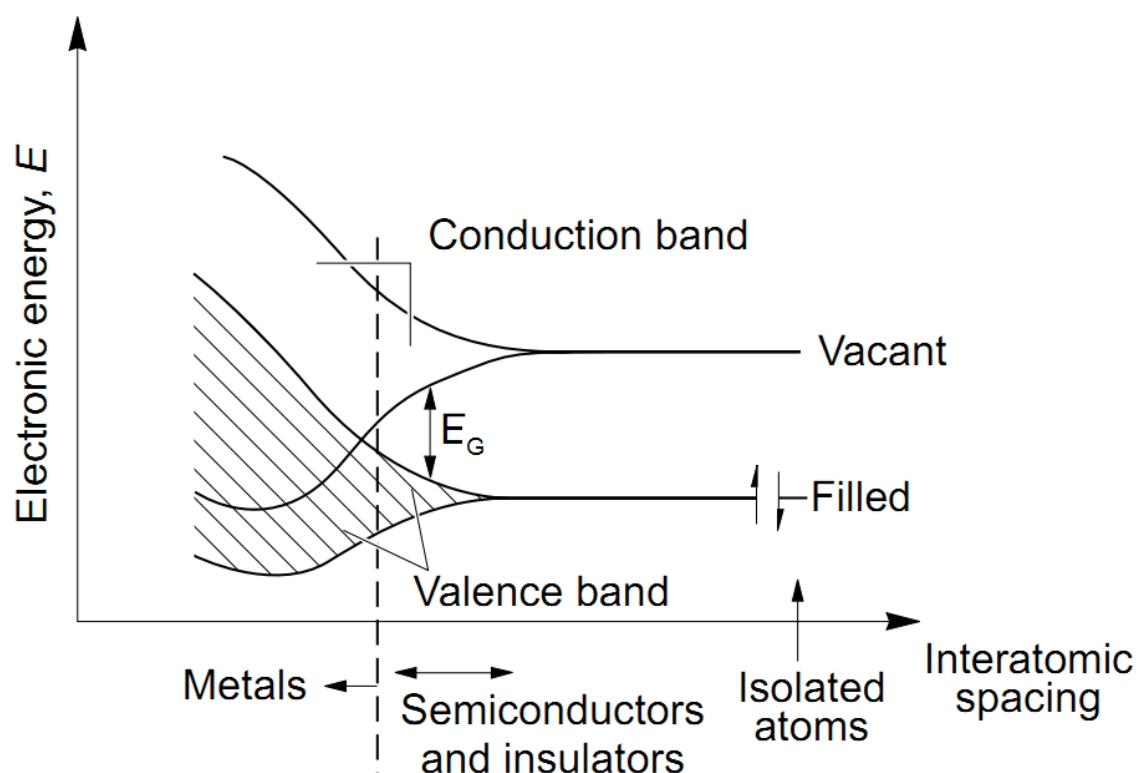
Figure 2-1 Discrete energy levels become a continuum of levels resulting in energy bands that eventually overlap with decreasing atomic distance. Figure adapted from Bott.[35]
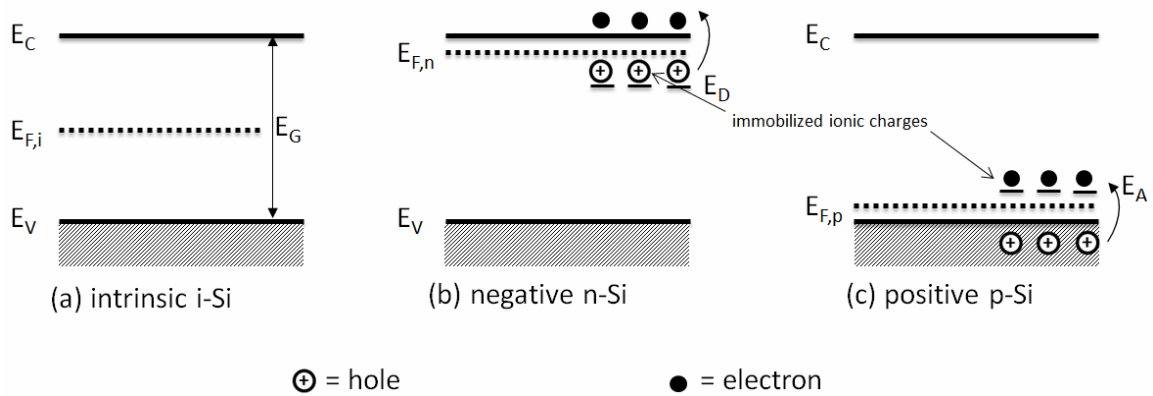
Figure 2-2   Energy band structure of an (a) intrinsic, (b) n-doped, (c) p-doped semiconductor. Shown are the conduction (lowest unoccupied) band (E_C), valence (highest occupied) band (E_V), Fermi level (E_F), donor level (E_D), acceptor level (E_A) and band gap (E_G). For silicon E_G = 1.107eV, for phosphorus E_D=0.044eV, for boron E_A=0.045eV.[61]
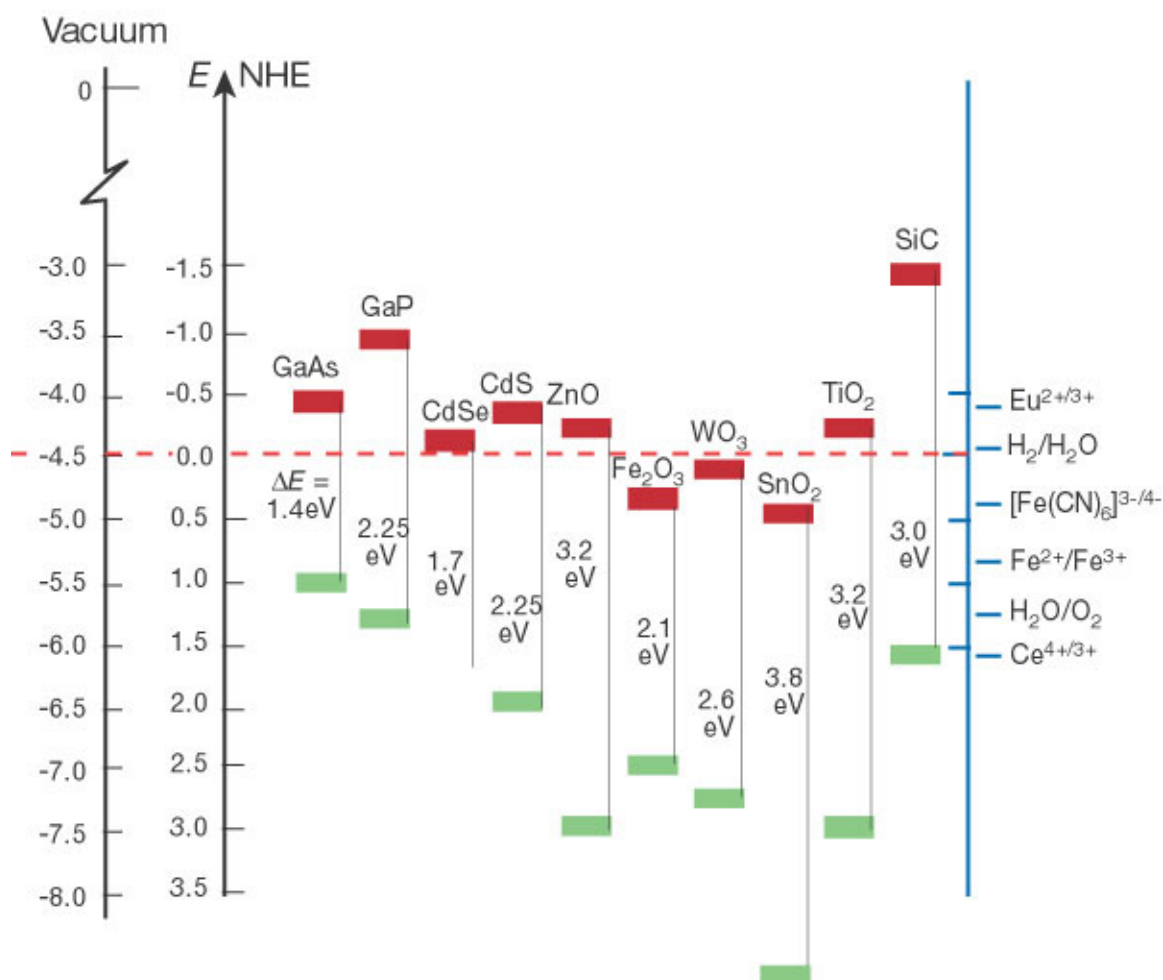
Figure 2-3 The upper edge of the valence band (Green) and the lower edge of the conduction band (Red) are shown for ten different semiconductor materials at pH 1 as compiled by Grätzel.[31] The left energy scale is referenced to both the vacuum level and the normal hydrogen electrode. The electron affinity (χ) is measured from the bottom of the conduction band to the vacuum level. The work function (φ) is measured from E_{vac} to E_F. The standard potentials of several redox couples are presented on the right side.
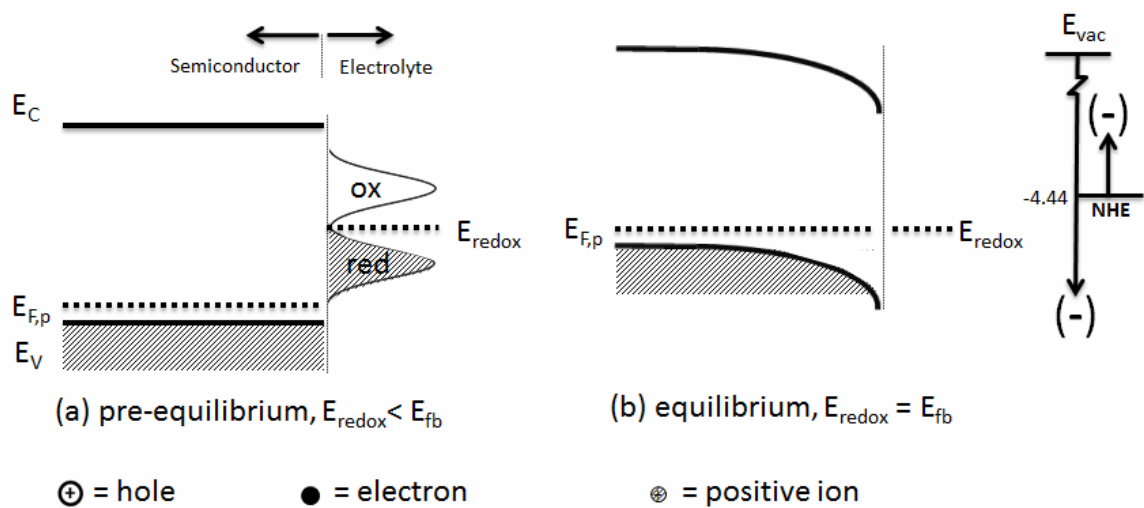
Figure 2-4 p-type semiconductor surface in contact with an electrolyte solution with species $E_{redox} < E_{F,p}$ (a) pre-equilibrium before band bending, (b) equilibrium with band bending.
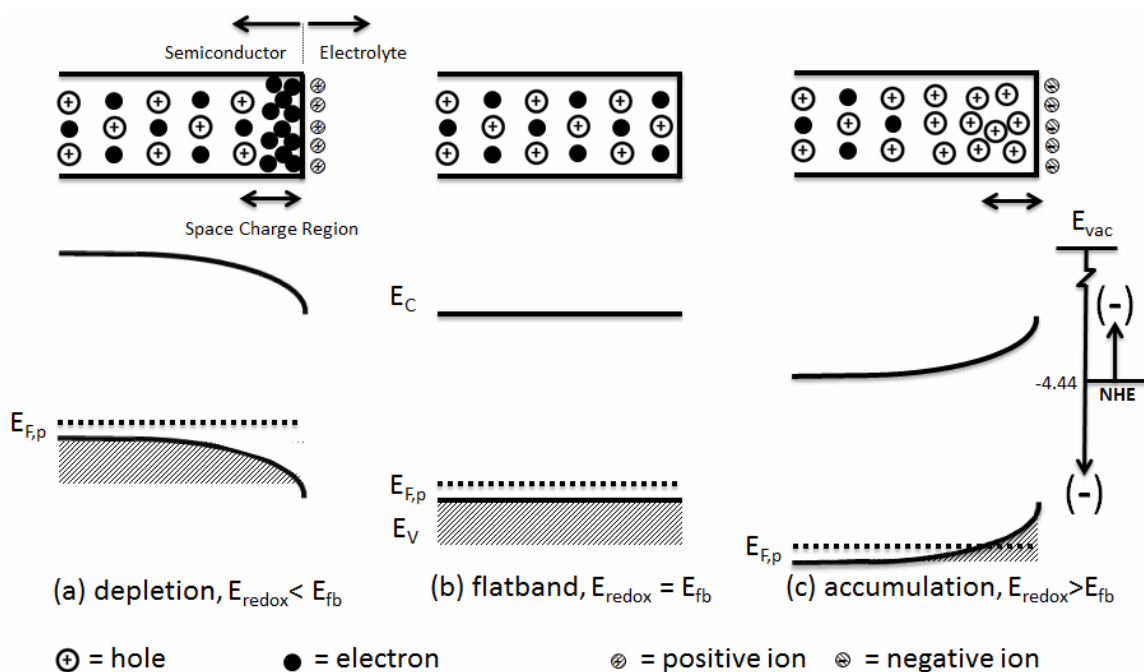
Figure 2-5 p-type semiconductor surface in contact with an electrolyte solution for: (a) depletion, (b) flatband, (c) accumulation. The top shows the distribution of charges in the semiconductor and in the solution near the surface. The bottom shows the band bending of a p-type semiconductor in contact with an electrolyte solution.
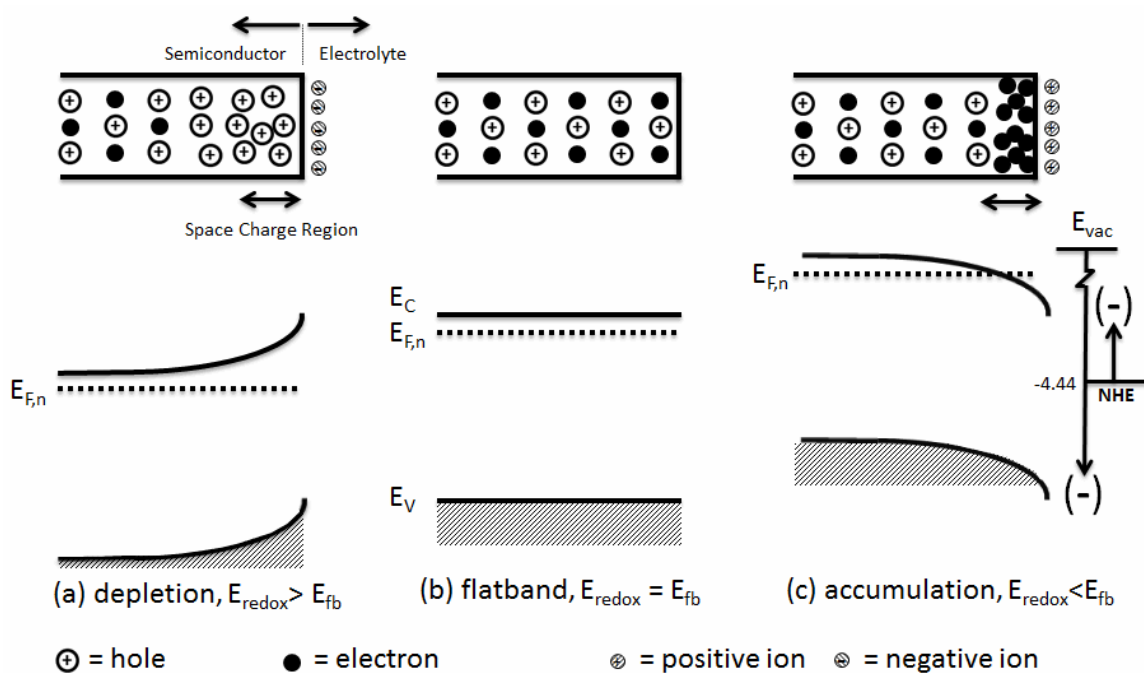
Figure 2-6 n-type semiconductor surface in contact with an electrolyte solution for: (a) depletion, (b) flatband, (c) accumulation. The top shows the distribution of charges in the semiconductor and in the solution near the surface. The bottom shows the band bending of an n-type semiconductor in contact with an electrolyte solution.

Table 2-1 Semiconductor properties of GaP and Silicon.

	Gallium Phosphide	Silicon	
Crystal Structure	Zinc Blende	Diamond	
E_G Band Gap	2.26	1.11	eV
E_C DOS	1.80E+19	3.20E+19	cm^{-3}
E_V DOS	1.90E+19	1.80E+19	cm^{-3}
E_A (Zn, GaP) or (B, Si)	0.0697	0.045	eV
Dielectric Constant (static)	11.1	11.7	
Electron Affinity	3.8	4.05	eV
Lattice Constant	0.54505	0.5431	nm
Electron Mobility	250	1400	$cm^{-2} V^{-1} s^{-1}$
Hole Mobility	150	450	$cm^{-2} V^{-1} s^{-1}$
Hole Lifetime N~10E18	1.00E-06	1.00E-06	s
Hole Diffusion Length	2.00E-05	1.00E-03	m
Electron Lifetime N~10E18	1.00E-07	4.00E-06	s
Electron Diffusion Length	7.00E-06	4.00E-03	m
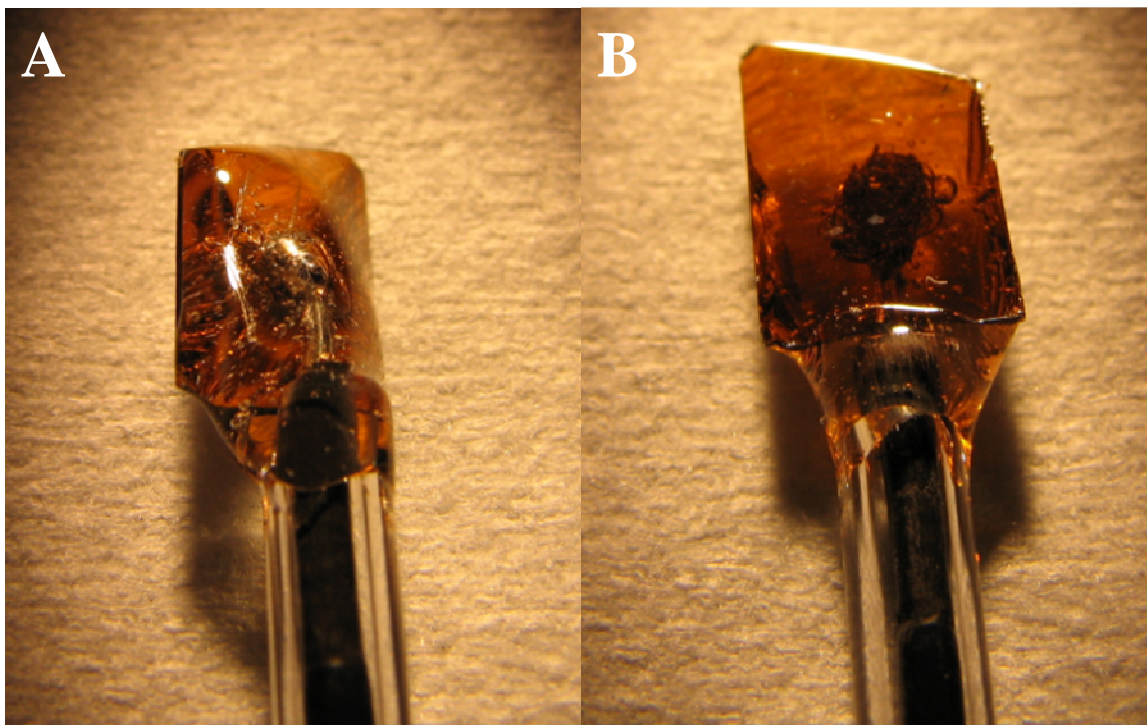
Figure 2-7 Photographs of constructed p-GaP electrodes. An In-Ga eutectic liquid solder contacts the GaP through a scribed contact. A copper wire inside a glass tube is inserted into the solder and then completely sealed with epoxy. Improved ohmic contacts were subsequently made using annealed 4.6 wt% Zn-In alloy. (a) backside sealed with epoxy, (b) frontside with surface exposed.
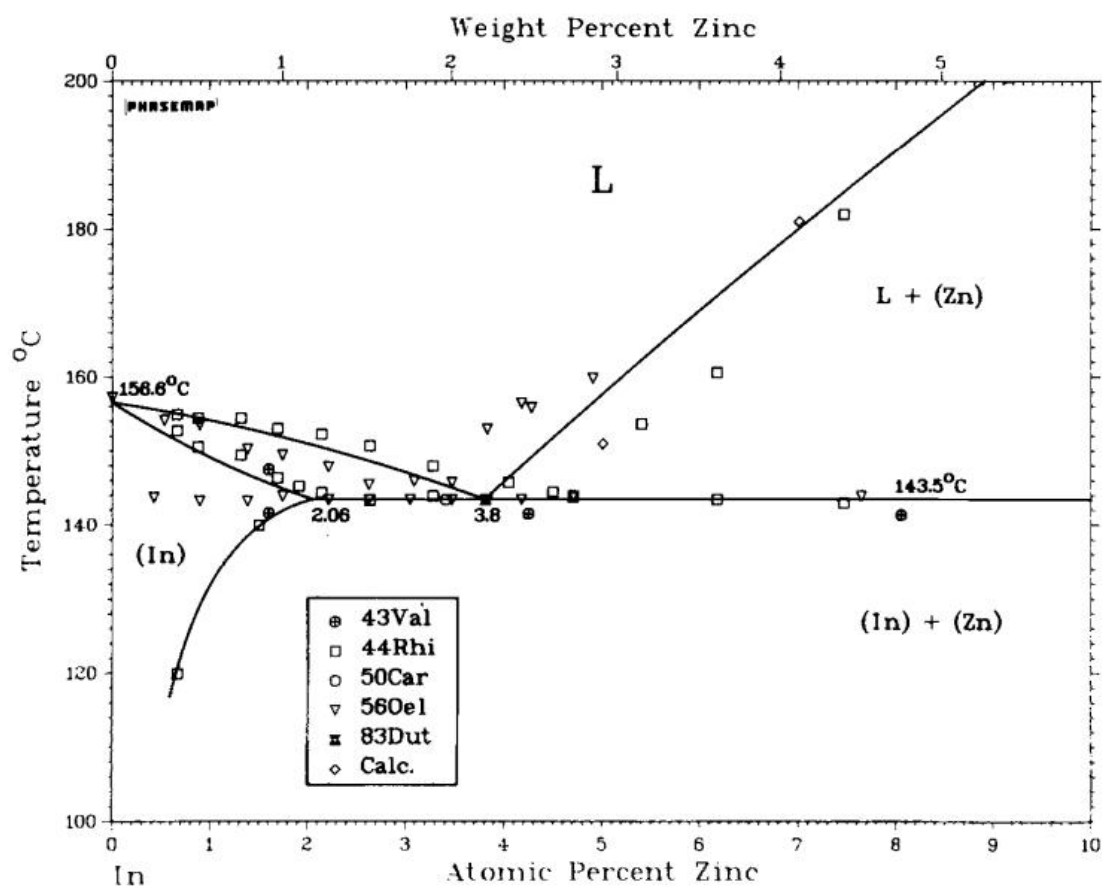
Figure 2-8 In-Zn phase diagram in the eutectic region, from Zakulski and Dutkiewicz.[56]
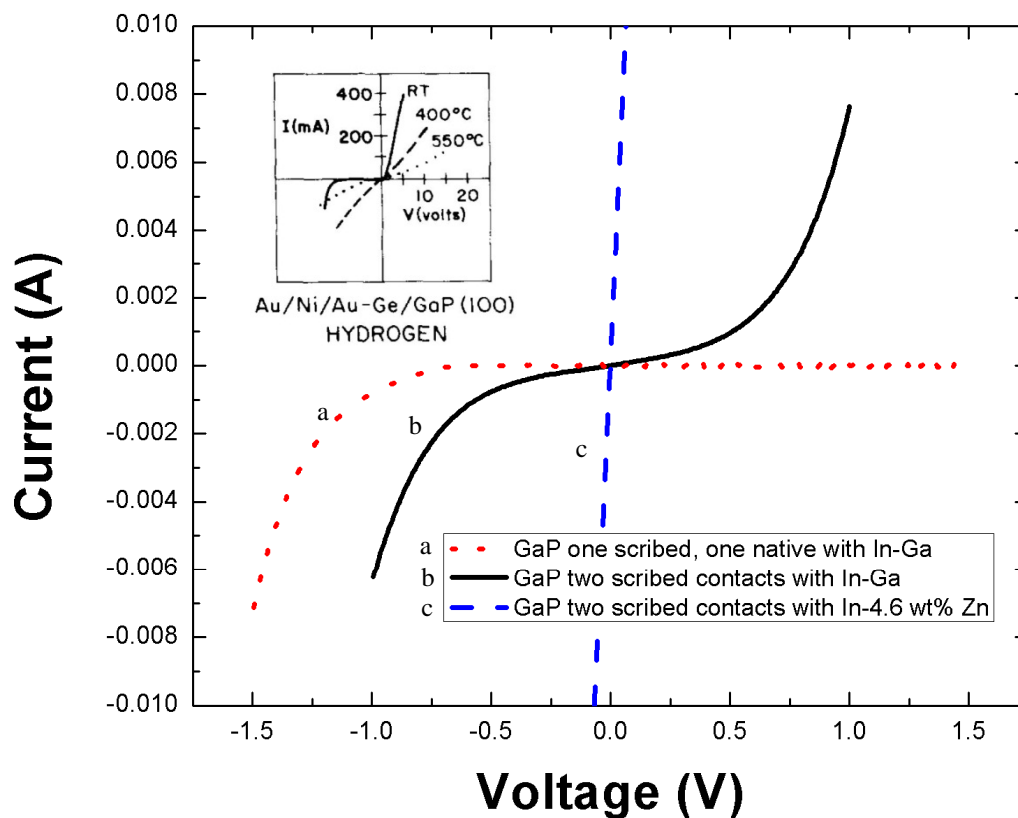
Figure 2-9 Current voltage plots of In-Ga and In-Zn contacts to p-GaP. The In-Ga show non-ohmic behavior while the In-Zn shows low resistance and ohmic behavior. Inset is similar observations on p-GaP using Au alloys from Ginley.[55] The measured resistances were as follows 255 ohms near the origin for one scribed, 17.5 near the origin for two scribed, and 5.3 ohms for the In-Zn alloy contact.
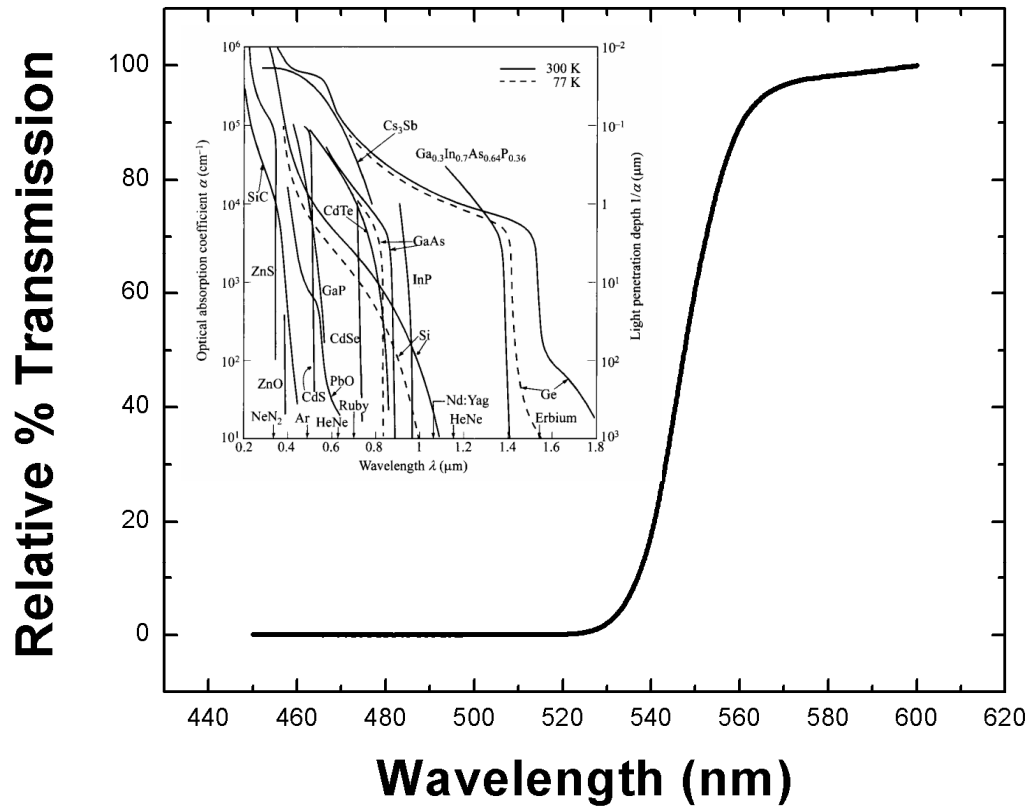
Figure 2-10 UV-VIS spectrum of p-GaP showing a 50% relative transmittance at 546 nm corresponding to a band gap of 2.27eV. At wavelengths $E_\lambda < E_G$ the semiconductor will reflect/transmit the light, and for $E_\lambda > E_G$ the light will be reflected/absorbed. Inset shows the absorption coefficient and penetration depth for a variety of semiconductor materials from Sze.[62]
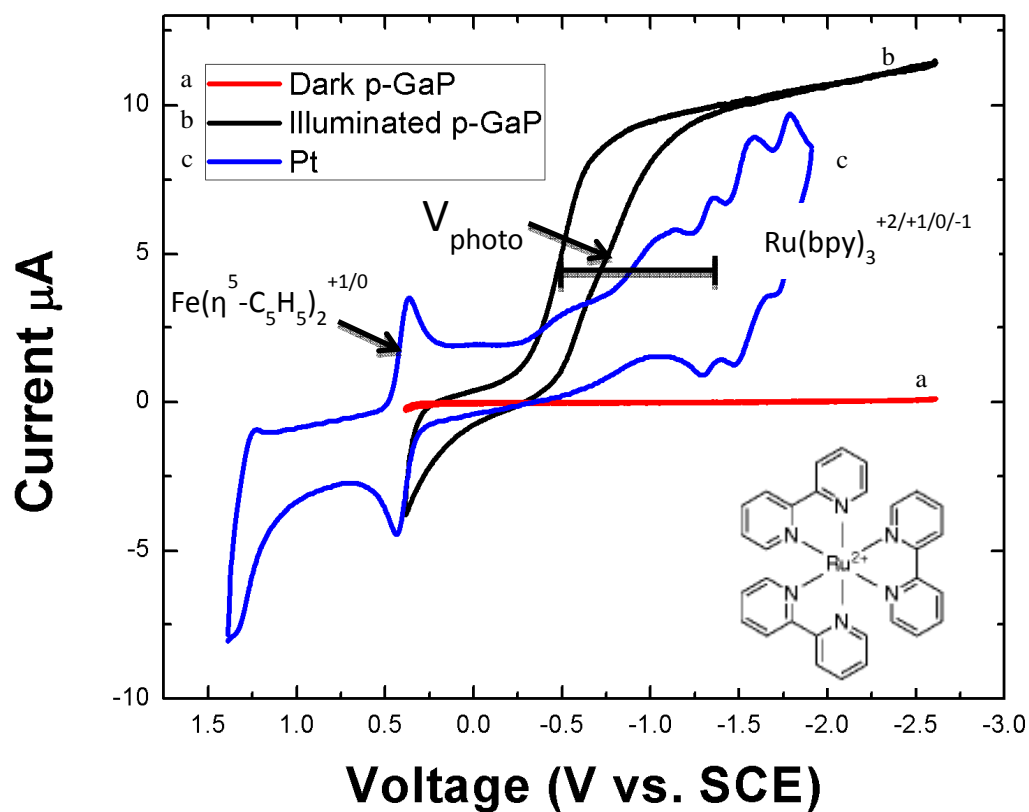
Figure 2-11 Cyclic voltammograms of 1mM Ru(2,2′-bipyridyl) $_3$(PF$_6$)$_2$ on a platinum electrode and on an illuminated p-GaP photocathode. V$_{photo}$~900mV but shows poor surface kinetics. Conditions: N$_2$ purged CH$_3$CN with 0.1M (n-butyl)$_4$N(PF$_6$), scan rate 100 mV/s, platinum counter, with ferrocene[+1/0] as an internal standard.
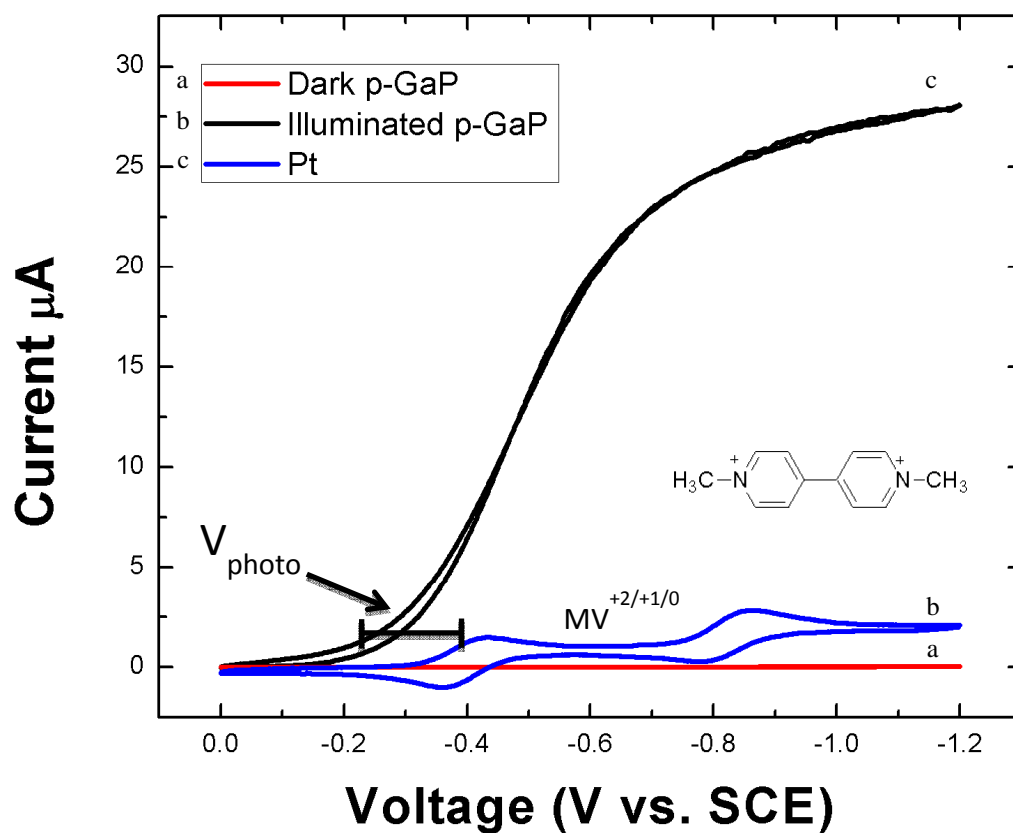
Figure 2-12 Cyclic voltammograms of 1mM N,N′-dimethyl-4,4′-bipyridinium (PF$_6$)$_2$ electrode and on a platinum electrode and on an illuminated p-GaP photocathode. V$_{photo}$~200mV with poor surface kinetics. Conditions: N$_2$ purged CH$_3$CN with 0.1M (n-butyl)$_4$N(PF$_6$), scan rate 10 mV/s, platinum counter, with ferrocene$^{+1/0}$ as an internal standard.
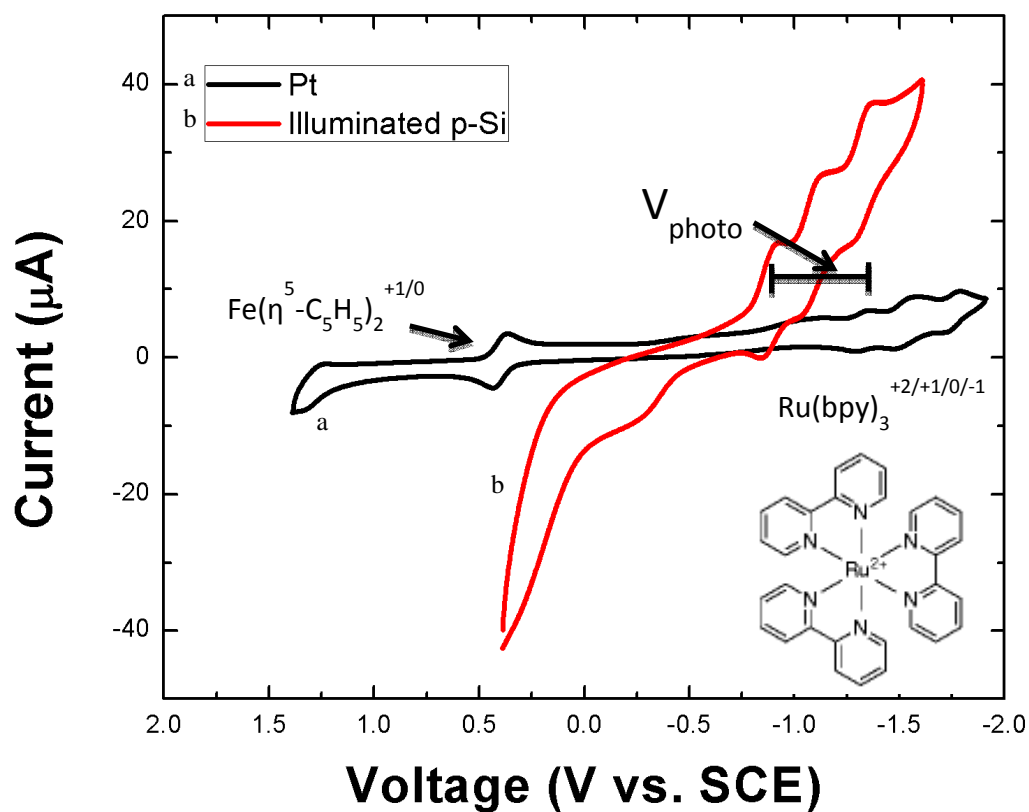
Figure 2-13 Cyclic voltammograms of 1mM Ru(2,2′-bipyridyl) $_3$(PF$_6$)$_2$ on a platinum electrode and on an illuminated p-Si photocathode. V$_{photo}$~465-475mV for all three couples. Conditions: N$_2$ purged CH$_3$CN with 0.1M (n-butyl)$_4$N(PF$_6$), scan rate 100 mV/s, platinum counter, with ferrocene[+1/0] as an internal standard.
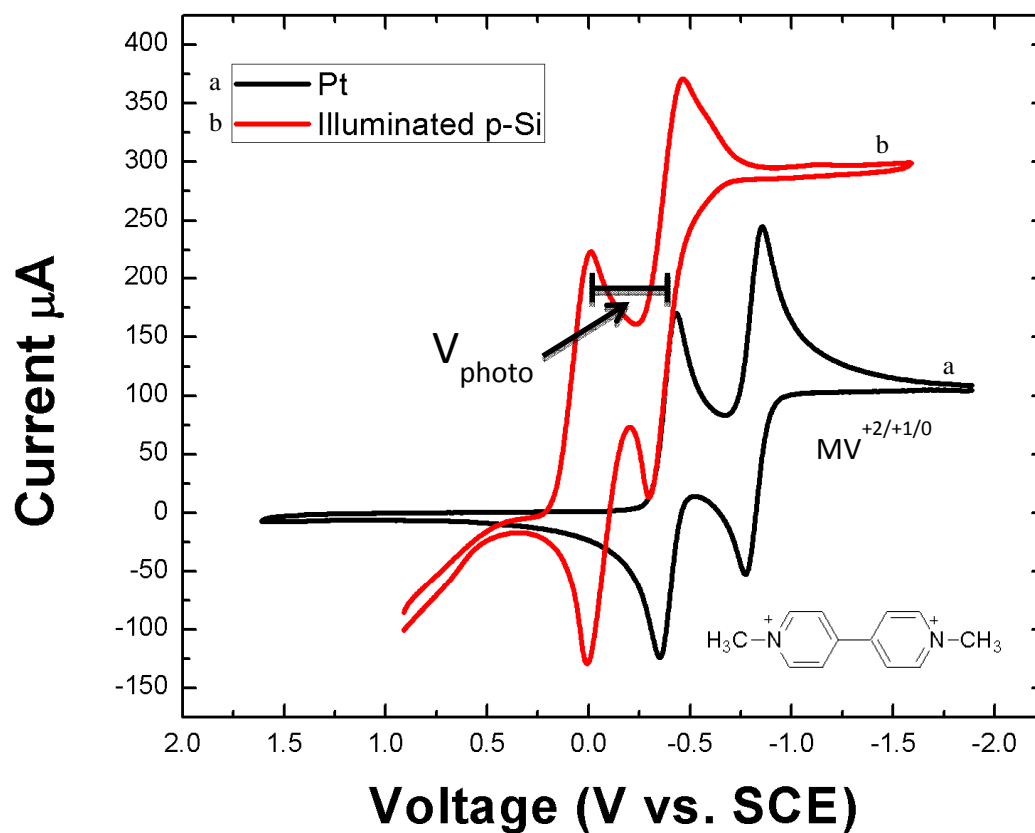
Figure 2-14 Cyclic voltammograms of 1.4mM N,N′-dimethyl-4,4′-bipyridinium $(PF_6)_2$ on a platinum electrode and on an illuminated p-Si photocathode. V_{photo}~400mV Conditions: N_2 purged CH_3CN with 0.1M $(n-butyl)_4N(PF_6)$, scan rate 100 mV/s, platinum counter, with ferrocene[+1/0] as an internal standard.
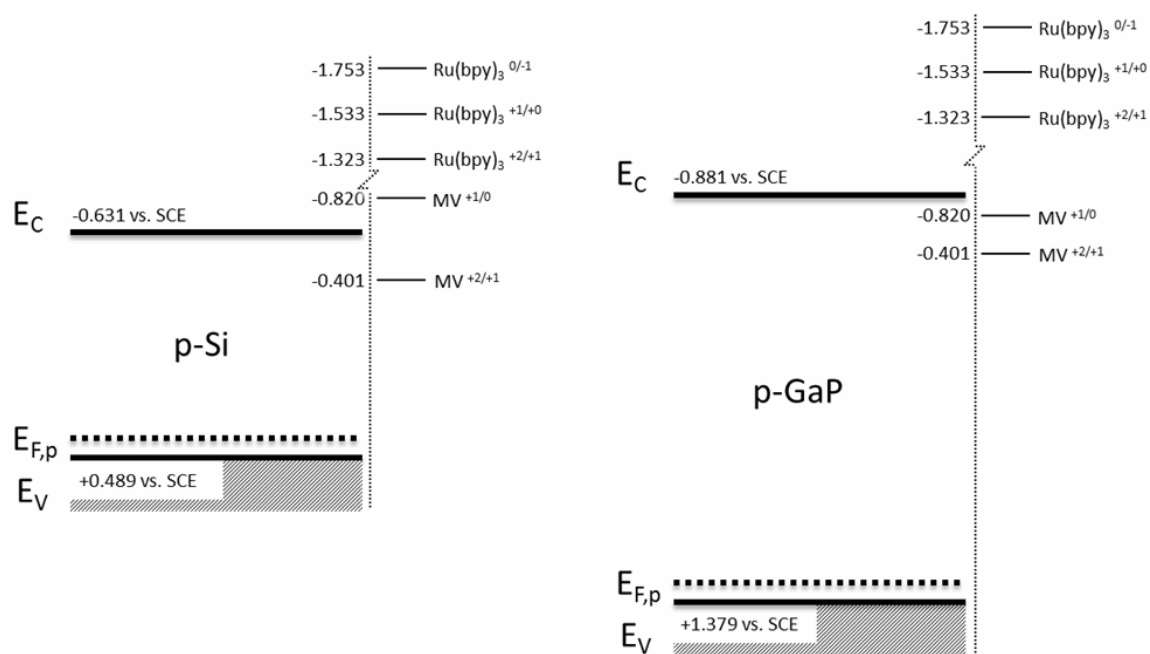
Figure 2-15 Band positions of p-Si and p-GaP with the MV and Ru(bpy)$_3$ redox couples vs. SCE. E_C and E_V are for pH = 0.

2.8 REFERENCES

(1)   Belessiotis, V.; Delyannis, E. The history of renewable energies for water desalination. *Desalination* **2000**, *128*, 147-159.

(2)   Bequerel, E. Recherches sur les effets de la radiation chimique de la lumière solaire, au moyen des courants électriques. *C.R. Acad. Sci.* **1839**, *9*, 145-149.

(3)   Brattain, W. H.; Garrett, C. G. B. Experiments on the Interface Between Germanium and an Electrolyte. *Bell System Tech. Journal* **1955**, *34*, 129-176.

(4)   Gerische.H. Electrochemical Behavior of Semiconductors Under Illumination. *J. Electrochem. Soc.* **1966**, *113*, 1174-&.

(5)   Koval, C. A.; Howard, J. N. Electron-Transfer at Semiconductor Electrode Liquid Electrolyte Interfaces. *Chem. Rev.* **1992**, *92*, 411-433.

(6)   Bak, T.; Nowotny, J.; Rekas, M.; Sorrell, C. C. Photo-Electrochemical Hydrogen Generation from Water Using Solar Energy. Materials-Related Aspects. *Int. J. Hydrog. Energy* **2002**, *27*, 991-1022.

(7)   Licht, S. Multiple Band Gap Semiconductor/Electrolyte Solar Energy Conversion. *J. Phys. Chem. B* **2001**, *105*, 6281-6294.

(8)   Lewerenz, H. J. Surface Scientific Aspects in Semiconductor Electrochemistry. *Chem. Soc. Rev.* **1997**, *26*, 239-246.

(9)   Nozik, A. J.; Memming, R. Physical Chemistry of Semiconductor-Liquid Interfaces. *J. Phys. Chem.* **1996**, *100*, 13061-13078.

(10)   Carlsson, P.; Holmstrom, B. Photoelectrochemical Cells - Laboratory Determination of Solar Conversion Efficiencies. *Sol. Energy* **1986**, *36*, 151-157.

(11)   Decker, F.; Fracastorodecker, M.; Moro, J. R.; Motisuke, P. Optical Losses in Solar Photoelectrochemical Cells. *Sol. Cells* **1987**, *20*, 19-26.

(12)   Bard, A. J.; Memming, R.; Miller, B. Terminology in Semiconductor Electrochemistry and Photoelectrochemical Energy-Conversion. *Pure Appl. Chem.* **1991**, *63*, 569-596.

(13)   Archer, M. D.; Bolton, J. R. Requirements for Ideal Performance of Photochemical and Photovoltaic Solar-Energy Converters. *J. Phys. Chem.* **1990**, *94*, 8028-8036.

(14)   Peter, L. M. Dynamic Aspects of Semiconductor Photoelectrochemistry. *Chem. Rev.* **1990**, *90*, 753-769.

(15)   Nozik, A. J. Photoelectrochemistry - Introductory Lecture. *Faraday Discuss.* **1980**, *70*, 7-17.

(16)   Archer, M. D. Electrochemical Aspects of Solar-Energy Conversion. *J. Appl. Electrochem.* **1975**, *5*, 17-38.

(17)   Salvador, P. Semiconductors Photoelectrochemistry: A Kinetic and Thermodynamic Analysis in the Light of Equilibrium and Nonequilibrium Models. *J. Phys. Chem. B* **2001**, *105*, 6128-6141.

(18)   Gratzel, M. Photovoltaic and Photoelectrochemical Conversion of Solar Energy. *Philos. Trans. R. Soc. A-Math. Phys. Eng. Sci.* **2007**, *365*, 993-1005.

(19)   Nozik, A. J. Electrode Materials for Photoelectrochemical Devices. *J. Cryst. Growth* **1977**, *39*, 200-209.

(20)   Bard, A. J. Design of Semiconductor Photo-Electrochemical Systems for Solar-Energy Conversion. *J. Phys. Chem.* **1982**, *86*, 172-177.

(21)   Harris, L. A.; Wilson, R. H. Semiconductors for Photoelectrolysis. *Annu. Rev. Mater. Sci.* **1978**, *8*, 99-134.

(22)   Rajeshwar, K. Materials Aspects of Photoelectrochemical Energy-Conversion. *J. Appl. Electrochem.* **1985**, *15*, 1-22.

(23)   Memming, R. Photoelectrochemical Solar-Energy Conversion. *Top. Curr. Chem.* **1988**, *143*, 79-112.

(24)   Reichman, J. The Current-Voltage Characteristics of Semiconductor-Electrolyte Junction Photo-Voltaic Cells. *Appl. Phys. Lett.* **1980**, *36*, 574-577.

(25)   Haneman, D.; Miller, D. J.; Desilva, K. T. L.; McCann, J. F. Solar-Energy Conversion by Photoelectrochemical Cells. *J. Electroanal. Chem.* **1981**, *118*, 101-113.

(26)   Wrighton, M. S. Photoelectrochemistry - Inorganic Photochemistry at Semiconductor Electrodes. *J. Chem. Educ.* **1983**, *60*, 877-881.

(27)   Bard, A. J. Photoelectrochemistry and Solar-Energy - Progress, Promise and Problems. *J. Electroanal. Chem.* **1984**, *168*, 5-20.

(28)   Parkinson, B. On the Efficiency and Stability of Photoelectrochemical Devices. *Accounts Chem. Res.* **1984**, *17*, 431-437.

(29)   Mills, A.; LeHunte, S. An Overview of Semiconductor Photocatalysis. *J. Photochem. Photobiol. A-Chem.* **1997**, *108*, 1-35.

(30)   Bard, A. J. Photoelectrochemistry. *Science* **1980**, *207*, 139-144.

(31)   Gratzel, M. Photoelectrochemical Cells. *Nature* **2001**, *414*, 338-344.

(32)   Wrighton, M. S. Thermodynamics and Kinetics Associated with Semiconductor-Based Photoelectrochemical Cells for the Conversion of Light to Chemical Energy. *Pure Appl. Chem.* **1985**, *57*, 57-68.

(33)   Memming, R. Solar-Energy Conversion by Photoelectrochemical Processes. *Electrochim. Acta* **1980**, *25*, 77-88.

(34)   Butler, M. A.; Ginley, D. S. Principles of Photoelectrochemical, Solar-Energy Conversion. *J. Mater. Sci.* **1980**, *15*, 1-19.

(35)   Bott, A. W. Electrochemistry of Semiconductors. *Current Separations* **1998**, *17*, 87-91.

(36)   Schottky, W. Semiconductor Theory of Blocking-Layer and Point Rectifier. *Z. Phys.* **1939**, *113*, 367-414.

(37)   Schottky, W. Simplified and Extended Theory of Boundary Layer Rectifier. *Z. Phys.* **1942**, *118*, 539-542.

(38)   Mott, N. F. The Theory of Crystal Rectifiers. *Proc. R. Soc. of London-A. Math. and Phys. Sci.* **1939**, *171*, 27-38.

(39)   Nozik, A. J. Photoelectrochemistry -Applications to Solar-Energy Conversion. *Annu. Rev. Phys. Chem.* **1978**, *29*, 189-222.

(40)   Sprunken, H. R.; Schumacher, R.; Schindler, R. N. Evaluation of the flat-band potentials by measurements of anodic/cathodic photocurrent transitions. *Faraday Discussions of the Chemical Society* **1980**, *70*, 55-66.

(41)   Gomes, W. P.; Cardon, F. Electron Energy Levels in Semiconductor Electrochemistry. *Prog. Surf. Science* **1982**, *12*, 155-215.

(42)   Bard, A. J.; Bocarsly, A. B.; Fan, F. R. F.; Walton, E. G.; Wrighton, M. S. The Concept of Fermi Level Pinning at Semiconductor/Liquid Junctions. Consequences for Energy Conversion Efficiency and Selection of Useful Solution Redox Couples in Solar Devices. *J. Am. Chem. Soc.* **1980**, *102*, 3671-3677.

(43)   Bocarsly, A. B.; Bookbinder, D. C.; Dominey, R. N.; Lewis, N. S.; Wrighton, M. S. Photoreduction at Illuminated p–Type Semiconducting Silicon Photoelectrodes. Evidence for Fermi Level Pinning. *J. Am. Chem. Soc.* **1980**, *102*, 3683-3688.

(44)   Fan, F. R. F.; Bard, A. J. Semiconductor Electrodes. 24. Behavior of Photoelectrochemical Cells Based on p-type Gallium Arsenide in Aqueous Solutions. *J. Am. Chem. Soc.* **1980**, *102*, 3677-3683.

(45)   Bard, A. J.; Fan, F.-R. F.; Gioda, A. S.; Nagasubramanian, G.; White, H. S. On the role of surface states in semiconductor electrode photoelectrochemical cells. *Farad. Disc. Chem. Soc.* **1980**, *70*, 19-31.

(46)   Green, M. Electrochemistry of the Semiconductor-Electrolyte Electrode. 1. Electrical Double Layer. *J. Chem. Phys.* **1959**, *31*, 200-203.

(47)   Chiaradia, P.; Fanfoni, M.; Nataletti, P.; De Padova, P.; Brillson, L. J.; Slade, M. L.; Viturro, R. E.; Kilday, D.; Margaritondo, G. Fermi-Level Pinning and Intrinsic Surface States in Cleaved GaP. *Phys. Rev. B* **1989**, *39*, 5128.

(48)   O'Regan, B.; Gratzel, M. A Low-Cost, High-Efficiency Solar Cell Based on Dye-Sensitized Colloidal TiO2 Films. *Nature* **1991**, *353*, 737-740.

(49)   Nazeeruddin, M. K.; Kay, A.; Rodicio, I.; Humphry-Baker, R.; Mueller, E.; Liska, P.; Vlachopoulos, N.; Graetzel, M. Conversion of Light to Electricity by *cis*-X$_2$bis(2,2'-bipyridyl-4,4'-dicarboxylate)ruthenium(II) Charge-Transfer Sensitizers (X = Cl$^-$, Br$^-$, I$^-$, CN$^-$, and SCN$^-$) on Nanocrystalline Titanium Dioxide Electrodes. *J. Am. Chem. Soc.* **1993**, *115*, 6382-6390.

(50)   Fujishima, A.; Honda, K. Electrochemical Photolysis of Water at a Semiconductor Electrode. *Nature* **1972**, *238*, 37-+.

(51)   Graetzel, M. Artificial Photosynthesis: Water Cleavage Into Hydrogen and Oxygen by Visible Light. *Accounts Chem. Res.* **1981**, *14*, 376-384.

(52)   Inoue, T.; Fujishima, A.; Konishi, S.; Honda, K. Photoelectrocatalytic Reduction of Carbon Dioxide in Aqueous Suspensions of Semiconductor Powders. *Nature* **1979**, *277*, 637-638.

(53)   Barber, J. Photosynthetic Energy Conversion: Natural and Artificial. *Chem. Soc. Rev.* **2009**, *38*, 185-196.

(54)   Rideout, V. L. Review of Theory and Technology for Ohmic Contacts to Group III-V Compound Semiconductors. *Solid-State Electron.* **1975**, *18*, 541-550.

(55)   Ginley, R. A.; Chung, D. D. L.; Ginley, D. S. Structural Effects of Heating Gold-Based Contacts to Gallium Phosphide. *Solid-State Electron.* **1984**, *27*, 137-146.

(56)   Dutkiewicz, J.; Zakulski, W. The In–Zn (Indium–Zinc) System. *J. Phase Equilibria* **1984**, *5*, 284-289.

(57)   Kato, Y.; Geib, K. M.; Gann, R. G.; Brusenback, P. R.; Wilmsen, C. W. Thermal-Oxidation of GaP. *J. Vac. Sci. Technol. A-Vac. Surf. Films* **1984**, *2*, 588-592.

(58)   Kaminska, E.; Piotrowska, A.; Kaminska, A.; Klimkiewicz, M. Etching Procedures for GaP Surfaces. *Surf. Tech.* **1981**, *12*, 205-215.

(59)   Bard, A. J. F., L. R *Electrochemical Methods: Fundamentals and Applications*, 2nd Edition ed.; John Wiley & Sons, Inc., 2001.

(60)   Connelly, N. G.; Geiger, W. E. Chemical Redox Agents for Organometallic Chemistry. *Chem. Rev.* **1996**, *96*, 877-910.

(61)   Shackelford, J. F. *Introduction to Materials Science for Engineers*, 5th ed.; Prentice Hall: Upper Saddle River, NJ, 2000.

(62)   Sze, S. M. N., Kwok K. *Physics of Semiconductor Devices*, 3rd Edition ed.; John Wiley & Sons, Inc., 2007.

CHAPTER 3

PHOTO–ASSISTED ELECTROCATALYTIC HOMOGENEOUS REDUCTION OF CARBON DIOXIDE AT P–TYPE SILICON

3.1 ABSTRACT

The photoelectrocatalytic production of carbon monoxide using carbon dioxide as a feedstock demonstrates the capture of solar energy and subsequent electrochemical conversion into a useful chemical commodity. Carbon dioxide is reduced at illuminated p–Silicon (p–Si) cathodes using the electrocatalyst *fac*–Re(2,2'–bipyridyl)CO_3Cl at a 440 mV less anodic potential when compared to a glassy carbon electrode. This room temperature reduction shows that p–Si photocathodes effectively convert broadband optical energy into electrical energy that is directly transferred to an electrocatalyst for the reduction of CO_2. Selective production of carbon monoxide is confirmed by gas chromatography. Cyclic voltammograms of the electrocatalyst with CO_2 show an increase in current at the second reduction wave. Additional voltammograms performed using illuminated p–Si show the integrity of electrocatalytic activity shifted to more anodic potentials.

3.2 INTRODUCTION

Capturing energy from the sun to facilitate the renewable conversion of CO_2 into useful chemical commodities creates a carbon neutral cycle. This cycle is currently out of balance on a global scale and new approaches to reducing CO_2 levels are needed. CO_2 is abundant and the motivations for utilization arise from its global contribution to the greenhouse effect. CO_2 conversion is not a foreign reaction; plants successfully accomplish this on a global scale of more than 100 billion tons per year via

photosynthesis.[1] Major synthetic targets for conversion include carbon monoxide, methanol, formaldehyde and formic acid.[2] These commodities can be readily integrated into the existing chemical industry infrastructure. For example, carbon monoxide and hydrogen (synthesis gas) can be combined to produce liquid fuels via Fischer–Tropsch technology.[3] The major approaches to transforming CO_2 are chemical, photochemical, electrochemical, biological, reforming, and inorganic.[4] Each method requires an external source of energy to drive the thermodynamically uphill reaction ($\Delta G=257$ kJ mol^{-1} or 1.33V for $CO_2 \rightarrow CO + \frac{1}{2}O_2$). Desired qualities of a CO_2 conversion system are rapid conversion and high selectivity. An activation barrier E_A, or in electrochemical terms an overpotential η, exists for CO_2 conversion intermediates and consequently it is preferable to use a catalyst to lower the barrier. Currently there are no artificial systems that adequately accomplish CO_2 transformation efficiently. Utilization of CO_2 is considered a difficult problem because the conversion process requires multiple electrons coupled with multiple protons (PCET).[5] The high energy barrier for the one electron reduction of CO_2 to $CO_2^{\bullet-}$ at -1.90V vs. NHE is due to the large reorganization energy from the linear molecule to the bent radical anion.[6] Homogeneous electrocatalysis presents a unique opportunity to convert and store electrical energy in CO_2 derived products at low input energy. For example, a natural enzyme, formate dehydrogenase has recently been shown to operate at the thermodynamic potential with no overvoltage for CO_2 to formate and the reverse reaction, but the biological system suffers from immediate decay outside its natural environment.[7] Artificial systems built with transition metal complexes exhibit poor overpotentials typically between 0.5–1 volt.[8] The electrocatalyst *fac*–Re(2,2'–

bipyridyl)CO_3Cl[9] (Re(bpy)) is remarkable for its high selectivity, stability, and turnover frequency for conversion of CO_2 to CO.[10] By using a synthetic photoelectrochemical approach,[11] solar energy can be directly converted on a semiconductor surface to drive the electrocatalysis as shown in Figure 3-1. This assumes that the photovoltage is sufficient to drive both the cathodic and anodic reactions. Otherwise, external energy via an additional voltage source will be needed. Both the fixation of a greenhouse gas and the synthesis of chemical commodities can be attained in a renewable fashion by using electrocatalytic CO_2 photoelectrochemistry.

3.3 EXPERIMENTAL

3.3.1 Preparation of fac–Re(2,2'–bipyridyl)CO₃Cl

All chemicals were analytical grade or higher. *fac*–Re(2,2'–bipyridyl)CO_3Cl (Re(bpy)) was prepared via literature methods with small modifications.[12,13] In a 250 mL round bottom flask 0.5 g (1.3 mmol) of $Re(CO)_5Cl$ (white fine crystalline solid, Sigma-Aldrich 98%) and 0.216 (1.3 mmol) of 2-2'bipyridine (large clear crystals, Alfa-Aesar) were dissolved in toluene and refluxed (110 °C) for 1 hour. Upon heating, the solution immediately changed from colorless to yellow. When cooled to room temperature a yellow precipitate formed. The solid was filtered over a medium frit, washed twice with diethyl ether, and dried under vacuum. Purity was confirmed using NMR, and IR. ^{1}H NMR spectra were recorded on a Varian Mercury 300 MHz spectrometer. Infrared

spectra were collected on a Bruker Equinox 55 spectrometer. IR (CH_3CN) ν(CO): 2026 cm^{-1}, 1920 cm^{-1}, 1902 cm^{-1}.

3.3.2 Electrochemistry Setup

Tetrabutylammonium hexafluorophosphate (TBAH) electrolyte (Sigma–Aldrich 98%) was recrystallized in ethanol and dried under vacuum for 24 hours at 100°C. Acetonitrile was degassed and dried on a custom dry solvent system. Anhydrous N,N-Dimethylformamide (DMF) (Sigma-Aldrich 99.8%) was kept in a dry box. A BAS CV–50W voltammetric analyzer was used in all electrochemical experiments. Platinum electrodes (1 mm diameter), glassy carbon electrodes (3 mm diameter), and an $Ag^{+/0}$ non-aqueous reference electrode were purchased from Bioanalytical systems. Scans were conducted in 0.1 M TBAH in acetonitrile at 100 mV/sec unless otherwise noted. The platinum wire counter electrode was cleaned with a piranha etch (3 H_2SO_4 : 1 H_2O) and hydrogen flame annealed prior to use. The reference electrode consisted of a glass tube equipped with a vycor tip containing a silver wire and a 0.01M solution of $AgPF_6$ ($Ag^{+/0}$) in acetonitrile, with 0.1M TBAH electrolyte. At the end of electroanalysis ferrocene was added as an internal reference and used to convert to the SCE scale.[14] Argon gas (Ar) was bubbled using a stainless steel needle for 15 minutes to deoxygenate the solution. After purging, a positive pressure of Ar was maintained over the solution. For CO_2 experiments, the solution was sparged for 10 minutes with bone dry grade CO_2 (>99.9% Airgas) to the saturation point in acetonitrile (0.28M).[15] Other gases used were CO (99.99% Matheson Tri-Gas, Inc.), Ar (UHP, 99.999% Praxair) and N_2 (99.998% Praxair).

3.3.3 Photoelectrode Preparation

Photoelectrode substrates were fabricated in the UCSD nano3 microfabrication cleanroom. Three inch p–Si (111) substrates (Wacker Siltronic Corp, San Jose CA, 35–65 ohm–cm, 500 µm thick, boron p–doped 10^{15} cm^{-3}) were used for all experiments. Prior to the metallization on one side, the surface was cleaned ultrasonically for 5 minutes each with methanol, acetone, isopropyl alcohol, and water. The native oxide layer was removed using a HF buffered oxide etch (BOE) as described in chapter 2.6.1. After the etch, 5 nm of titanium and 100 nm of gold was deposited using a Temescal BJD 1800 Ebeam evaporator. A Shipley 1827 positive photoresist layer was added to one side to protect the wafer during the cutting operation on a Disco 3220 automatic dicing saw. The wafer was diced into 10 mm squares and the photoresist removed with Shipley 1165 microposit remover.

3.3.4 Custom Teflon Electrochemical Cell

A custom electrochemical cell was constructed at the UCSD campus research machine shop as shown in Figure 3-2. The cap includes three openings to accommodate the fiber optic light, the reference electrode, and the platinum wire counter electrode. The cell was purged with gases through a septa also containing the counter electrode. One opening in the bottom exposed the p–Si surface to the solution with a fixed area of 0.24 cm^2. The backside was contacted by pressing a polished copper foil to the gold. The

Teflon coated o-ring seals (Marco Rubber, Seabrook, NH), and Teflon cell walls are good for chemical inertness and ensured gas tight operation. This cell design minimizes exposure of the front semiconductor surface of the p–Si photoelectrode to oxygen during the experiments and keeps the backside from contacting the solution. Earlier experiments with epoxy coated electrodes as discussed in chapter 2, interacted with the illuminated Re(bpy) catalyst and were not stable for photoelectrolysis. The new cell design allowed for stable voltammetric measurements, illumination, and the ability to purge the cell with CO_2. The volume required for experiments was between 5–10 mL.

3.3.5 Light Source

A quartz halogen Dolan–Jenner MI–150 with 1/8" flexible fiber optic light guide equipped with an IR filter (cutoff wavelength = 1000 nm) was used as the light source. The broadband illumination intensity was measured as 10 mW/cm^2 with an Ophir 30A–SH–V1 thermopile.

3.3.6 Contact Angle Measurement

Surface contact angle measurements were conducted on a custom–built photographic stand equipped with a micropipette as shown in Figure 3-3. One drop (6.2 µL) of deionized water was placed on the surface and digital photographs were taken using an Olympus C–5050 camera using macro mode. The angle θ between the surface and the droplet edge was measured using Adobe Photoshop. This measurement was used

to determine surface functionalization.[16] In a typical experiment, the p–Si photocathode was hydrogen terminated[17] by placing in an Ar purged 40% NH$_4$F aqueous solution (Aldrich) for 15 minutes, rinsed with Ar purged water, and dried under nitrogen before being exposed to an acetonitrile solution typically containing 0.5 to 2 mM of a redox species or catalyst.

3.3.7 Gas Chromatography

Gas chromatography (GC) was performed on a Hewlett Packard 5890 Series II equipped with a 19095P–HS6 column (Agilent Technologies, length = 30 m, inner diameter = 0.530 mm, 25 μm beads). A thermal conductivity detector (TCD) was used with a helium carrier gas. The injector temperature was 200ºC, the detector 200ºC, and the oven 50ºC for 5 minutes, and then a 25ºC min^{-1} ramp for 4 minutes to bake out residual CO_2 in the column. Authentic samples of CO_2, CO, and Ar were run to determine elution times.

3.4   RESULTS AND DISCUSSION

3.4.1 Electrocatalytic Cyclic Voltammetry of Re(bpy) Under CO$_2$

The cyclic voltammetry (CV) of Re(bpy) on a platinum electrode in DMF shows two reduction waves. Upon addition of CO_2, a 300% increase in current at the second reduction wave at -1.65 vs. SCE appears, as shown in Figure 3-4. This current is characteristic of electrocatalytic behavior and corresponds to CO_2 reduction to CO as

confirmed by GC. The catalyst stability was confirmed with bulk electrolysis runs at –1.8V vs. SCE, that did not show any degradation in current over several hours. The only product observed was CO, confirmed from headspace injections in a gas chromatograph. The reduction mechanism proceeds via an initial one electron reversible reduction of the bipyridine ligand forming $[Re(CO)_3(bpy)Cl]^-$ anion followed by an additional reduction of Re(I) to Re(0).[18,19] The complex is though to first lose chloride, after which CO_2 coordinates with the radical anion to produce CO with one additional electron. The chloride lose is supported by an observed splitting of the first reduction return wave reflecting two distinct species, with and without coordinated chloride. Additional cyclic voltammograms in acetonitrile with supporting electrolyte clearly show this chloride loss by the splitting of the first reversible return oxidation wave of the bipyridine ligand under argon. Varying scan rates (v) over the rage on 10–1000 mV/sec confirm a freely diffusing homogeneous current behavior proportional to $v^{1/2}$.

3.4.2 Electrode Surface Treatment and Contact Angle Measurement

The nature of the semiconductor electrode surface dramatically affects the photoelectrochemical performance. The native oxide on p–Si is prone to defects that hamper the electron transfer properties, specifically by creating recombination centers that enhance the surface recombination velocities.[20] This effectdestroys the needed charge carriers at the surface and leads to lower observed photocurrents and photovoltages. After a hydrogen termination step, the silicon surface can still degrade in only a matter of minutes. During these experiments, exposure of the hydrogen terminated

surface to oxygen was minimized to ensure the best possible photoelectrode voltammetric behavior. To illustrate the change in surface properties, contact angle measurements were taken of water on the electrode surface to determine the hydrophobicity. Figure 3-5 shows the native oxide wetting angle of $\theta = 40°$ corresponding to an approximate thickness of 15 Å.[16] After etching for 15 minutes in argon purged NH_4F, the angle approached $\theta \sim 80\text{–}90°$, corresponding to a purely hydrogen terminated surface. The rapid and selective etching of SiO_2 is an essential pretreatment step for PEC experiments.

3.4.3 Post Surface Treatment and Electrode Characterization

In order to evaluate the surface treatment effect on PEC, cyclic voltammetry was used to probe photoelectrode behavior. Chapter 2 discussed the expected ideal and Fermi-level pinned PEC behavior. From this analysis p–type Si should behave as a photocathode with a fixed photovoltage due to pinning. Model electron acceptors such as tris(2,2'–bipyridyl)ruthenium(II) hexafluorophosphate ($Ru(bpy)_3^{2+}$), and 1,1'–Dimethyl–4,4'–bipyridinium hexafluorophosphate (methyl viologen, MV) were used to characterize the photoelectrodes. These were chosen because they have multiple reversible redox couples with appropriate reduction potentials for PEC. The native p–Si surfaces displayed low photovoltages, and poor photocurrents. This supports sluggish electron transfer at the surface, which resulted in distorted CVs. In contrast, H–terminated p–Si surfaces displayed well–defined CVs with good photocurrent and photovoltage. The photovoltage is in series to the external potentiostat voltage and in the case of p–type photoreduction, an anodic shift is observed. The best performing electrodes showed an anodic shift in the

electron acceptor waves up to 550 mV. These results agree with previous reports,[21] but is only half of the 1.12 eV bandgap of Silicon due to Fermi level pinning.[22] Surface states pin the Fermi level to a given value such that the barrier height is fixed and any additional potential drop occurs at the solution interface (for more details see Chapter 2). After confirmation of good PEC behavior, the electrodes were used with the electrocatalyst.

3.4.4 Electrocatalytic CO_2 reduction on p-Si photocathodes

Photons with energy greater than the band gap will be absorbed by a semiconductor and create an electron in the conduction band, and a hole in the valence band. Due to the induced band bending of p–type semiconductors in contact with a redox species, a surface photovoltage drives electrons towards the surface.[23,24] The electrocatalytic behavior of Re(bpy) shown earlier in Figure 3-4 was repeated in acetonitrile on a glassy carbon surface. The second reduction was no longer reversible as was the case in DMF, but still showed a large current enhancement under CO_2. Controlled potential electrolysis was then performed on illuminated p–Si. Voltages more negative than the peak current for the catalyst had lower Faradaic current efficiencies for CO production. During the electrolysis an uncharacterized surface deposit was observed on the silicon surface. Figure 3-6 shows the cyclic voltammetry for Re(bpy) at a glassy carbon electrode and for an illuminated p–Si electrode. The CO_2 electrocatalytic behavior as shown earlier in Figure 3-4 on platinum in DMF has a similar reduction potential on glassy carbon in acetonitrile, with an onset of –1.65 V vs. SCE. The cyclic

voltammograms of Re(bpy) are used for referencing the shift in potential between glassy carbon and illuminated p–Si. No catalytic current was observed for any scans without CO_2 as shown in Figure 3-6 a–b. In the dark, the p–Si electrode current level of the semiconductor was negligible ($\sim$nA/cm^2). Illumination of the semiconductor in the same solution shows an anodic shift voltammogram of 440 mV with respect to a glassy carbon surface. The first reduction wave remains reversible on p–Si, an indication of good electron transfer from the electrode surface to the solution. The combination of a photovoltage anodic shift and catalytic CO_2 reduction is shown in the cyclic voltammogram 3-4 d. The large current enhancement at –1.26 V on p–Si displays the same 440mV anodic shift, and the catalytic current enhancement is preserved. This lowers the required energy needed for the electroreduction of CO_2 to CO.

3.5 CONCLUSIONS

Reducing the external energy needed for the reduction of CO_2 is accomplished using an illuminated p–Si photocathode to supply current as well as a portion of the voltage. A solution phase Re(bpy) electrocatalyst is used to increase the rate of conversion and selectivity for the reduction of CO_2 to CO. The achieved anodic potential shift required for the electroreduction of CO_2 using photons demonstrates a method for the recycling of CO_2 from a renewable energy source. Although the photovoltage is not sufficient to drive the reduction alone, another semiconductor material with a larger bandgap or a tandem cell device (photocathode and photoanode) could drive the entire

process using only solar energy. Treatment of the silicon surface with NH_4F yields a hydrophobic hydrogen–terminated surface that improves the observed photoelectrochemistry. Additional experiments with other functionalized surfaces, exploration of new electrocatalysts, and testing of additional semiconductor materials are currently being explored.

3.6 ACKNOWLEDGEMENTS

Chapter 2 and 3, in part, are currently being prepared for submission for publication of the material, entitled, "Light Assisted Homogeneous Electrocatalytic Reduction of Carbon Dioxide on p-Type Silicon Evidenced by Cyclic Voltammetry," written by Aaron J. Sathrum and Clifford P. Kubiak. The dissertation author was the primary investigator and author of this material.

Figure 3-1 Incident solar energy strikes the surface of the p–type semiconductor, creating a photocurrent with electrons flowing to the surface. The electrons are transferred to a homogeneous CO_2 electrocatalyst. The photovoltage shifts the electrochemical reaction anodic, supplying energy for the CO_2 transformation.
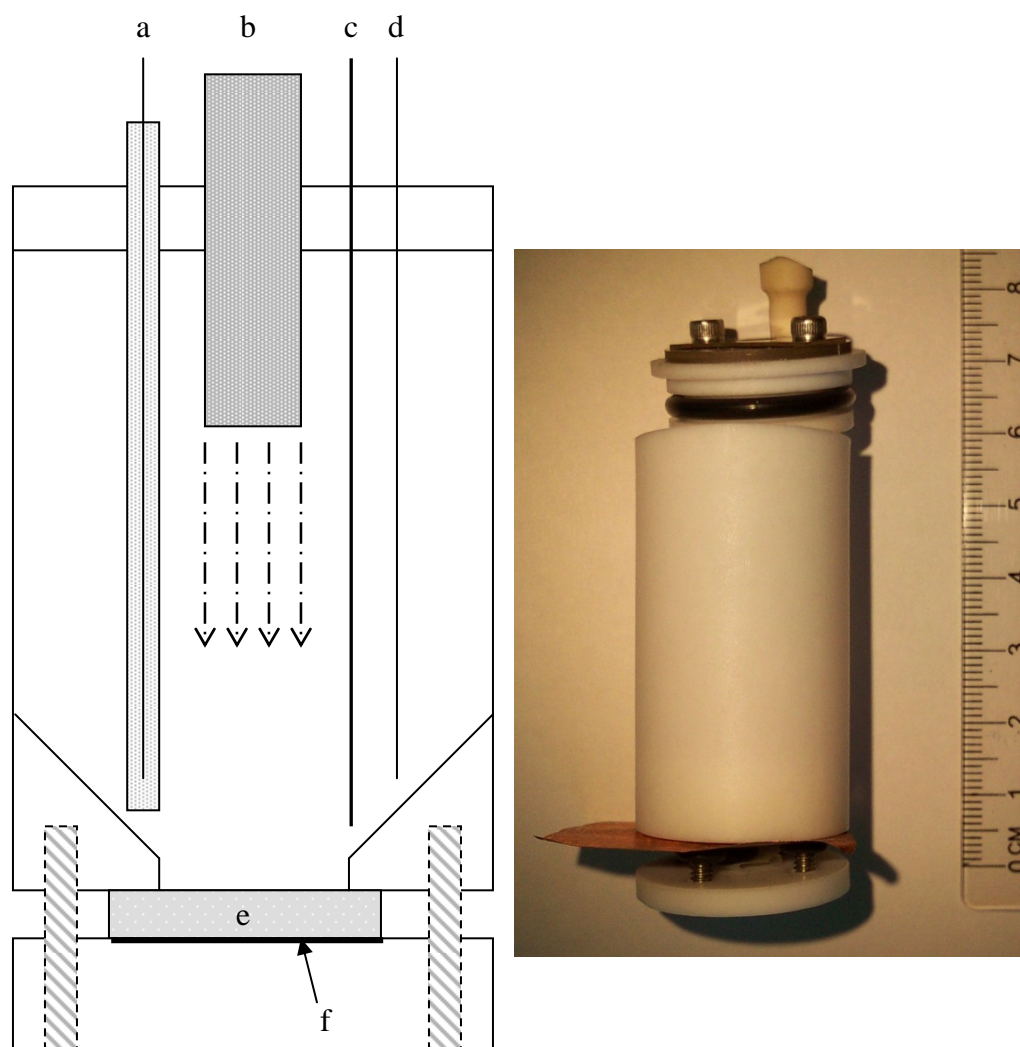
Figure 3-2 Left: schematic of a single compartment air tight Teflon cell for photoelectrochemical measurements. (a) reference electrode, (b) fiber light, (c) platinum wire counter electrode, (d) Ar or CO_2 purge, (e) photoelectrode, (f) backside Ti–Au contact with copper foil. The bottom opening was sealed with a Teflon coated o-ring. Right: photograph of Teflon cell.
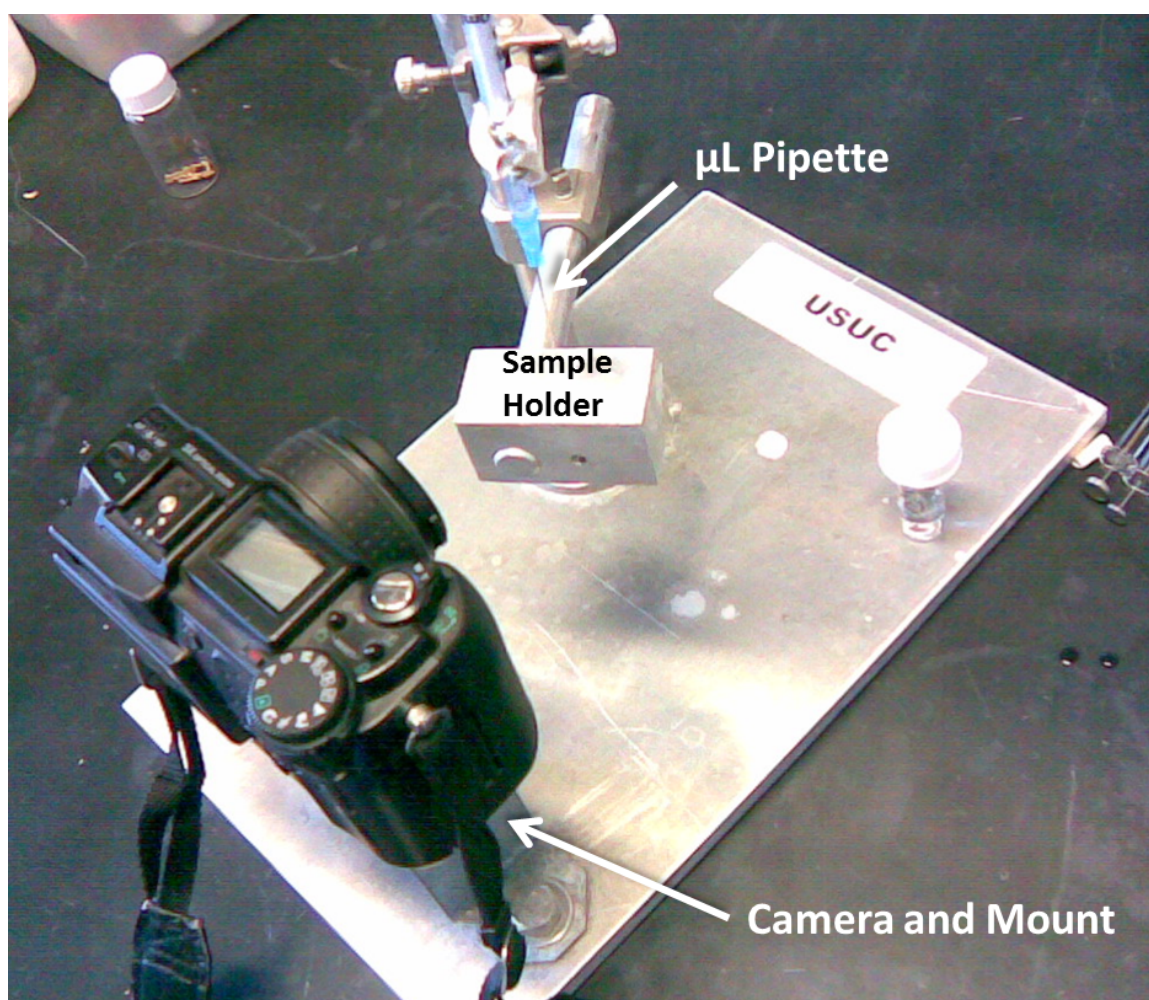
Figure 3-3 Photograph of the contact angle measurement apparatus. The Olympus C–5050 camera is mounted at a fixed distance from the adjustable sample holder. A droplet from the µL pipette is placed on the sample and a digital image captured using macro mode manual focus.
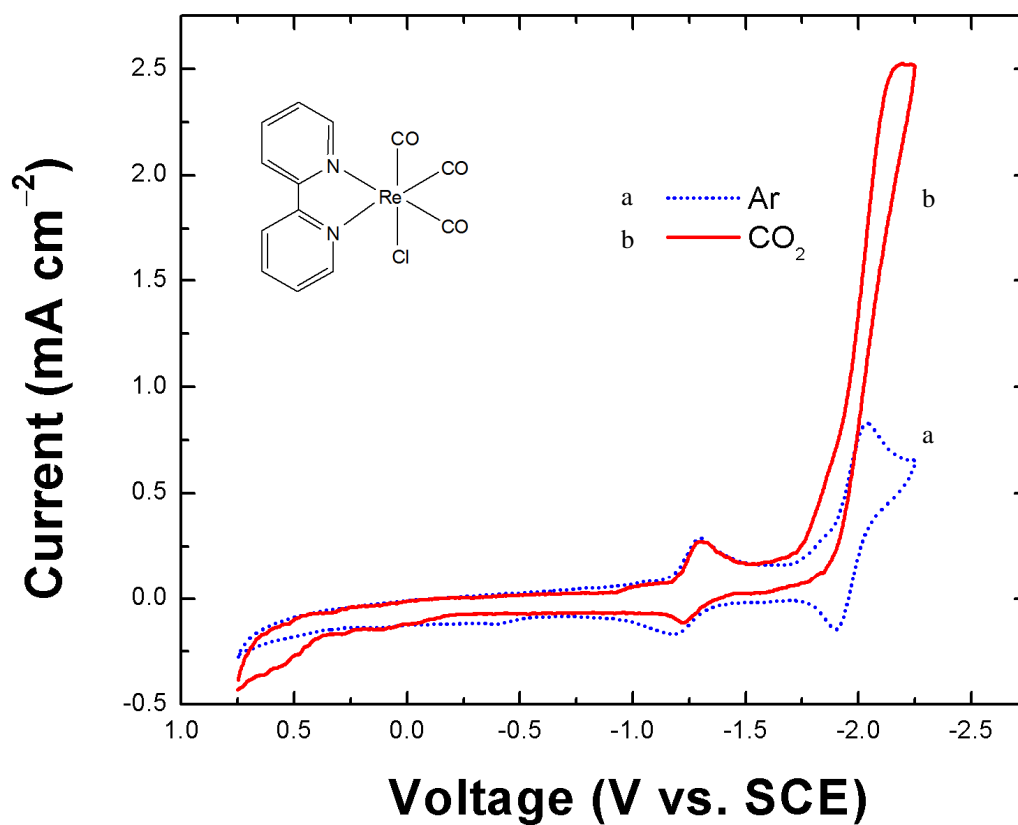
Figure 3-4 Cyclic voltammogram of 0.5mM *fac*–Re(2,2'–bipyridyl)CO$_3$Cl under N$_2$ (dashed line), and CO$_2$ (solid line). Conditions: DMF with 0.1M tetrabutylammonium hexafluorophosphate, scan rate 100 mV/s, platinum working electrode, platinum wire counter electrode.
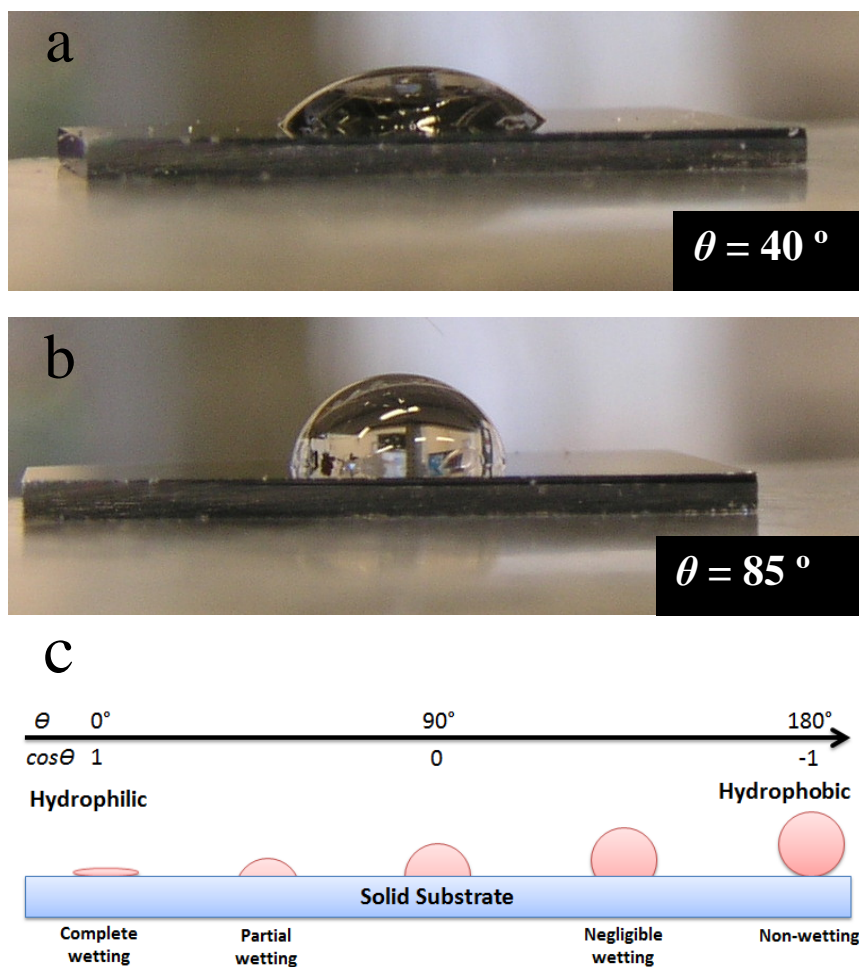
Figure 3-5 Water contact angle measurements showing the p–Si (111) (a) before NH$_4$F etch, and (b) after 15 min etch. Droplet size is 6.2 μL. For scale: the silicon wafer is 500 μm thick. (c) The contact angle measurement scale.
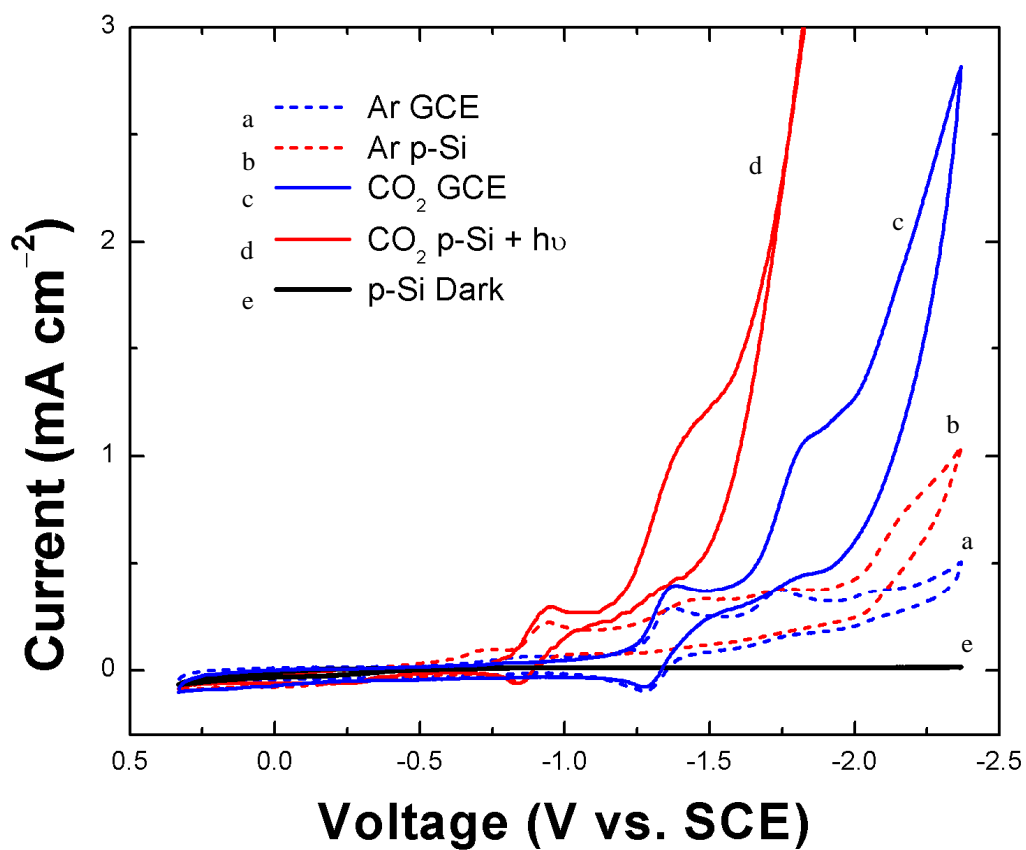
Figure 3-6 Cyclic voltammograms of 0.5mM *fac*–Re(2,2'–bipyridyl)CO$_3$Cl on glassy carbon electrode under Ar (a), and CO$_2$ (c), illuminated p–Si under Ar (b), and CO$_2$ (d), dark p–Si under CO$_2$ (e). Conditions: CH$_3$CN with 0.1M tetrabutylammonium hexafluorophosphate, scan rate 100 mV/s, platinum wire counter electrode.
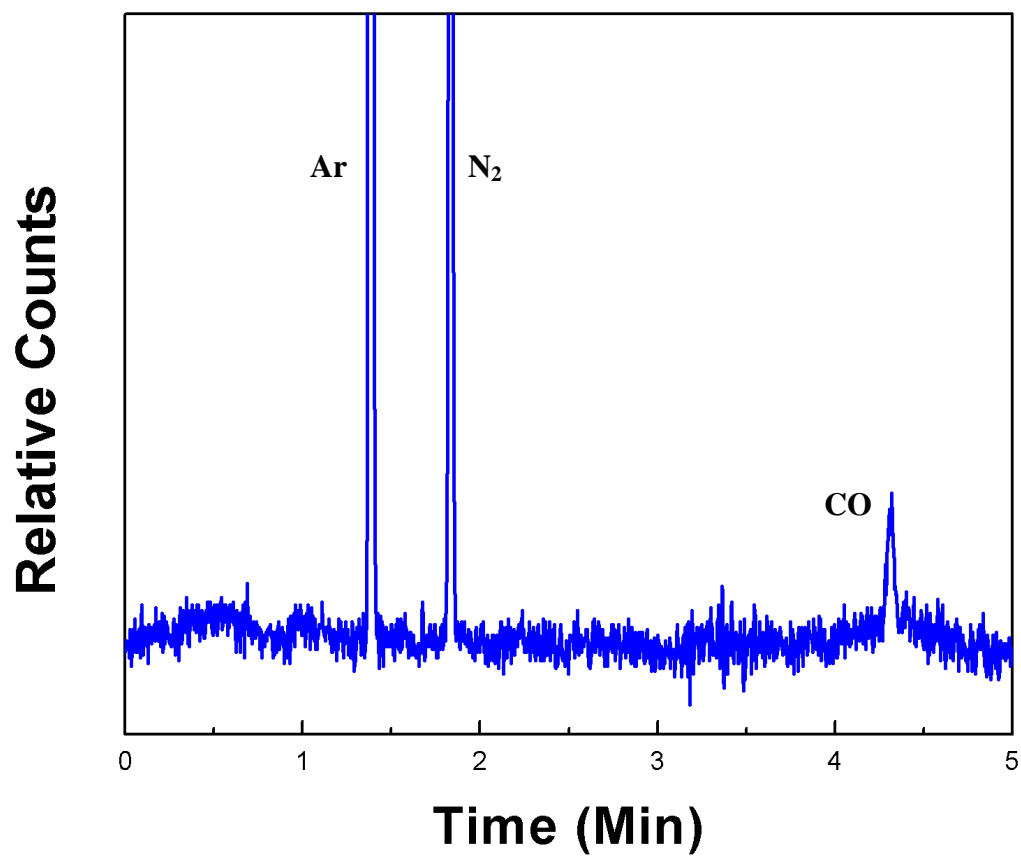
Figure 3-7 Gas chromatograph after a one hour bulk electrolysis on illuminated p-Si with Re(bpy) at –1.35V vs. SCE. CO production appears at a of retention time of 4.3 minutes. Residual argon (1.4 min) and nitrogen (1.8 min) remain from earlier gas purges.

3.7 REFERENCES

(1)   Field, C. B.; Behrenfeld, M. J.; Randerson, J. T.; Falkowski, P. Primary Production of the Biosphere: Integrating Terrestrial and Oceanic Components. *Science* **1998**, *281*, 237-240.

(2)   Arakawa, H.; Aresta, M.; Armor, J. N.; Barteau, M. A.; Beckman, E. J.; Bell, A. T.; Bercaw, J. E.; Creutz, C.; Dinjus, E.; Dixon, D. A.; Domen, K.; DuBois, D. L.; Eckert, J.; Fujita, E.; Gibson, D. H.; Goddard, W. A.; Goodman, D. W.; Keller, J.; Kubas, G. J.; Kung, H. H.; Lyons, J. E.; Manzer, L. E.; Marks, T. J.; Morokuma, K.; Nicholas, K. M.; Periana, R.; Que, L.; Rostrup-Nielson, J.; Sachtler, W. M. H.; Schmidt, L. D.; Sen, A.; Somorjai, G. A.; Stair, P. C.; Stults, B. R.; Tumas, W. Catalysis Research of Relevance to Carbon Management: Progress, Challenges, and Opportunities. *Chem. Rev.* **2001**, *101*, 953-996.

(3)   Klerk, A. d. Fischer-Tropsch Fuels Refinery Design. *Energy Environmen. Sci.* **2011**, *4*, 1177-1205.

(4)   Mikkelsen, M.; Jorgensen, M.; Krebs, F. C. The Teraton Challenge. A Review of Fixation and Transformation of Carbon Dioxide. *Energy Environ. Sci.* **2010**, *3*, 43-81.

(5)   Huynh, M. H. V.; Meyer, T. J. Proton-Coupled Electron Transfer. *Chem. Rev.* **2007**, *107*, 5004-5064.

(6)   Smieja, J.; Sathrum, A.; Kubiak, C.; Benson, E. Electrocatalytic and Homogeneous Approaches to Conversion of CO_2 to Liquid Fuels. *Chem. Soc. Rev.* **2009**, *38*, 89-99.

(7)   Reda, T.; Plugge, C. M.; Abram, N. J.; Hirst, J. Reversible Interconversion of Carbon Dioxide and Formate by an Electroactive Enzyme. *P. Natl. Acad. Sci.* **2008**, *105*, 10654-10658.

(8)   Savéant, J.-M. Molecular Catalysis of Electrochemical Reactions. Mechanistic Aspects. *Chem. Rev.* **2008**, *108*, 2348-2378.

(9)   Hawecker, J.; Lehn, J.-M.; Ziessel, R. Electrocatalytic Reduction of Carbon Dioxide Mediated by Re(bipy)(CO)$_3$Cl (bipy = 2,2'–bipyridine). *J. Chem. Soc. Chem. Comm.* **1984**, 328.

(10)   Hawecker, J.; Lehn, J.-M.; Ziessel, R. Photochemical and Electrochemical Reduction of Carbon Dioxide to Carbon Monoxide Mediated by (2,2'-

Bipyridine)tricarbonylchlororhenium(I) and Related Complexes as Homogeneous Catalysts. *Helv. Chim. Acta* **1986**, *69*, 1990-2012.

(11) Grätzel, M. Photoelectrochemical Cells. *Nature* **2001**, *414*, 338-344.

(12) Wrighton, M.; Morse, D. L. Nature of the Lowest Excited State in Tricarbonylchloro-1,10-phenanthrolinerhenium(I) and Related Complexes. *J. Amer. Chem. Soc.* **1974**, *96*, 998-1003.

(13) Cattaneo, M.; Fagalde, F.; Katz, N. E. Proton-Induced Luminescence of Mono- and Dinuclear Rhenium(I) Tricarbonyl Complexes Containing 4-Pyridinealdazine. *Inorg. Chem.* **2006**, *45*, 6884-6891.

(14) Connelly, N. G.; Geiger, W. E. Chemical Redox Agents for Organometallic Chemistry. *Chem. Rev.* **1996**, *96*, 877-910.

(15) Scovazzo, P.; Poshusta, J.; Dubois, D.; Koval, C.; Noble, R. Electrochemical Separation and Concentration of <1% Carbon Dioxide from Nitrogen. *J. Electrochem. Soc.* **2003**, *150*, D91-D98.

(16) Williams, R.; Goodman, A. M. Wetting of Thin Layers of SiO_2 by Water. *Appl. Phys. Lett.* **1974**, *25*, 531-532.

(17) Wade, C. P.; Chidsey, C. E. D. Etch−Pit Initiation by Dissolved Oxygen on Terraces of H−Si(111). *Appl. Phys. Lett.* **1997**, *71*, 1679-1681.

(18) Scheiring, T.; Klein, A.; Kaim, W. EPR Study of Paramagnetic Rhenium(I) Complexes (bpy(center dot−))$Re(CO)_3$X Relevant to the Mechanism of Electrocatalytic CO_2 Reduction. *J. Chem. Soc. Perk. Trans. 2* **1997**, 2569-2571.

(19) Johnson, F. P. A.; George, M. W.; Hartl, F.; Turner, J. J. Electrocatalytic Reduction of CO_2 Using the Complexes [Re(bpy)$(CO)_3$L](n) (n=+1, L=P(OEt)$_3$, CH_3CN; n=0, L=Cl−, Otf(−); bpy=2,2'−bipyridine; Otf(−)=CF_3SO_3) as Catalyst Precursors: Infrared Spectroelectrochemical Investigation. *Organomet.* **1996**, *15*, 3374-3387.

(20) Webb, L. J.; Lewis, N. S. Comparison of the Electrical Properties and Chemical Stability of Crystalline Silicon(111) Surfaces Alkylated Using Grignard Reagents or Olefins with Lewis Acid Catalysts. *J. Phys. Chem. B* **2003**, *107*, 5404-5412.

(21) Bocarsly, A. B.; Bookbinder, D. C.; Dominey, R. N.; Lewis, N. S.; Wrighton, M. S. Photoreduction at Illuminated p−Type Semiconducting Silicon

Photoelectrodes. Evidence for Fermi Level Pinning. *J. Am. Chem. Soc.* **1980**, *102*, 3683-3688.

(22)   Bard, A. J.; Bocarsly, A. B.; Fan, F. R. F.; Walton, E. G.; Wrighton, M. S. The Concept of Fermi Level Pnning at Semiconductor/Liquid Junctions. Consequences for Energy Conversion Efficiency and Selection of Useful Solution Redox Couples in Solar Devices. *J. Amer. Chem. Soc.* **1980**, *102*, 3671-3677.

(23)   Koval, C. A.; Howard, J. N. Electron Transfer at Semiconductor Electrode– Liquid Electrolyte Interfaces. *Chem. Rev.* **1992**, *92*, 411-433.

(24)   Nozik, A. J.; Memming, R. Physical Chemistry of Semiconductor-Liquid Interfaces. *J. Phys. Chem.* **1996**, *100*, 13061-13078.

CHAPTER 4

ELECTROLYSIS OF CO$_2$ TO CO BY DIRECTLY COUPLING A PHOTOVOLTAIC SOLAR CELL WITH A HOMOGENEOUS ELECTROCATALYST

4.1 ABSTRACT

The ability to use renewable electricity from photovoltaic cells to convert CO_2 into more useful products such as CO was demonstrated. The design and theoretical voltage requirements show a minimum practical voltage of 3.4 V even though the thermodynamic minimum is only 1.33 V. The balancing of a non-linear power supply to a non-linear load reveals a self–stabilizing nature. A fully integrated system for a directly coupled solar photovoltaic driven CO_2 electrolyzer was built and characterized. The current–voltage (I–V) behavior of the source and the load shows a resulting intersection termed the operating point. The voltage at this operating point (V_{op}) greatly determines the efficiency of the operation of the solar cell and thus the total system efficiency. An overall solar conversion efficiency (η_{TOT}) of 2.1% was achieved by using an electrocatalyst based on Re(4,4'-di-*tert*-butyl-2,2'-bipyridine)(CO)$_3$Cl (Re-tBu). This efficiency assumes oxygen generation at the counter electrode and further experiments are ongoing to investigate the exact quantity and composition of the anode product. Theoretical calculations predict an upper efficiency limit of 21% for a single junction solar cell coupled to an electrolyzer. This stand-alone performance shows great promise and demonstrates the need for further development of more efficient CO_2 electrocatalysts.

4.2 INTRODUCTION

The solar driven conversion of carbon dioxide into a chemical feedstock for fuel production would allow for a more sustainable energy cycle. At the present time it is not

clear whether artificial photosynthesis or biofuels derived from natural photosynthesis will ultimately be used to provide and store renewable energy. An electrolysis system for "carbon dioxide splitting" requires electrocatalysts for selective production of carbon based products at a low overpotential. Electricity from intermittent renewable resources can supply the energy necessary for the electrolyzer. This stores the renewable energy in chemical bonds and can be further upgraded with Fischer–Tropsch processes for highly dense and transportable liquid fuels.

The chemical transformation of a material by an applied voltage and current is at the heart of electrochemistry. Electrochemical reactor engineering encompasses a diverse set of fields including but not limited to: chemistry, physics, engineering, and material science. Current industrial examples include the Hall-Hérout process for aluminum production ($4.1x10^6$ tons year^{-1}) and the chloralkali process for producing chlorine and sodium hydroxide ($11.1x10^6$ tons year^{-1}).[1-3] The cell design and operating can be very process–specific, however a description of the minimum components can be generalized.[4] Figure 4-1 shows a schematic of a generic two–compartment cell with the individual voltage components needed for the minimum applied voltage ($V_{applied}$). A cathode supplies n electrons for a reduction reaction, which is physically separated from the anode where n electrons are withdrawn. In between the two electrodes is an electrolyte that allows ionic conduction and a separator that keeps the anode and cathode products from mixing, but still allows ions to flow. Each component adds additional required voltage. Each electrode reaction requires additional voltage above the thermodynamic minimum (V_c, V_a) called the overpotential (η_c, η_a), which can be lowered by a

heterogeneous or homogeneous catalyst. An electrolyzer also has further ohmic loss due to the resistance of the solution V_{ohm} and junction loss V_{junc}. The ohmic loss is directly proportional to the current flowing in the cell, therefore it is important to minimize the resistance. This can be accomplished by increasing electrolyte concentration, increasing temperature, improving separator ion conductivity, decreasing electrode spacing, and keeping the current to a low value. The circuit for electrolysis is completed by an external circuit using a power supply connected to the cathode (–) and anode (+). The general components of an electrolyzer provide a basis for the design. No such design currently exists for homogeneous CO_2 electroreduction. A simple approach towards accomplishing this will be described in detail in this chapter with the additional of using a solar photovoltaic as the power supply.

4.3   EXPERIMENTAL

4.3.1 Materials

All chemicals used were analytical grade or higher. The electrolyte, tetra-*n*-butylammonium hexafluorophosphate, $[(n-C_4H_9)_4N]PF_6$ (TBAH) (Sigma-Aldrich 98%), was recrystallized in ethanol and dried under vacuum for 24 hours at 100°C. Acetonitrile was degassed and dried on a custom dry solvent system. Re-tBu was prepared via literature methods.[5] Purity of synthesized compounds was confirmed via NMR, IR, and elemental analysis techniques. A variety of solar cells were purchased from Sundance

Solar (Warner, NH) and Futurlec (New York, NY) and fully characterized with a solar simulator light source.

4.3.2 Solar Simulator

The solar simulator was a custom 450 W xenon lamp equipped with an air mass 1.5 global (AM1.5G) filter (Newport 81094) used to illuminate the solar cells. The intensity was calibrated using a calibrated silicon photodiode (OSI Optoelectronics) on an optical rail. Light and dark I–V curves were collected using a custom LabVIEW (National Instruments) data capture program.

4.3.3 Gas Chromatography

Gas chromatographs were performed on an Agilent Technologies 7890A equipped with a 19095P-MS6 molesieve column (Agilent Technologies, length = 30 m, inner diameter = 0.53 mm, 25 μm beads). A thermal conductivity detector (TCD) was used with a helium carrier gas. The injector temperature was 200°C, the detector 250°C, and the oven 50°C for 6 minutes, and then ramped to 200°C for 6.4 minutes while back flushing the system. A multipoint calibration curve was constructed via dilution of CO (Matheson, UHP, 99.9%), in argon (Airgas, UHP, 99.999%). A fully deaerated 1 mL Hamilton gas-tight syringe was used to extract headspace samples via a septum. A sample of the electrolyzer headspace (75 mL) was taken immediately after CO_2 purging to confirm no initial CO present in the system. During electrolysis 1 mL aliquots were

taken at regular intervals (10–15 minutes) and analyzed. No corrections were made for dissolved CO in solution due to the low reported solubility (0.005–0.008 M) in acetonitrile.[6,7]

4.3.4 Electrochemical Methods

All electrochemical experiments were performed in acetonitrile with 0.1M TBAH as supporting electrolyte. Solutions were flushed with argon, or CO_2 (Airgas, Bone Dry, 99.9%) for a minimum of 10 minutes. The concentration of dissolved CO_2 at saturation has been reported as 0.26M in acetonitrile.[8,9] The solution volume and therefore the redox concentration were maintained by incorporating an inline bubbler containing solvent to prevent evaporation. Re-tBu concentrations ranged from 1–5 mM. The solutions were not stirred during data collection. Corrections for iR loss and concentration overpotentials were not performed.

4.3.5 Cyclic Voltammetry of Re-tBu

A Bioanalytical Systems Inc. (BASi), model CV-50W voltammetric analyzer was used for measuring cyclic voltammograms via a three–electrode setup without *i*R compensation. A one–compartment cell was used incorporating a glassy carbon working electrode (BASi, 3 mm diameter), a platinum wire counter electrode, and a Ag/AgCl reference electrode with ferrocene ($Fc^{+/0}$) added as an internal reference and adjusted to SCE.[10,11] Working electrodes were polished with 3 μm, 1 μm, and 0.05 μm slurries

(BASi), sonicated, and rinsed with reagent grade water and methanol prior to use. Figure 4-2 shows the cyclic voltammetry of Re-tBu. Scans under CO_2 in the same voltage range without catalyst did not show any current enhancement or CO production.

4.3.6 Bulk Electrolysis

Controlled potential electrolysis was performed using a Pine Instruments Inc., model AFCBP1 bipotentiostat for construction of electrolyzer characteristic curves. This consisted of a two-electrode setup by shorting the counter and reference electrodes. A custom gas tight single compartment cell shown in Figure 4-3 with a carbon cathode (~5 cm^2) and platinum mesh anode (~5 cm^2) was used. For electrolysis runs using a solar cell, a stopwatch was used to measure the time elapsed. A current meter and separate voltage meter were used to monitor output from the solar cell.

4.4   COMPARISON TO NATURAL PHOTOSYNTHESIS

Capturing energy from the sun to facilitate the renewable conversion of CO_2 into useful chemicals creates a more sustainable carbon cycle. The current carbon cycle is being driven to increasing atmospheric concentrations on a global scale and new approaches to reducing CO_2 levels are needed.[12,13] CO_2 conversion is successfully accomplished by plants via photosynthesis on a global scale of more than 100 billion tons per year.[14] CO_2 is inherently inexpensive, stable, and abundant. Yet less than 2% of anthropogenic CO_2 is utilized industrially (mostly for urea synthesis) due to the large

energetic barriers involved.[15] Major targets for conversion include carbon monoxide, methanol, formaldehyde and formic acid.[16-18] CO can be combined with H_2 (syngas) and readily integrated into the existing chemical industry for further upgrading to liquid fuels via Fischer–Tropsch technology.[19] A sampling of end products that can be derived from syngas is shown in Figure 4-4.[20] Some of the Homogeneous electrocatalysis presents a unique opportunity to convert and store electrical energy in CO_2 derived products at low input energy.[21] Artificial systems utilizing transition metal complexes often exhibit large overpotentials and slow kinetics.[22] However a recently reported catalyst,[5] inspired by a rhenium bipyridine reported by Lehn,[23,24] has given homogeneous based systems considerable merit.

The artificial photosynthetic reaction that converts CO_2 to CO is an important goal in energy and climate research. At the present time it is not clear whether artificial photosynthesis[25] or biofuels derived from natural photosynthesis[26] will ultimately be used to provide and store renewable energy. Plants convert solar energy, albeit at low insolations of 100–200 W m^{-2} due to saturation of water oxidation, into biomass with a photosynthetic efficiency of 0.2-2%, e.g. switch grass (0.2-0.6%), maize (0.8%), and sugar cane (2.24%).[27] Therefore an integrated artificial device with an efficiency better than the natural analog would be invaluable towards correcting the global carbon cycle. A goal of sunlight to chemical energy with an efficiency of 10% for an artificial system is reasonable and theoretically attainable.[28] A complete artificial system for the renewable conversion of CO_2 into an upgraded carbon feedstock via homogeneous electrocatalysis provides a tangible benchmark of the present capability.

4.5 ELECTROLYZER CONSTRUCTION AND TESTING

To demonstrate this device, a homogeneous CO_2 electrolyzer was built and directly coupled it to a photovoltaic (PV) cell as shown in Figure 4-3. A carbon cathode was separated from a platinum mesh anode by a polypropylene mesh. A custom Teflon cap fitted with o–rings created a gas tight seal. A glass tube equipped with a septa allowed for electrode wires and headspace sampling. By directly connecting the PV to the electrolyzer, no voltage converters, charge controllers, batteries, or maximum power point trackers (MPPT) are used. The Re(4,4'-di-*tert*-butyl-2,2'-bipyridine)(CO)$_3$Cl (Re-tBu) electrocatalyst chosen was previously reported by Smieja and Kubiak,[5] and shows selectivity towards CO production, high turnover number (TON), and high turnover frequency (TOF). Initial studies on a variety of cathode material candidates revealed that glassy carbon supports the largest current density of 5 mA cm^{-2} at –1.9 V vs. SCE (1 mM Re-tBu, 0.25M CO_2).[8] A thin 0.033 cm polypropylene mesh was used to separate the carbon cathode rod from the platinum mesh anode to minimize solution iR losses while maintaining physical separation of the electrodes. Since the electrolysis cell was a single compartment, the reaction(s) taking place at the counter electrode did not decrease the activity of the Re based electrocatalyst or get re-oxidized at the anode. This wass supported by observing no loss in current density over the course of each experiment (1–2 hours). The catalyst selectively produces CO, which forms bubbles that rapidly rise to the solution surface, thus decreasing the amount of possible contact with the anode.

Control experiments with catalyst but without CO_2, and without catalyst and with CO_2 did not produce any CO under the same applied voltage. This effectively shows that homogeneous electrocatalyst based systems can be very selective, stable, and kinetically fast such that they can be readily integrated into an electrolyzer.

4.6   RESULTS AND DISCUSSION

4.6.1 Photovoltaic Source to Load Power Matching

The electrolyzer current–voltage response (load curve) reflects the specific electrolyzer performance. In order to correctly match the PV power, the load curve must be measured. By varying the applied voltage, a characteristic load curve was constructed as shown in Figure 4-5A. The voltage is held for several minutes at each point to measure the diffusion limited catalytic current as shown in Figure 4-5B. The load curve is essential in understanding how to match a non-linear load (electrolyzer) to a non-linear power source (PV cell). This captures all the power, current, and voltage demands concisely. The features of this curve reflect the diffusion limited current for the first and second reductions of the electrocatalyst (see Figure 4-2) in a saturated solution of CO_2 and the edge of the acetonitrile electrochemical window.

4.6.2 Theoretical Voltage Requirement

The above results are in good agreement with the calculated voltage requirements. Figure 4-6 shows a line graph with the respective cathodic and anodic reactions taking

into account the additional voltage required for each. To summarize the thermodynamics, the standard redox voltage per electron required for CO_2 splitting is 1.33 V, which is only slightly more than 1.23 V for H_2O splitting. However, the tremendous amount of research on proton reduction and water oxidation has yielded a combined overpotential as low as 200 mV, whereas for the CO_2 reduction half reaction of this system, the overpotential alone is 1100 mV.[5] If water oxidation is the reaction occurring at the anode and the protons used as oxygen acceptors for the cathodic reaction, then the total required voltage increases to 3.4 V. Scheme 4-1 shows the respective reactions at pH 7. This simple analysis does not take into account any geometric or membrane separator iR losses that would increase the practical operating voltage.

Individual PV cells of 4 V and 6 V were selected for the custom built electrolyzer. With an understanding of the electrolyzer load, solar cells with less than 100 mW total power output under one sun (1000 W m^{-2}) are coupled directly to the setup as shown in Figure 4-3. It is important that the supply power is less than the demand so that the current produced by the PV cells is be completely utilized by the electrolyzer. Optimization strategies have been previously shown for hydrogen generation from PV and these can be readily applied to this new system.[29-31] For example, the PV power supply can be adjusted by increasing the number of cells in series or parallel. The electrolyzer characteristic (load) can be changed by adjusting the electrode surface area, catalyst concentration, temperature, and pressure. The load can also be increased by stacking additional cells similar to PEM electrolyzers.[31,32] Finally, the I–V of a solar cell can be completely decoupled from a given load by using complex electronic circuitry via

direct current (DC) voltage conversion and power point tracking algorithms.[33] While these optimization strategies increase the overall device efficiency, the goal of this work was to demonstrate a simple and straightforward approach for solar powered CO_2 electrolysis.

4.6.3 Operating Point and Self–Stabilization Behavior

Each solar cell was fully characterized under an AM 1.5 G solar simulator. The fill factor (FF), open circuit voltage (V_{OC}), short circuit current (I_{SC}), and the maximum power point (P_{max}) are determined from the measured I–V curves.[34] Then the I–V curve was superimposed onto the electrolyzer characteristic as shown in Figure 4-7A and 4-7B. The two curves intersect defining a direct–coupled operating point. For the 4 V cell this was at 4.1 V and 8.3 mA of current and for the 6V cell this was at 4.3 V and 12.8 mA of current. Interestingly the supply and load curves are opposite in nature and thus form a built in self–stabilization control system. If the supply voltage is too high, then the PV current would decrease, but the load demands a high current at high voltages, forcing the voltage across both to float lower until it reaches the operating point. Conversely if the supply voltage is too low, then the PV current would increase, but the load demands a lower current at low voltages, so the voltage across both will float higher until it reaches the operating point. The location of this operating point is critical for evaluating the efficient transfer of power from the PV cell, since the power-to-voltage (P–V) curve is non-linear and shows a maximum power point (MPP).

A perfectly matched system has the MPP voltage exactly at the operating point voltage. Hypothetically, if the PV power is kept constant while independently controlling the voltage and current of the PV cell, then a constant power line can be used for power matching. For comparison, the constant power at the MPP was added to Figure 4-7A and 4-7B. This new line intersects with the electrolyzer characteristic at the optimal operation point for the given PV cell power. The I–V of a PV cell depends on the specific geometry of the constructed cell, the semiconductor material, and the illumination. This results in a finite selection of PV cells that are commercially available. This limits the direct–coupled power matching approach. However, by increasing the system size, a lowest common multiple makes the power matching easier because of the division of voltage mismatch over multiple electrolyzers and multiple solar arrays.

4.6.4 Evaluation of Power Matching

A comparison between the operating point and the optimal point provides a direct measure of power matching. In order to completely and directly transfer all of the power from a PV cell to an electrolyzer, the power must be appropriately matched. Another way to visualize power matching is by taking the same data from the I–V plots and converting to P–V plots. Multiplying the current by the voltage in the electrolyzer characteristic yields the load power characteristic shown in Figure 4-7C and 4-7D for the 4 V and 6 V cells respectively. The intersection between the power characteristic and P–V curve was the same operating point as shown previously in Figure 4-7A and 4-7B. Also included as a secondary y-axis is the measured solar efficiency η_{PV} of the PV cell to show the non-

linear η_{PV} behavior of a solar cell that depends on the operating voltage. These graphs show that the peak η_{PV} was in close proximity to the operating point for both cells. For the 4 V cell the V_{MPP} was at 3.5 V and 20.2 mA of current and for the 6 V cell at 5.5 V and 12.6 mA of current. Strictly looking at the V_{MPP} for the 4V case we are at a lower voltage, while the 6 V case at a higher voltage than V_{op}. However the slope of the P–V curve was not symmetrical. The lower voltage side (left) of V_{MPP} has a linear response to increasing V_{op}, while the higher voltage (right) has an exponential drop off due to biasing the diode. This emphasizes that the η_{PV} of directly–coupled systems will depend strongly on the voltage mismatch:

$$\Delta V_{mismatch} = V_{MPP} - V_{op} \qquad \textbf{(4-1)}$$

where V_{op} is the operating point voltage and V_{MPP} is the maximum power point voltage. The sign of equation 4-1 reflects the location: negative is lower and positive is higher than V_{op}. While the 6 V cell possesses a greater voltage mismatch of +1.25 V, it was in the linear region and does not suffer as much η_{PV} loss. To contrast this, the 4 V cell has less mismatch of –0.6 V, but was past V_{MPP} in the exponential drop off region and suffers a greater overall η_{PV} loss. The directly coupled electrolyzer was matched as closely as possible within the measured conditions. If this approach is taken to a larger scale, the power matching becomes easier because one can find the least common multiple grouping to match the supply and load.

4.6.5 Directly–Coupled PV Bulk Electrolysis

With an understanding of power matching, controlled electrolysis experiments are run using several solar cells. A detailed photograph of the experimental setup is shown in Figure 4-8. The total efficiency was computed using equation 4-2:

$$\eta_{TOT} = (\eta_{PV})\ (\Phi_{CO})\ \left(\frac{V_{Therm}}{V_{op}}\right) \qquad \textbf{(4-2)}$$

where η_{PV} is the the PV cell efficiency in %, Φ_{CO} the Faradaic current efficiency for CO production in %, V_{op} the operating voltage, and the V_{Therm} is the thermoneutral voltage equal to 1.47 V.[35] The thermoneutral voltage refers to the isothermal operation (only electrical energy input) for CO_2 conversion to CO and O_2. For the 6 V cell an average voltage of 4.3 V and an average current of 12.7 mA are measured during a 67 minute experiment. The current and voltage levels are shown in Figure 4-9A. Since the solution was not stirred there was an initial drop in current and a corresponding increase in voltage until the diffusion-limited steady state was reached. This observation reinforces the self-stabilization control behavior of the direct-coupled system mentioned earlier. Figure 4-9B shows the amount of CO produced versus the coulombs consumed. The average Φ_{CO} was 72%, the average voltage efficiency was 34%, and the average η_{PV} was 6.9%. A small amount of hydrogen (less than 1% of the total current) was also detected by GC. Note that the measured maximum efficiency of the 6V solar cell was only 8.7%. Figure 4-10 shows the time evolution of the CO trace measured in the GC from point taken every 10–15 minutes during the electrolysis. The average total efficiency η_{TOT}, for the 6 V cell was 1.7% with a maximum of 2.1%. In a separate run for the 4 V cell, the

average Faradaic efficiency was 79%, the average voltage efficiency was 36%, and the average solar efficiency was 6.1%. Note, the measured maximum efficiency of the 4 V solar cell was 10%. The average total efficiency for the 4 V cell was 1.7% with a maximum of 2.1%. These results are summarized in Table 4-1. It must be emphasized that these experiments are performed at room temperature, in one atmosphere of CO_2, without any electronic control systems. Interestingly from these results, the measured total efficiency was similar for the 4 V and 6 V case, even though the mismatch from the maximum operating point (as discussed earlier) is quite different. This supports the mismatch non-linearity of η_{PV} and the electrolyzer as discussed earlier. A simple demonstration of solar PV driven bulk electrolysis demonstrates a sustainable method for the conversion of CO_2 to CO.

4.6.6 Maximum Theoretical PV–Electrolyzer Efficiency

It is important to ask how efficient this conversion method could become and what are the barriers to improvements. Taking a look at equation 4-2 one can see that the photovoltaic solar cell efficiency plays a dominant factor. Under one sun irradiance, the limit for a single junction solar cell is 30%.[36] This sets the upper efficiency for any direct single junction solar-coupled device. The Faradaic current efficiency reflects the selectivity of the catalyst within the given electrochemical conditions as well as the collection of the product. The upper limit is 100% and many CO_2 electrocatalytic systems have reported current efficiency near unity.[5,23,37] Finally the voltage efficiency is driven by the ratio of the thermoneutral voltage to the applied voltage. The applied voltage

consists of the concentration overpotentials, ohmic losses due to solution and separator, and the electrocatalyst overpotential at the cathode and the anode. A practical goal of 0.3 volts of overpotential[38] per electrode would set a maximum voltage efficiency of 71%. Combining these limits yields a theoretical maximum efficiency of 21%. For comparison, current reports for peak PV powered H_2 generation range from 7–16%.[30,39,40] This highlights a need for further research to develop lower potential CO_2 homogeneous reduction catalysts while maintaining high kinetic rates and selectivity.

4.7 CONCLUSION

The ability to produce more sustainable carbon feedstocks is an important goal in energy and climate research. This work demonstrates a directly coupled homogeneous CO_2 electrolyzer that can use renewable energy and electrocatalysis to produce CO. The merits for characterizing an electrolyzer load and the power matching have been elucidated. The demonstrated PV electrolyzer approach is competitive with natural systems and theoretically could approach an overall conversion efficiency of 21%. Photovoltaic technology was chosen because it is modular in size, available commercially, and can benefit from the storage of harnessed energy into chemical products. In principle any renewable electrical source or even excess grid capacity could be redirected to electrolyzers for driving CO_2 conversion. This work shows that the recycling of CO_2 into chemical feedstocks could be a viable part of the solution for storing electrical energy and help mitigate rising atmospheric CO_2 levels. An overall

solar fuel conversion efficiency up to 2.1% was achieved by using an electrocatalyst based on a rhenium complex. This efficiency assumes simultaneous oxygen generation and further experiments are ongoing to investigate the exact quantity and composition of the anode product. The efficiency can be increased using higher efficiency solar cells, better power matching, and the use of electrocatalysts with lower overpotentials. Further development of more efficient CO_2 electrocatalysts from more earth abundant materials that are water soluble and conversion techniques are ongoing in our laboratory.

4.8   ACKNOWLEDGEMENTS

Chapter 4, in part, is currently being prepared for submission for publication of the material, entitled, "Artificial Photosynthesis of CO from CO_2: How Efficient is it?" written by Aaron J. Sathrum and Clifford P. Kubiak. The dissertation author was the primary investigator and author of this material.

$$V_{applied} = (V_a + \eta_a) - (V_c + \eta_c) + V_{ohm} + V_{junc}$$

Figure 4-1 The necessary components in a homogenous CO_2 electrolyzer. A voltage sources supplies the driving force, reduction occurs at the cathode, oxidation at the anode, the separator can be an ionic conductor that selectively keeps products and can act as a solid electrolyte, the solution (and electrolyte). The total applied voltage necessary is the sum of the thermodynamic potentials, overpotentials, and the geometric resistive losses.
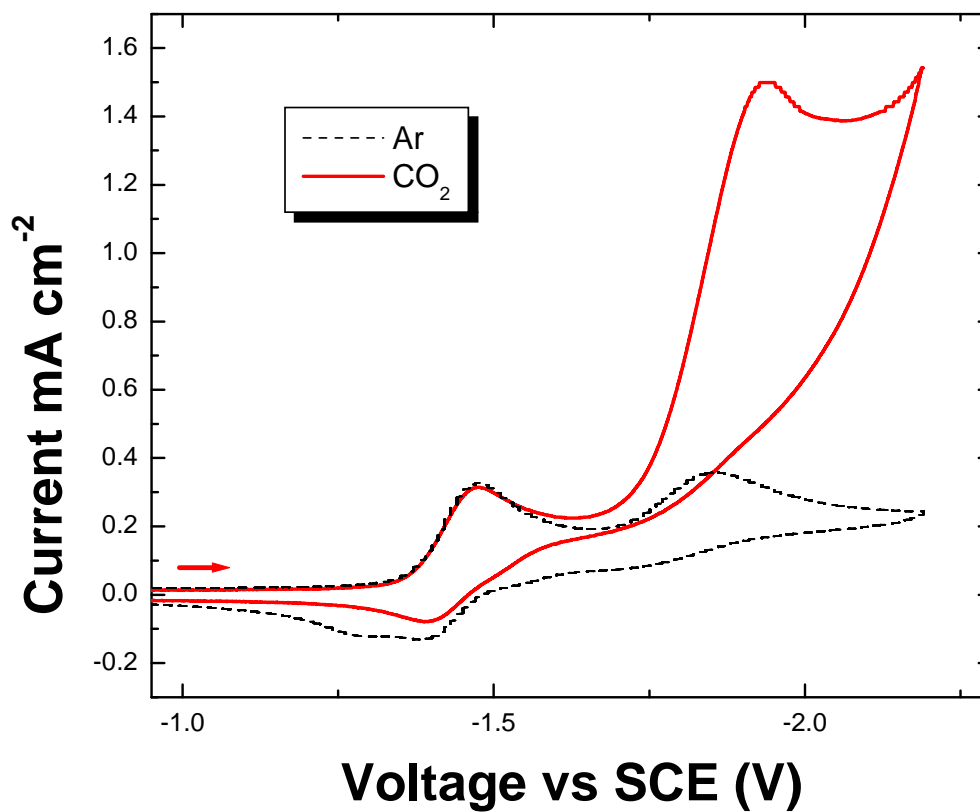
Figure 4-2 Cyclic voltammogram of 1mM Re-tBu complex in acetonitrile containing 0.1M TBAH electrolyte on a 3mm diameter glassy carbon working electrode with a Pt wire auxiliary electrode. The scan rate is 100mV s^{-1} with ferrocene used as an internal standard. Scans are performed under Ar (black dashed line) and CO_2 (red solid line).
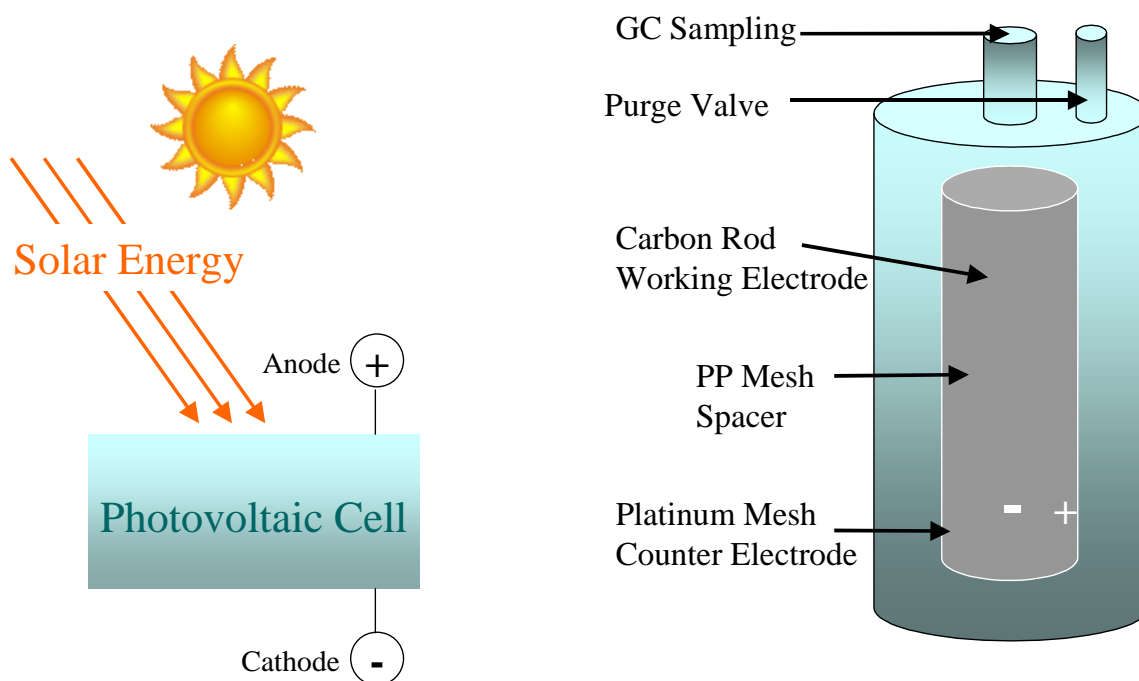
Figure 4-3 Electrolyzer characterization and direct PV coupled electrolysis is conducted in a custom gas tight glass cell with a Teflon cap. A carbon cathode (–) and platinum mesh anode (+) are separated by a thin polypropylene (PP) mesh. The single compartment cell is filled with 50 mL of CH_3CN containing 0.1 M tetra-*n*-butylammonium hexafluorophosphate electrolyte, and 1 mM Re-tBu electrocatalyst.
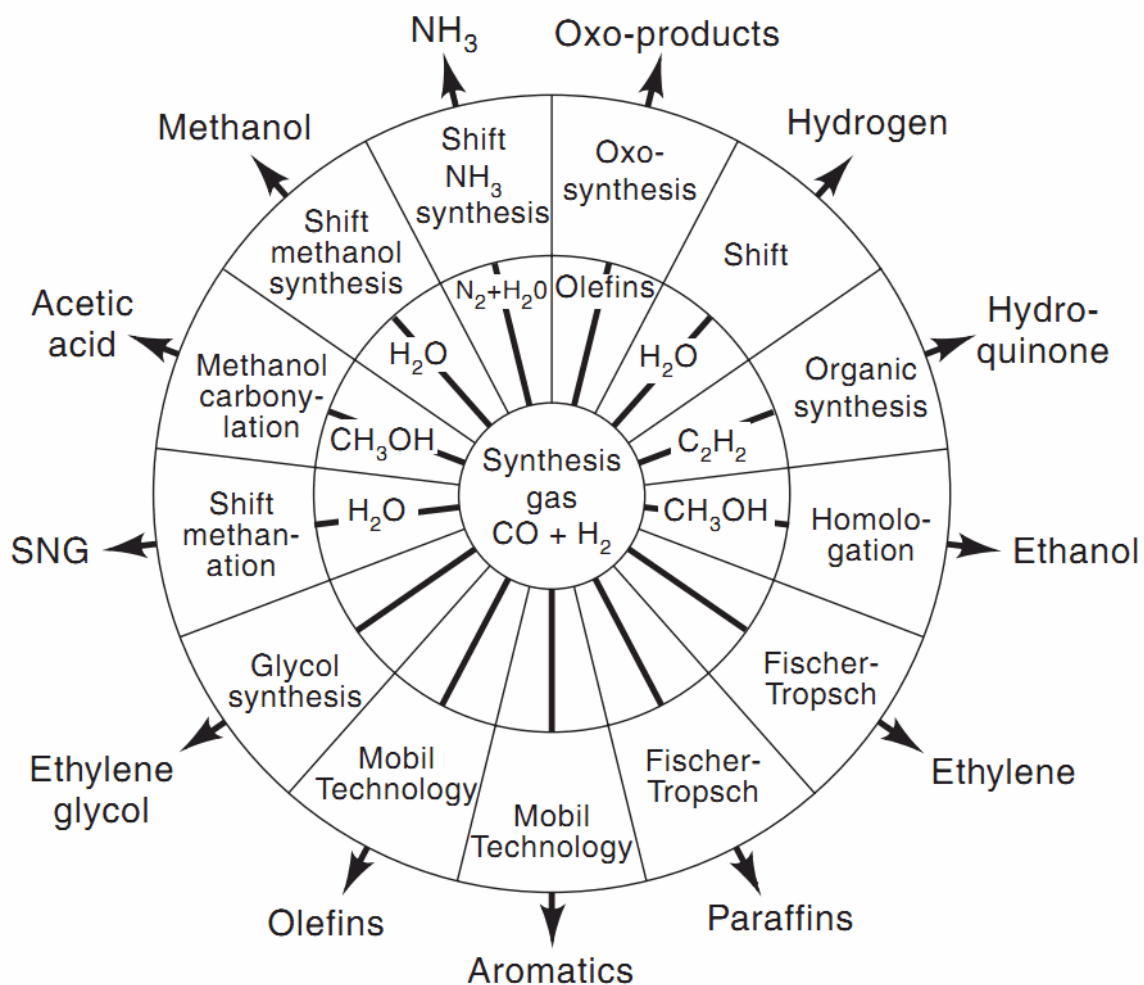
Figure 4-4 Synthesis gas (syngas) is predominately made from the partial oxidation of natural gas to CO and then producing hydrogen via the water–gas shift reaction. From syngas a large variety of valuable end products can be made. By making syngas using renewable energy, fossil fuel use can be avoided. This figure is from Kirk–Othmer.[20]

A

B
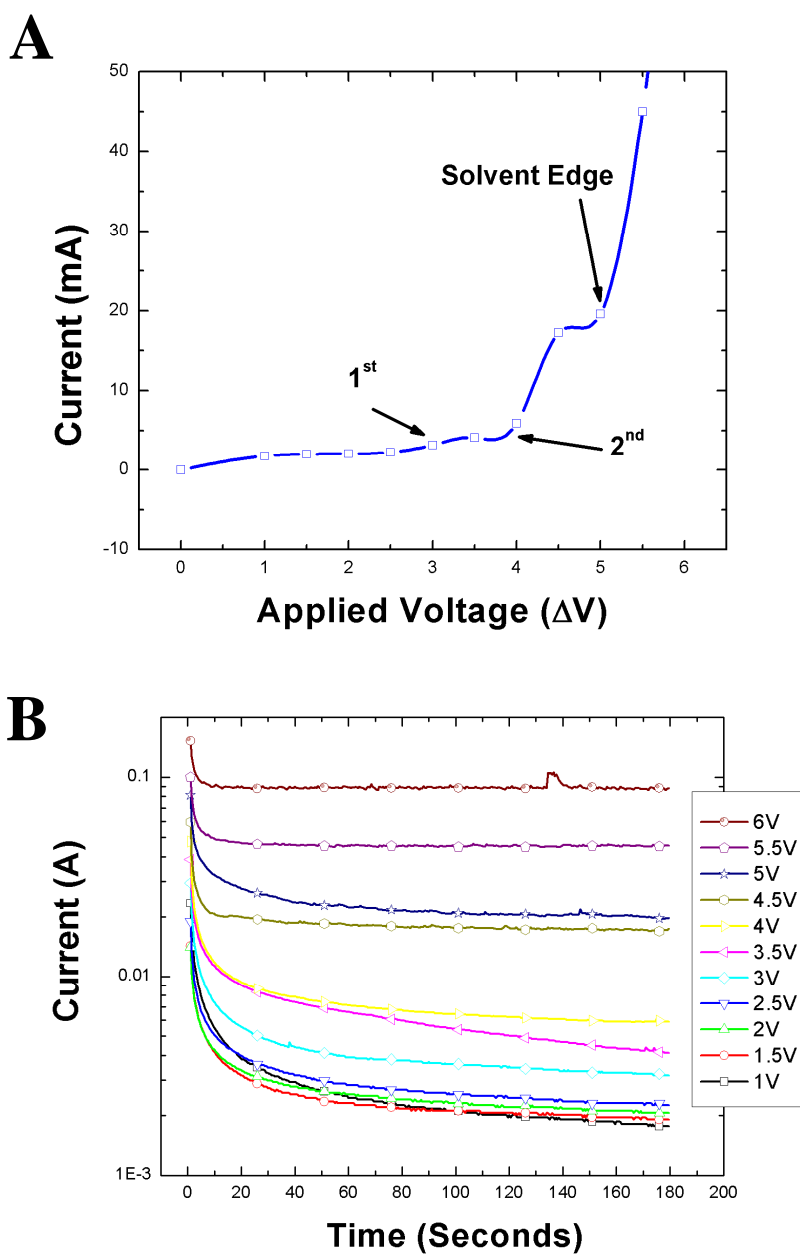
Figure 4-5 (A) The current after 3 minutes is used to construct the electrolyzer load curve. The first reduction occurs at 3.4V, the second at 4V, and the solvent edge at 5V. (B) Bulk electrolysis runs using 1mM Re-tBu in CH_3CN with 0.1M TBAH electrolyte under CO_2.
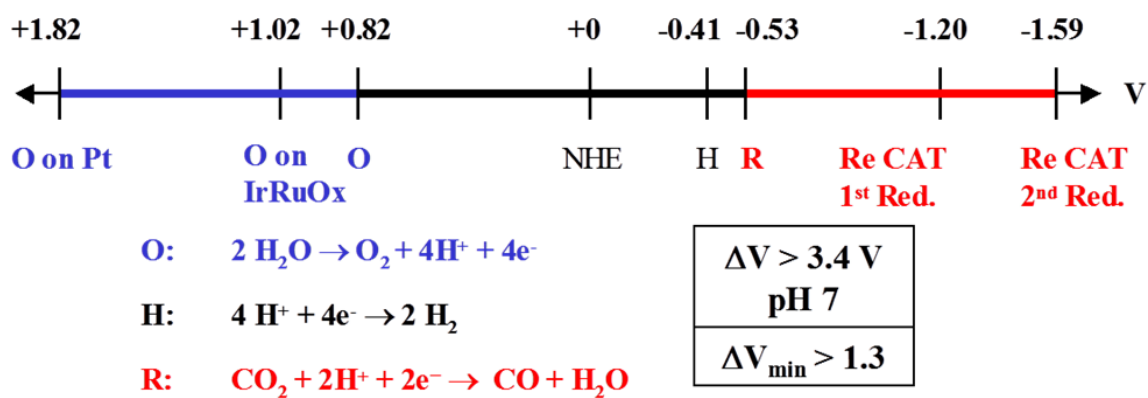
Figure 4-6 Theoretical voltages required for the electrolyzer showing the respective overpotentials for both the cathodic and anodic reactions. This shows a minimum practical voltage needed of 3.4V. Hydrogen reduction is also shown for comparison.

Cathode: $CO_2 + 2H^+ + 2e^- \rightarrow CO + H_2O$ $E_c = -1.59$ vs. NHE pH 7

Anode: $H_2O \rightarrow 2H^+ + \frac{1}{2}O_2 + 2e^-$ $E_a = +1.82$ vs. NHE pH 7

Net: $CO_2 \rightarrow CO + \frac{1}{2}O_2$ $\Delta E_{a-c} = 3.41$V
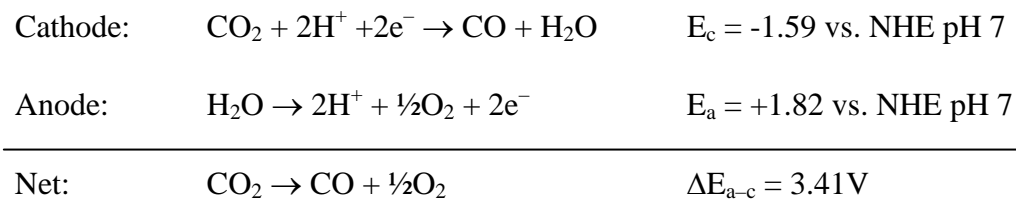
Scheme 4-1 The half reactions for CO_2 reduction and H_2O oxidation. The net reaction results in CO and O_2 production.
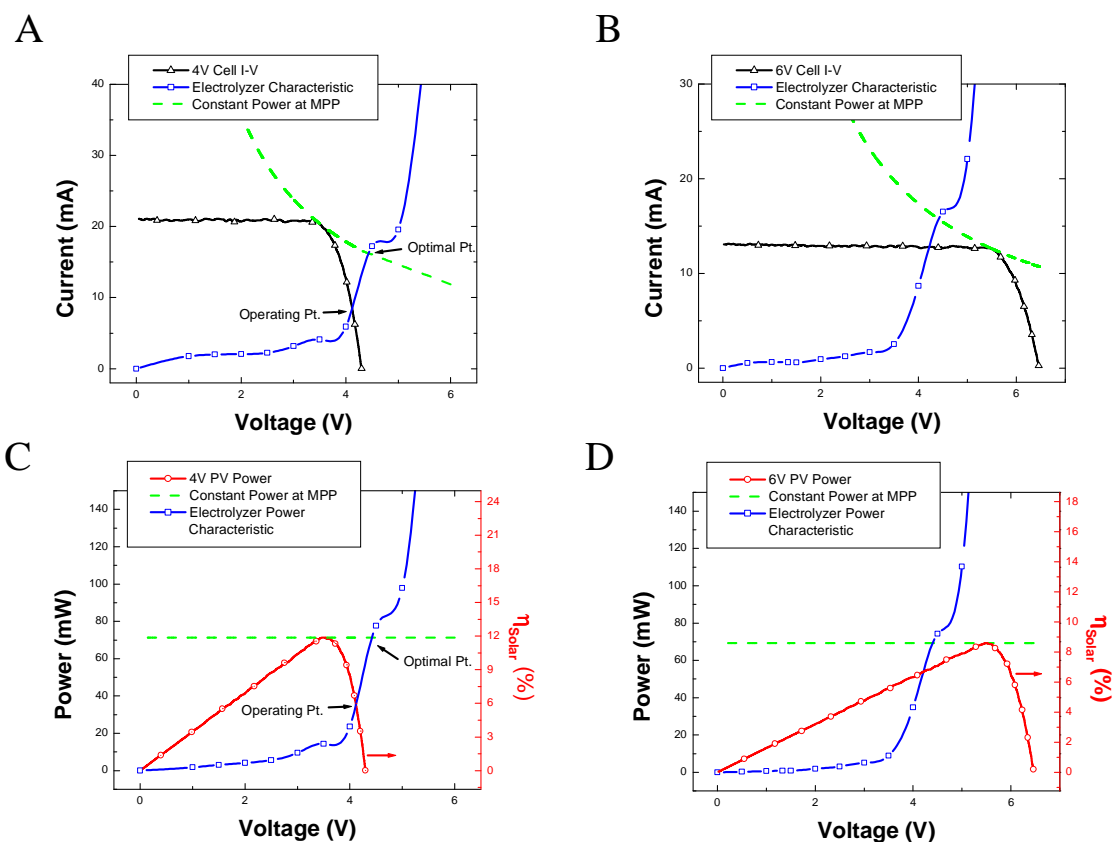
Figure 4-7 (A) The intersection of the I-V of the electrolyzer characteristic (blue -□-) and the solar cell (black -Δ-) sets the operating point. The constant power I-V (green dash) from the maximum power point intersects at the optimal point. The difference is the degree of mismatch. This is shown for a 4V solar cell at 1mM Re-tBu. (B) Repeated for a 6V solar cell at 2mM Re-tBu. (C) Plotting power vs. voltage further illustrates the power mismatch. The intersection of the solar cell power (red -o-) and the electrolyzer power (blue -□-) is the same operating point as A. The constant power I-V (green dash) from the maximum power point intersects the electrolyzer power at the optimal point (same as A). This is shown for a 4V solar cell at 1mM Re-tBu. (D) Repeated for a 6V solar cell at 2mM Re-tBu.
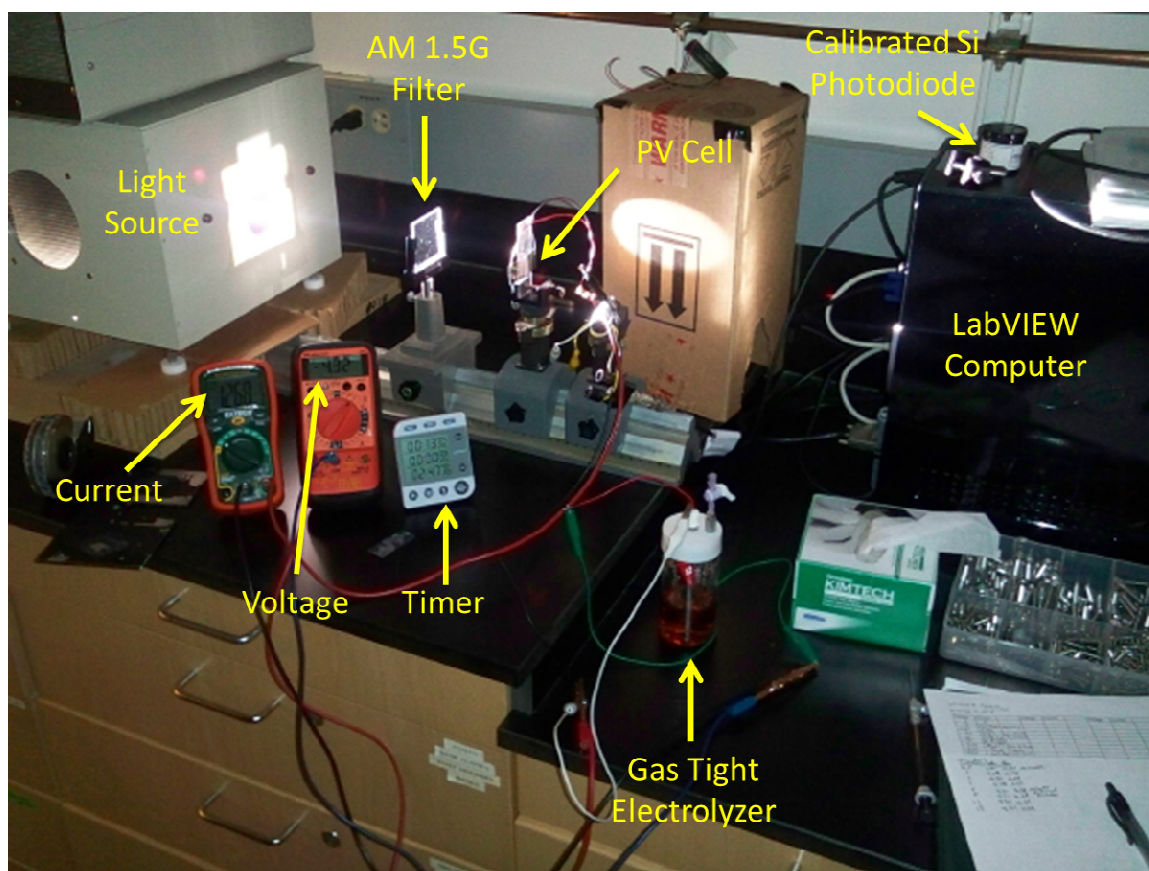
Figure 4-8 Photograph of the solar powered electrolyzer setup. A 450 W xenon light passes through an AM 1.5G filter before reaching the PV cell. The positive PV lead is connected to the anode and the negative lead connected to the cathode. The PV voltage and current are monitored with digital multimeters.

Table 4-1 Summary of the electrolysis results for the 4V (1mM Re-tBu) and 6V (2mM Re-tBu) coupled cells. The time is when gas chromatograph (GC) samples were extracted, the volume of CO produced is then computed from GC calibration curves, the coulombs integrated from the current, and the total efficiency computed using equation 4-2.

	Electrolysis Time (min)	Volume of CO Produced (mL)	Total Coulombs (C)	Peak Total Efficiency (%)
4 Volt Cell	88	5.90	45.8	2.1
6 Volt Cell	67	6.39	51.0	2.1
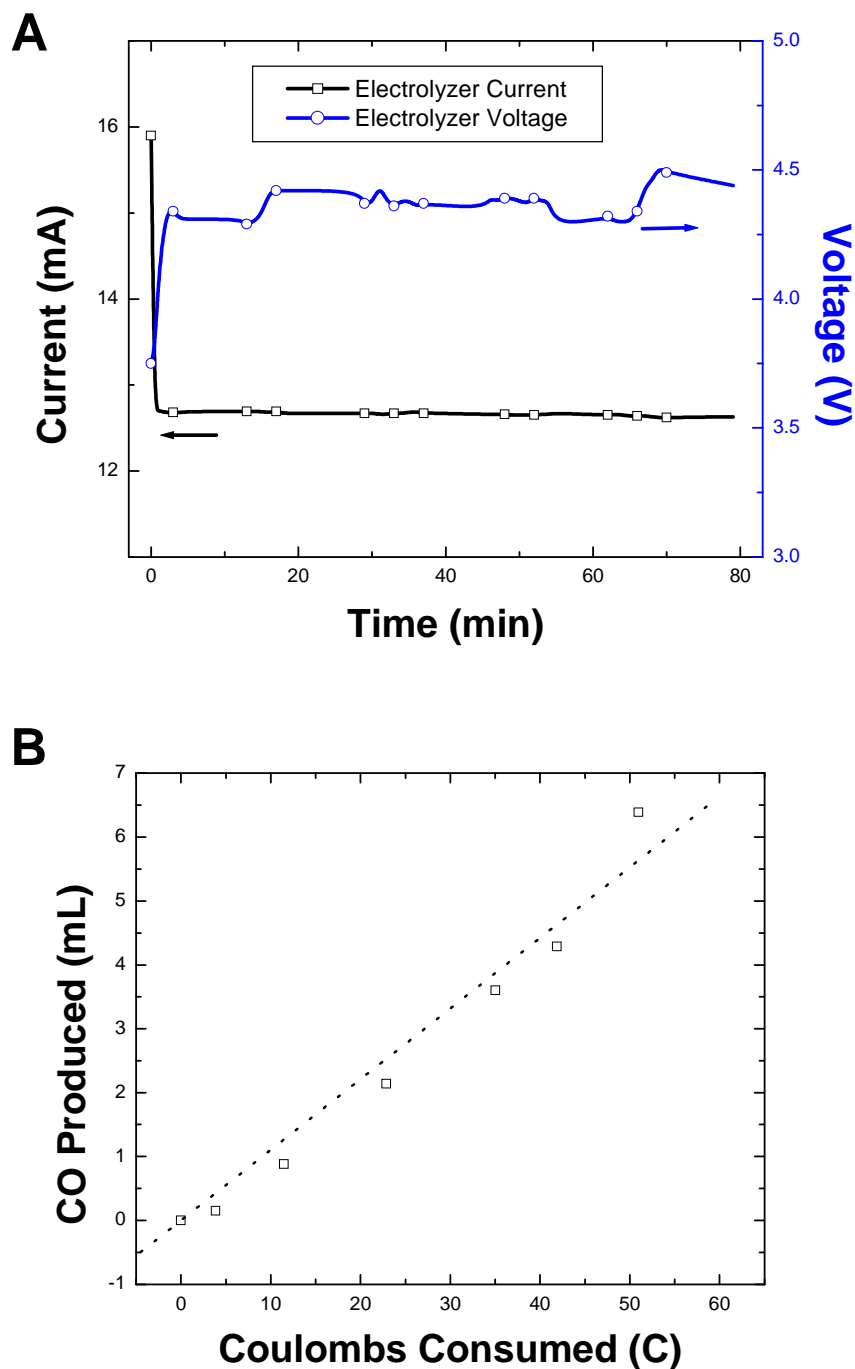
Figure 4-9 (A) The current and voltage output by a direct–coupled PV bulk electrolysis from the 6V solar cell as a function of time. (B) Volume of CO produced by the reduction of CO_2 using Re-tBu as a function of the amount of charge consumed.
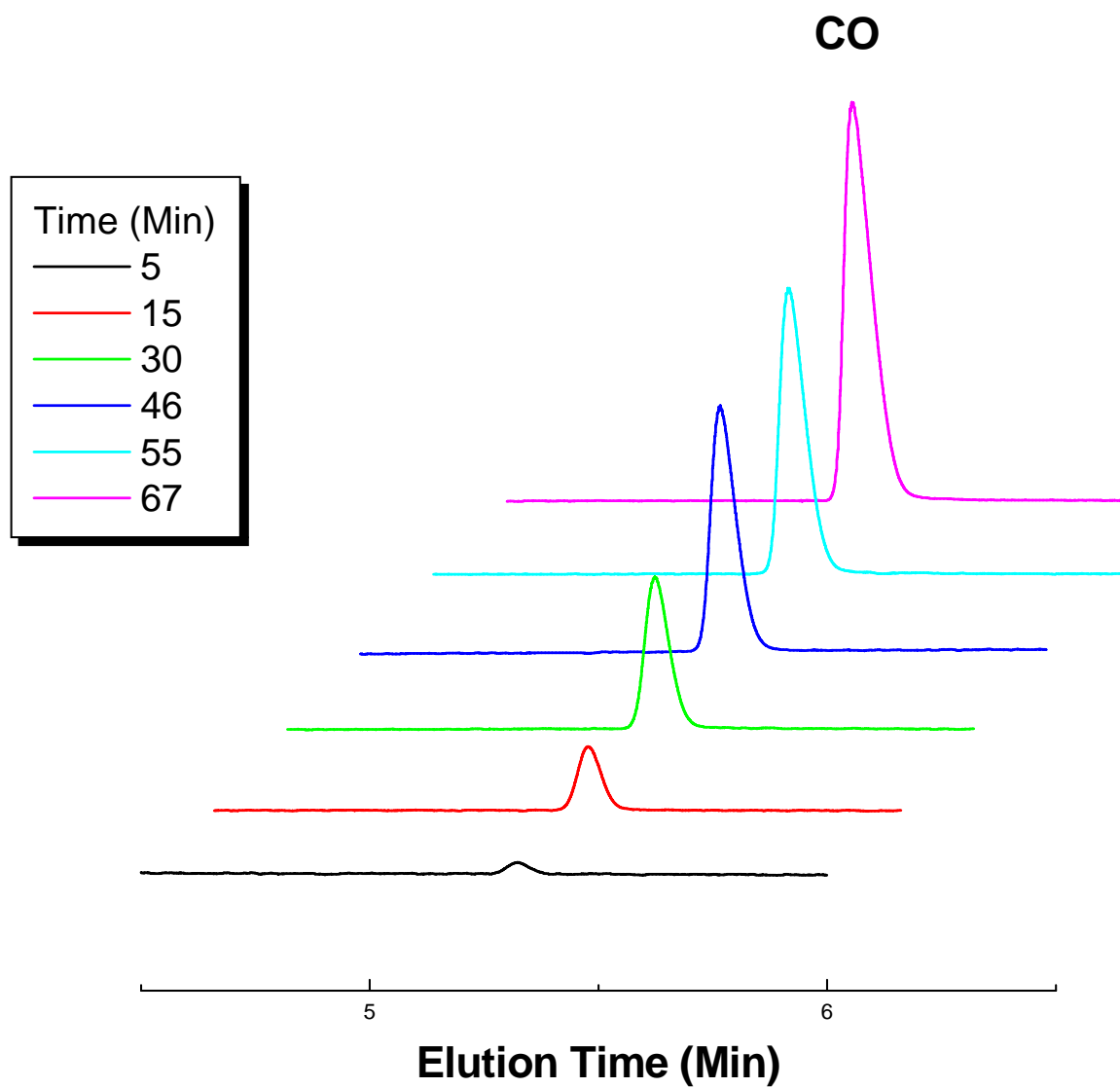
Figure 4-10 Gas chromatographs from controlled direct-coupled 6V solar cell electrolysis. CO eluted at 5.3 minutes and was verified with control samples of dilute CO.

4.9 REFERENCES

(1)   Garrett, A. B. Aluminum Metallurgy: Charles Martin Hall. *J. Chem. Ed.* **1962**, *39*, 415.

(2)   Leddy, J. J. The Chlor-Alkali Industry. *J. Chem. Ed.* **1980**, *57*, 640.

(3)   Grotheer, M. P. Electrochemical Processing, Inorganic. In *Kirk-Othmer Encyclopedia of Chemical Technology*; John Wiley & Sons, Inc., 2000.

(4)   Pickett, D. J. *Electrochemical Reactor Design*, 2nd Edition ed.; El Sevier: New York, NY, 1979.

(5)   Smieja, J. M.; Kubiak, C. P. Re(bipy−tBu)(CO)$_3$Cl−improved Catalytic Activity for Reduction of Carbon Dioxide: IR−Spectroelectrochemical and Mechanistic Studies. *Inorg. Chem.* **2010**, *49*, 9283-9289.

(6)   Fujita, E.; Creutz, C.; Sutin, N.; Szalda, D. J. Carbon Dioxide Activation by Cobalt(I) Macrocycles: Factors Affecting Carbon Dioxide and Carbon Monoxide Binding. *J. Am. Chem. Soc.* **1991**, *113*, 343-353.

(7)   Szalda, D. J.; Fujita, E.; Creutz, C. Cobalt(I), -(II), and -(III) Complexes of a Tetraaza 14−Membered Macrocycle, 5,7,7,12,14,14-Hexamethyl-1,4,8,11-Tetraazacyclotetradeca-4,11-Diene (L). Crystal and Molecular Structures of [CoL(CO)]ClO$_4$, trans-CoLCl$_2$, and cis-[CoL(CO$_3$)]ClO$_4$. *Inorg. Chem.* **1989**, *28*, 1446-1450.

(8)   Scovazzo, P.; Poshusta, J.; DuBois, D.; Koval, C.; Noble, R. Electrochemical Separation and Concentration of < 1% Carbon Dioxide from Nitrogen. *J. Electrochem. Soc.* **2003**, *150*, D91-D98.

(9)   Haines, R. J.; Wittrig, R. E.; Kubiak, C. P. Electrocatalytic Reduction of Carbon Dioxide by the Binuclear Copper Complex [Cu$_2$(6-(Diphenylphosphino)-2,2'−Bipyridyl)$_2$(MeCN)$_2$][PF$_6$]$_2$. *Inorg. Chem.* **1994**, *33*, 4723-4728.

(10)   Connelly, N. G.; Geiger, W. E. Chemical Redox Agents for Organometallic Chemistry. *Chem. Rev.* **1996**, *96*, 877-910.

(11)   Bard, A. J.; Faulkner, L. R. *Electrochemical Methods: Fundamentals and Applications 2nd Edition*; John Wiley & Sons: Hoboken, NJ, 2001.

(12)   Lewis, N. S.; Nocera, D. G. Powering the Planet: Chemical Challenges in Solar Energy Utilization. *Proc. Natl. Acad. Sci. U. S. A.* **2006**, *103*, 15729-15735.

(13)   Whitesides, G. M.; Crabtree, G. W. Don't Forget Long−Term Fundamental Research in Energy. *Science* **2007**, *315*, 796-798.

(14)   Field, C. B.; Behrenfeld, M. J.; Randerson, J. T.; Falkowski, P. Primary Production of the Biosphere: Integrating Terrestrial and Oceanic Components. *Science* **1998**, *281*, 237-240.

(15)   Mikkelsen, M.; Jorgensen, M.; Krebs, F. C. The Teraton Challenge. A Review of Fixation and Transformation of Carbon Dioxide. *Energy Env. Sci.* **2010**, *3*, 43-81.

(16)   Aresta, M.; Dibenedetto, A. Utilization of CO_2 as a Chemical Feedstock: Opportunities and Challenges. *Dalton Trans.* **2007**, 2975-2992.

(17)   Song, C. S. Global Challenges and Strategies for Control, Conversion and Utilization of CO_2 for Sustainable Development Involving Energy, Catalysis, Adsorption and Chemical Processing. *Catal. Today* **2006**, *115*, 2-32.

(18)   Leitner, W. Carbon Dioxide as a Raw Material: The Synthesis of Formic Acid and Its Derivatives from CO2. *Angew. Chem. Int. Ed.* **1995**, *34*, 2207-2221.

(19)   Rofer-DePoorter, C. K. A Comprehensive Mechanism for the Fischer−Tropsch Synthesis. *Chem. Rev.* **1981**, *81*, 447-474.

(20)   Worsham, P. R. Feedstocks, Coal Chemicals In *Kirk-Othmer Encyclopedia of Chemical Technology*, 2010; pp 1–25.

(21)   Smieja, J.; Sathrum, A.; Kubiak, C.; Benson, E. Electrocatalytic and Homogeneous Approaches to Conversion of CO_2 to Liquid Fuels. *Chem. Soc. Rev.* **2009**, *38*, 89-99.

(22)   Savéant, J.-M. Molecular Catalysis of Electrochemical Reactions. Mechanistic Aspects. *Chem. Rev.* **2008**, *108*, 2348-2378.

(23)   Hawecker, J.; Lehn, J. M.; Ziessel, R. Electrocatalytic Reduction of Carbon Dioxide Mediated by Re(bipy)(CO)$_3$Cl (bipy = 2,2'−bipyridine). *J. Chem. Soc. Chem. Comm.* **1984**, 328.

(24)   Hawecker, J.; Lehn, J. M.; Ziessel, R. Photochemical and Electrochemical Reduction of Carbon Dioxide to Carbon Monoxide Mediated by (2,2'-Bipyridine) Tricarbonylchlororhenium(I) and Related Complexes as Homogeneous Catalysts. *Helv. Chim. Acta* **1986**, *69*, 1990-2012.

(25)   Calvin, M. Artificial Photosynthesis: Quantum Capture and Energy Storage. *Photochem. Photobio.* **1983**, *37*, 349-360.

(26)   Agrawal, R.; Singh, N. R.; Ribeiro, F. H.; Delgass, W. N. Sustainable Fuel for the Transportation Sector. *Proc. Natl. Acad. Sci. U. S. A.* **2007**, *104*, 4828-4833.

(27)   Klass, D. L. *Biomass for Renewable Energy, Fuels, and Chemicals*; Academic Press: San Diego, CA, 1998.

(28)   *The DOE   funded   mission of JCAP (http://www.solarfuelshub.org/) is to demonstrate a scalable and cost-effective solar fuels generator that, without use of rare materials or wires, robustly produces fuel from the sun 10 tim es more efficiently than typical current crops.*

(29)   Gibson, T. L.; Kelly, N. A. Optimization of Solar Powered Hydrogen Production Using Photovoltaic Electrolysis Devices. *Int. J. Hydro. Energy* **2008**, *33*, 5931-5940.

(30)   Gibson, T. L.; Kelly, N. A. Predicting Efficiency of Solar Powered Hydrogen Generation Using Photovoltaic−Electrolysis Devices. *Int. J. Hydro. Energy* **2010**, *35*, 900-911.

(31)   Artuso, P.; Zuccari, F.; Dell'Era, A.; Orecchini, F. PV−Electrolyzer Plant: Models and Optimization Procedure. *J. Sol. Energy Eng.* **2010**, *132*, 031016.

(32)   Kroposki, B.; Levene, J.; Harrison, K.; Sen, P. K.; Novachek, F. Electrolysis: Information and Opportunities for Electric Power Utilities; NREL TP-581-40605, 2006.

(33)   Esram, T.; Chapman, P. L. Comparison of Photovoltaic Array Maximum Power Point Tracking Techniques. *IEEE Trans. Energy Conv.* **2007**, *22*, 439-449.

(34)   Emery, K. A.; Osterwald, C. R. Solar Cell Efficiency Measurements. *Sol. Cells* **1986**, *17*, 253-274.

(35)   Fu, Q. X.; Mabilat, C.; Zahid, M.; Brisse, A.; Gautier, L. Syngas Production via High-Temperature Steam/CO_2 Co−Electrolysis: An Economic Assessment. *Energy Env. Sci.* **2010**, *3*, 1382-1397.

(36)   Shockley, W.; Queisser, H. J. Detailed Balance Limit of Efficiency of p−n Junction Solar Cells. *J. App. Phys.* **1961**, *32*, 510-519.

(37)   Beley, M.; Collin, J. P.; Ruppert, R.; Sauvage, J. P. Nickel(II) Cyclam − An Extremely Selective Electrocatalyst for Reduction of CO_2 in Water. *J. Chem. Soc. Chem. Comm.* **1984**, 1315-1316.

(38)   McDaniel, N. D.; Bernhard, S. Solar Fuels: Thermodynamics, Candidates, Tactics, and Figures of Merit. *Dalton Trans.* **2010**, *39*, 10021-10030.

(39)   Khaselev, O.; Bansal, A.; Turner, J. A. High−Efficiency Integrated Multijunction Photovoltaic/Electrolysis Systems for Hydrogen Production. *Int. J. Hydro. Energy* **2001**, *26*, 127-132.

(40)   Clarke, R. E.; Giddey, S.; Ciacchi, F. T.; Badwal, S. P. S.; Paul, B.; Andrews, J. Direct Coupling of an Electrolyser to a Solar PV System for Generating Hydrogen. *Int. J. Hydro. Energy* **2009**, *34*, 2531-2542.

CHAPTER 5

KINETICS AND LIMITING CURRENTS OF

HOMOGENEOUS AND HETEROGENEOUS

ELECTROCATALYTIC EC' SYSTEMS FOR

SOLAR GENERATED FUELS

5.1 ABSTRACT

The theoretical performance of model homogeneous and heterogeneous electrocatalytic EC' systems for freely diffusing and surface–attached systems is compared. Electrochemical conversions such as water or carbon dioxide splitting are fields of tremendous interest and recent growth. These areas are significant as they are related to solar based fuels and energy storage. At present, it is not clear whether homogeneous catalysis, heterogeneous catalysis, or a combination of both will provide the best solution for solar energy applications. In the power range of the air mass 1.5 global solar flux, homogeneous and heterogeneous systems with overall turnover frequencies (TOF) of 10–1000 s^{-1} are found to be competitive with each other. The surface and solution concentrations of catalyst determine the required rate and other relevant system constraints. At higher current densities, the modeled heterogeneous system requires a lower TOF than the corresponding homogeneous system. The development of faster catalysts with lower overpotential is needed, while maintaining the desired selectivity and kinetics.

5.2 INTRODUCTION

Electrochemical conversions such as water or carbon dioxide splitting are fields of tremendous interest and recent growth. At present, it is not clear whether homogeneous catalysis, heterogeneous catalysis, or a combination of both will provide the best solution for solar energy applications. Homogeneous and heterogeneous catalysis

are historically rich fields that provide the basis of most of the industrial scale chemical transformations used today.[1] It is difficult to draw generalizations from these enormous fields. This chapter looks specifically at electrocatalysis; the transfer of electrons to drive catalytic reactions at or near an electrode surface. Electrocatalysis enables the potentially efficient and rapid conversion of electrical energy into chemical energy and is currently being investigated for generating solar based fuels via proton and carbon dioxide reductions.[2] One approach is to use semiconductor electrodes to directly harness solar energy via photoelectrochemistry (PEC).[3,4] In such devices, the light absorber and electrode surface area are generally the same. Promising devices have been developed based on photoanodes for water oxidation,[5] or photocathodes for proton reduction.[6] Often in such systems an electrocatalyst is attached to the electrode surface or dissolved in the solution to lower the required energy input and improve the reaction kinetics.[2] In PEC, the governing current density depends on both the supply of electrons via solar photons and the consumption of electrons by the electrocatalyst. The consumption is determined by a combination of the turnover frequency (TOF) and mass transport of the species involved. Therefore it is appropriate to apply the steady state conditions provided by the relevant solar flux to such photoelectrochemical systems. By examining the coupling of electrocatalysis to photoelectrochemistry, an appropriate range of values for the TOF required for homogeneous and heterogeneous systems is determined. The significant merits and the advantages and disadvantages of each approach are then compared.

In designing a scalable reactor with a given catalytic TOF, it is critically important to be able to predict whether the limiting current density of a homogeneous or

a heterogeneous system would be superior. In order to adequately answer this question one needs to derive the current density equations that govern electrocatalytic systems for freely diffusing and surface bound systems. If the catalyst is incorporated with a photoelectrode, such as in the case of photoelectrochemistry, then the relevant voltages and current densities from the maximum solar flux will set boundaries that are insightful in the modeling and optimization of the coupled systems. Other effects due to the electrolyte, solvent, temperature, and the distance of an attached catalyst from electrode are not included in the scope of this chapter.

5.3 DETERMINATION OF THE ELECTROCATALYTIC MECHANISM

Electron transfer with a coupled chemical reaction is a broad field with many variations. Cyclic voltammetry is typically used to experimentally diagnose the type of mechanism involved in a particular reaction. A plot of $i_p/v^{1/2}$ vs. v can be constructed,[7,8] where i_p is the peak current and v is the scan rate. This separates the diffusion component of scan rate from the overall kinetics, thereby giving a characteristic response curve that can be used to identify the appropriate mechanism.[7] With proper diagnosis, mathematical models can be developed, and equations for the expected current and voltage behavior derived. For this electrocatalytic comparison, the EC' mechanism where E represents an electron transfer at the electrode surface, and C' represents a following homogenous catalytic chemical reaction was employed.[9] Further information on other mechanisms can

be found in previous work by Bard and Faulkner,[10] as well as extensive work by Savéant.[11,12]

The generalized form of the EC' reaction is shown in scheme 5-1. **C** and **C'** are catalytic species, **S** is the substrate consumed and **P** is the final reaction product. In this treatment, **S** and **P** are assumed to be non-electroactive species in the voltage region relevant to the **C/C'** couple.

$$C + ne^- \underset{}{\overset{k_{et}}{\rightleftharpoons}} C'$$

$$\text{Catalytic Feedback}$$

$$C' + S \underset{}{\overset{k_{cat}}{\rightleftharpoons}} C + P$$
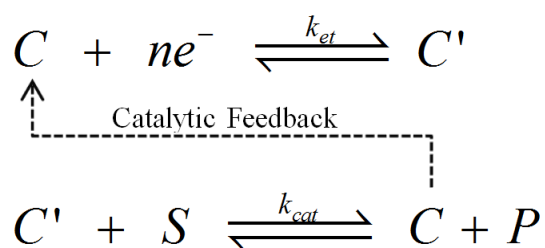
Scheme 5-1 EC' mechanism

First n electrons are transferred to the electrocatalyst **C** with the rate constant k_{et}, yielding the catalytically active oxidation state **C'**. Then **C'** reacts with the substrate **S** with the rate constant k_{cat}, creating the product **P** while regenerating **C**. An example of this reaction is the two electron reduction of CO_2 to CO by the reduced form of *fac*-Re(2,2'-bipyridyl)CO_3Cl.[13]

5.4 HOMOGENEOUS EC' RATE LIMITED CURRENT

5.4.1 Assumptions and Initial Conditions

The local environment of a homogeneous catalyst can be described as a freely diffusing catalyst in the same phase (i.e., solution) that contains the substrate. The

mathematical analysis presented here has been adapted from Delahay, et al.[14] and Savéant, et al.[15] and applied to EC' reactions. Consider a planar electrode as shown in Figure 5-1. The following assumptions must be made to proceed with the analysis: 1) the electrode is planar, 2) **C** is easier to reduce than **S**, 3) the voltage is sufficiently negative to reduce **C**, such that $k_{et} \gg k_{cat}$ and the rate limiting step is the catalytic chemical reaction, 4) [**S**] is large, such that the catalytic chemical reaction does not change the bulk concentration, 5) the reaction is at steady state, such that time t is large, 6) the product **P** does not affect catalysis, 7) k_{cat} is slow enough not to significantly change [**S**], and 8) diffusion limited mass transport of **C**. A more detailed discussion of k_{et} at semiconductor surfaces can be found in a review by Lewis.[16] These assumptions are reasonable for many electrocatalytic systems and allow for an analytical solution to the differential equations describing the system.

5.4.2 Derivation of Catalyst Flux

In order to calculate the EC' current one needs to derive the flux of relevant species at the electrode surface. By judicious choice of the appropriate differential equations, initial conditions, and boundary conditions, one can solve for the expected concentration gradient and resulting flux. The kinetics of the reaction can be written in terms of [**C**] (assuming activity coefficients of unity):

$$\left(\frac{\partial[C]}{\partial t}\right)_{kinetic} = k_{cat}\,'[C\,'][S] - k_{-cat}[C] \approx k_{cat}\,'[C\,'][S] \qquad \textbf{(5-1)}$$

where t is electrolysis time elapsed, [concentrations] are in moles cm^{-3}, k are rate constants in s^{-1}, and k_{cat}' is a second order rate constant with units of in s^{-1} mol^{-1} such that $k_{cat} = k_{cat}'[S]$. The forward rate $k_{cat} \gg k_{-cat}$, the reverse rate, because of the irreversible catalytic reaction, therefore the second term in equation 5-1 is negligibly small and removed. Since [S] $\gg$ [C] and [C'], [S] is unchanged by the distance x from the electrode surface or time t. This leads to the pseudo first order conditions where k$_{cat}$ is saturated and independent of [S]. By applying Fick's second law for the total change in concentration due to diffusion between two planes at x and $x + dx$, and adding in the additional term for the kinetics of the reaction derived in equation 5-1, one obtains:

$$\left(\frac{\partial [C]}{\partial t} \right)_{total} = D_C \frac{\partial^2 [C]}{\partial x^2} + k_{cat}'[C'][S] \qquad \textbf{(5-2)}$$

where D_C is the diffusion coefficient of **C** in cm^2 s^{-1}. Applying Duhamel's theorem[14] for linear diffusion where [C]$_o$ is the initial bulk concentration of **C**:

$$[C'] = \left(\frac{D_C}{D_{C'}} \right)^{\frac{1}{2}} \left([C]_o - [C] \right) \qquad \textbf{(5-3)}$$

For typical systems $D_C \approx D_{C'}$, and the notation is simplified by using only D_C and assuming their ratio will be near unity. Applying the initial and boundary conditions when the potential is stepped to a sufficiently negative value:

$$Initial\, Conditions: \qquad t = 0, [C] = [C]_o$$

$$Boundary\, Conditions: t > 0, \; x = 0, [C] = 0$$

and then combining equations 5-2 and 5-3 yields the differential equation:

$$\frac{\partial [C]}{\partial t} = D_C \frac{\partial^2 [C]}{\partial x^2} + k_{cat}'[S]([C]_o - [C]) \qquad \textbf{(5-4)}$$

and the solution for $[C]$ with respect to x and t is:

$$[C] = [C]_o \left[\begin{array}{l} 1 - \frac{1}{2}\exp\left[-x\left(\frac{k_{cat}'[S]}{D_C}\right)^{\frac{1}{2}}\right] erfc\left[\frac{x}{2(D_C t)^{\frac{1}{2}}} - (k_{cat}'[S]t)^{\frac{1}{2}}\right] \\ \\ - \frac{1}{2}\exp\left[x\left(\frac{k_{cat}'[S]}{D_C}\right)^{\frac{1}{2}}\right] erfc\left[\frac{x}{2(D_C t)^{\frac{1}{2}}} + (k_{cat}'[S]t)^{\frac{1}{2}}\right] \end{array} \right] \qquad \textbf{(5-5)}$$

where *erfc* is the complementary Gauss error function. From equation 5-5 it can be observed that as k_{cat} increases, the $[C]$ near the surface increases because of the regeneration reaction. The limits of equation 5-5 shows that:

$$\lim_{k_{cat} \to \infty} [C] = [C]_o$$

which is to be expected, because at an infinitely high k_{cat}, **C** is regenerated immediately after being consumed. At the other extreme:

$$\lim_{k_{cat} \to 0} [C] = [C]_o \left[1 - erfc\left(x/(4D_C t)^{\frac{1}{2}}\right)\right]$$

which when solved for the current at the electrode surface (x=0), yields the solution of simple linear diffusion, i.e. the Cottrell equation[17] without any catalytic reaction.

5.4.3 Derivation of the Catalytic Current

In order to solve for the current, one applies Fick's first law using the concentration profile from equation 5-5, taking into account the charge needed to reduce one mole of **C** at the electrode surface. The current can be obtained as:

$$i = nFAJ_C = nFAD_C \frac{\partial[C]}{\partial x} \qquad \textbf{(5-6)}$$

where i is the current in amperes, n in the number of electrons transferred per reaction, F is the Faraday constant, A is the area of the electrode in cm^{-2}, and J_C is the flux of **C** in mol cm^{-2} s^{-1}. J_C used here is not to be confused with current density $j = i/A$ in amperes cm^{-2}. When the concentration profile from equation 5-5 is differentiated and evaluated at the electrode surface one obtains:

$$i = nFA(D_C)^{\frac{1}{2}}[C]_o \left[\underbrace{\frac{1}{(\pi t)^{\frac{1}{2}}} \exp\left[(-k_{cat}'[S]t)^{\frac{1}{2}}\right]}_{Pure\ Diffusion} + \underbrace{(k_{cat}'[S])^{\frac{1}{2}} erf\left[(k_{cat}'[S]t)^{\frac{1}{2}}\right]}_{Pure\ Kinetic} \right]$$

$$\textbf{(5-7)}$$

The first term in equation 5-7 represents a pure diffusional current when the exponential argument $k_{cat}'[S]t$ is small, i.e., at short times. The second term is a pure kinetic current when $k_{cat}'[S]t$ is large, i.e., at long times. The middle region for certain values of $k_{cat}'[S]t$ will be governed by both terms. To examine equation 5-7 in more detail, one looks at the extremes, $\lim_{k_{cat} \to \infty} i = \infty$. It was earlier assumed that [**S**] is constant, which is not true for near the electrode surface when k_{cat} is high. In fact, local depletion of [**S**] will cause the current to plateau at a lower value than predicted from equation 5-7. Additional second-order effects have been calculated previously[15] to

account for such deviations. When electrocatalysis stops, i.e., $\lim_{k_{cat} \to 0} i = nFA[C]\left(D_C / \pi t\right)^{\frac{1}{2}}$ the familiar Cottrell equation based on the simple linear diffusion of non–catalytic species is observed. Thus, a solution is obtained for the expected current for a homogeneous EC' reaction on a planar surface that can be used for modeling.

5.4.4 Derivation of the Steady–State Current

At long times equation 5-7 becomes:

$$\lim_{t \to \infty} = i_{\lim} = nFA[C]\left(k_{cat}'[S]D_C\right)^{\frac{1}{2}} \qquad \textbf{(5-8a)}$$

$$k_{cat} = TOF = k_{cat}'[S] = \frac{1}{D_C}\left(\frac{i_{\lim}}{nFA[C]}\right)^2 = \frac{1}{D_C}\left(\frac{j_{\lim}}{nF[C]}\right)^2 \qquad \textbf{(5-8b)}$$

This results in equations 5-8a, and the rearrangement 5-8b. This very important result shows that an EC' steady state limiting current depends on the catalytic kinetics, catalyst concentration, and diffusion of **C**, but is independent of time. As k_{cat}' increases, so does the limiting current, and stronger a deviation from simple Cottrell behavior is observed. From equation 5-8a one can see that the limiting current is directly proportional to the surface area and catalyst concentration, while it varies with the square root of the turnover frequency (recall TOF = $k_{cat}'[\textbf{S}] = k_{cat}$), and diffusion coefficient.

5.4.5 Steady–State Reaction Layer Thickness

Another interesting result from this analysis is that nearly all the [**C'**] is found a reaction layer near the surface. This was shown by Savéant[15] to be:

$$x_{C'} = \left(\frac{D_C}{k_{cat}\,'[S]} \right)^{\frac{1}{2}} \quad \textbf{(5-9)}$$

Equation 5-9 is similar to a diffusion length with the additional catalytic reaction of **C'** reacting with **S** to form **P**. Faster catalysts will have a smaller reaction layer and require less solution depth. An example thickness can be calculated from a reported CO_2 electrocatalyst, Re(4,4'-di-*tert*-butyl-2,2'-bipyridine)(CO)$_3$Cl,[18] where $D_C = 8.1\times10^{-6}$ cm^2 s^{-1} and $k_{cat} = 260$ s^{-1}, resulting in an $x_{C'} = 1.8$ µm. This example demonstrates how little of the bulk solution is active in homogeneous electrocatalysis.

5.4.6 Homogeneous EC' Summary

To summarize the analysis of a homogeneous EC' system, the diffusion limited current for EC' is larger than simple Cottrell current as derived in equation 5-7. This is because **C** is continuously restocked by the following catalytic chemical reaction, thus increasing the net flux of **C** to the surface, allowing for additional current as shown in scheme 5-1. On short timescales the limiting current will be similar to a non-catalytic EC reaction, while for longer timescales the limiting current will deviate and be larger. By performing bulk electrolysis on an EC' system, and then measuring the limiting current, TOF can be calculated from equation 5-8b. If the TOF is substantially large, then the local concentration of **S** near the surface will be depleted and the limiting current will be

a mixture of kinetic and diffusional parameters. In this case mass transport can be controlled using a rotating disc electrode.

5.4.7 Current Response and TOF at Different Catalyst Concentrations

With a homogeneous relationship describing the TOF and the limiting current density (j_{lim}), equation 8b can be plotted for different electrocatalyst concentrations as shown in Figure 5-2. As expected, the higher the current density, the greater the demand on the TOF of the electrocatalyst. The exponential relationship causes the range of TOF values to vary over 12 orders of magnitude for only 6 orders of magnitude in the current density domain. Conversely, the slower the TOF the lower the maximum capacity for current density. This can be relaxed by increasing the electrocatalyst concentration as shown over the ranges of 0.01–100 mM. However, as noted in the previous analysis, for high TOF values the current is expected to be lower than the predicted limiting current density due to mass transport limitations and local depletion of the substrate. At higher catalyst concentrations, the assumption that $[S] \gg [C]$ may not be valid and may result in similar local depletion even at relatively low TOF values. Nevertheless, TOF is critically linked to the current density at an electrode surface. Later, these results will be compared to the surface–attached heterogeneous case with current density values constrained by the solar flux.

5.5 HETEROGENEOUS EC' RATE LIMITED CURRENT

5.5.1 Assumptions and Initial Conditions

The local environment of a heterogeneous catalyst can be described as a surface bound species in a different phase (i.e., solid) than the solution containing the substrate.[19] The mathematical analysis presented here has been adapted from Armstrong, et al.[20] and applied to an EC' system. In this approach the surface bound species is treated similarly to an adsorbed electrocatalytic enzyme. Consider a planar electrode as shown in Figure 5-3 with an attached electrocatalyst. The electron transfer from the surface is assumed to be fast such that $k_{et} \gg k_{cat}$, therefore the rate limiting step is the catalytic chemical reaction in scheme 5-1. This resembles the Butler-Volmer formalism for electron transfer rather than Marcus theory.[21] One significant warning is that if the driving force is made too high by applying a large electrochemical potential, the observed limiting current may be lower than expected due to reaching the Marcus plateau region. Murray, et al.[22] have shown that the crossover occurs when the applied overpotential is greater than ~30% of the reorganizational energy of the electrode reaction. If the attachment itself is resistive towards electron transfer, this introduces complications that can be accounted for with further modeling.[20] The first seven assumptions are used from the homogeneous case, leaving out the diffusion limited mass transport of the catalyst, because it is attached. It should also be noted that if the surface concentration (Γ_C) is high and/or the TOF is very high, then the substrate supply may become mass transport limited and a decrease from

the expected current observed. If it is mass transport limited, then one can use rotating disc voltammetry to separate the hydrodynamics.

A homogeneous electrocatalyst can be directly adsorbed,[21] polymerized,[23] or covalently tethered[24] to an electrode surface shown generically in Figure 5-3.[25,26] For this analysis it is assumed that k_{cat} does not change upon attachment of the electrocatalyst to the surface. Retention of electrocatalytic activity has been recently demonstrated by Meyer, et al.[24] for a water oxidation catalyst. For a surface attached EC' case a kinetic limiting current will be shown. Surface–bound electrocatalysis has been studied with enzymatic systems.[21] These biologically important catalysts exhibit redox–active behavior, show high specificity, low energy barriers, and fast reaction rates. Enzymes are often adsorbed onto electrode surfaces in order to probe reaction kinetics and elucidate the mechanism(s) involved. One major advantage of heterogeneous systems is that very small quantities of catalyst are required. This makes the surface adsorption method attractive for protein-film voltammetry.

5.5.2 Derivation of the Steady–State Current

Starting with the well–developed theory of Michaelis-Menten enzyme catalysis with a slight modification to the Michaelis constant K_m using the reaction shown in scheme 5-1:

$$K_m = \frac{k_{-et} + k_{cat}}{k_{et}} \qquad \textbf{(5-10)}$$

where k_{-et} is the back electron transfer. It has been shown that for a surface bound redox enzyme (electrocatalyst) that:[20]

$$i_{cat} = \frac{nFA\Gamma_C k_{cat}'[S]}{[S]+K_m} \qquad \textbf{(5-11)}$$

where Γ_C is the surface concentration in mol cm^{-2}. For an applied voltage greater than the electrocatalyst redox potential, $k_{et} \gg k_{-et}$, and when $k_{et} \gg k_{cat}$, then K_m will be quite small. This will make it easier to satisfy the condition that $[S] \gg K_m$ simplifying equation 5-11 to:

$$i_{lim} = nFA\Gamma_C k_{cat} \qquad \textbf{(5-12a)}$$

$$k_{cat} = \frac{i_{lim}}{nFA\Gamma_C} = \frac{j_{lim}}{nF\Gamma_C} \qquad \textbf{(5-12b)}$$

equations 5-12a, and the rearrangement 5-12b. Similar to the homogeneous case, an important result that follows is that a surface bound EC' steady state limiting current depends only on the catalytic kinetics and surface concentration, but is independent of time. From equation 5-12a it can be sees that the limiting current is directly proportional to surface area, surface concentration, and TOF.

5.5.3 Heterogeneous EC' Summary

To summarize the analysis of a heterogeneous EC' system: current through a surface electrocatalyst is limited strictly by the catalytic TOF under the conditions described above. This analysis neglects any rate limiting effect due to interfacial electron transfer. That effect if problematic may be decreased by increasing the electrochemical

driving force. By performing bulk electrolysis on an EC' system, and measuring the limiting current, equation 5-12b allows the calculation of k_{cat} and therefore the TOF. If the TOF is substantially large, then the local **S** surface concentration will be depleted and the limiting current will be a mixture of kinetic and diffusional parameters. In this case the mass transport of **S** can be increased by faster rotation rates according to the Levich equation.[20]

5.5.4 Current Response and TOF at Different Γ_{cat}

With a relationship describing the heterogeneous TOF and the limiting current density (j_{lim}), equation 5-12b is plotted for different electrocatalyst surface concentrations as shown in Figure 5-4. Also provided is Table 5-1 which shows appropriate surface concentration values in common unit notations. Higher current densities demand higher TOF, but in contrast to the homogenous case the relationship is linear. The heterogeneous slope on a log plot is half that of the homogeneous case. The required TOF can be reduced by increasing the surface electrocatalyst concentration as shown over the ranges of 1.7×10^{-13} to 1.7×10^{-9} mol cm^{-2}. A large electrocatalyst will require a higher TOF because of the increase in molecular surface area, whereas a smaller electrocatalyst can have a lower TOF and maintain the same current due to increased catalyst concentration on the surface. For high TOF values the catalyst will consume **S** faster than the restocking of **S** by diffusion limited mass transport. This will deplete the local surface concentration, resulting in a lower measured current than predicted by equation 5-12b. Again, electrocatalytic TOF is critically linked to the current density at an electrode surface.

5.6 CURRENT DENSITIES RELATING TO THE AM1.5G SOLAR FLUX

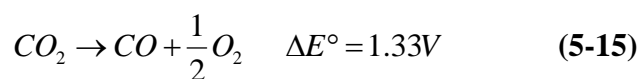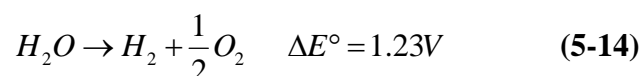### 5.6.1 Variable Solar Insolation Due to Air Mass

The illumination intensity of sunlight on the Earth's surface depends on a number of factors including latitude, time of day, time of year, solar activity, weather events, etc. Air Mass (AM) refers to the path length of atmosphere that is between a specific location and the sun. Since the atmosphere absorbs portions of the solar spectrum, the thicker the AM the lower the solar power intensity. AM 0 at 1360 W m^{-2} (also called the solar constant) refers to the top of the atmosphere, whereas AM 1 refers to when the sun is directly overhead and passes through a path length equal to one atmosphere. For zenith angles θ_z less than 60°, the AM can be calculated by the following formula:[27]

$$AM = \sec(\theta) \qquad \textbf{(5-13)}$$

When measuring solar intensity, it is important to note that radiation from the sun comes from three components: 1) diffuse radiation from scattering events, 2) reflection radiation from the local albedo, and 3) direct radiation straight from the sun. The global label, or G accounts for all three components, whereas the direct, or D (often omitted) is only the third and primary component. The average conditions for the 48 contiguous for the United States on a 37° tilted surface results in what is designated AM 1.5G with a value of 1000 W m^{-2}.[28]

5.6.2 Voltages Required for CO₂ and H₂O Splitting

In order to create a truly renewable energy source, sunlight is proposed to drive electrocatalysis either directly in PEC cells,[29] or indirectly in photovoltaic (PV) coupled bulk electrolysis.[30] For the planar PEC case the illuminated collection and electrode surface areas are equal. For the PV coupled case they are not necessarily equal and can be adjusted independently. New approaches to PEC using microwire arrays are being investigated,[31] and can relax the TOF demand by a simple geometric ratio of total electrode surface area divided by the projected surface area. In either case it is prudent to calculate the range of expected current densities from the solar flux for a given applied voltage. Two important reactions previously mentioned are water splitting and carbon dioxide splitting. These set a minimum thermodynamic voltage according to the following:

$$H_2O \rightarrow H_2 + \frac{1}{2}O_2 \quad \Delta E^\circ = 1.23V \qquad \textbf{(5-14)}$$

$$CO_2 \rightarrow CO + \frac{1}{2}O_2 \quad \Delta E^\circ = 1.33V \qquad \textbf{(5-15)}$$

where E° is the standard reduction potential in volts. The practical voltage will be higher due to system losses that can be attributed primarily due to overpotentials (η) and cell resistance (R_{cell}). The resistance will be geometry and system specific and is not considered in this perspective. With this in mind, Table 5-2 shows the relevant current densities that can be expected for a wide range of solar panel efficiencies and cell voltages. As the total η of both the anode and cathode decreases due to improved electrocatalysts, the demand on the cell voltage decreases resulting in an increase in j.

Also, as PV efficiency increases, the total amount of j increases for a given light absorber surface area. All these factors combined set upper and lower boundaries for expected current densities in a photoelectrolysis process. In Table5- 2 the j values range from 3.3 to 18 mA cm^{-2} using AM 1.5 G. It is anticipated that research will lead to more efficient PV cells and that new electrocatalysts will approach lower required voltage values. Therefore j may grow to even larger values than discussed here, and creates an even more compelling need for catalysts with higher TOF values.

5.7 COMPARISON OF HOMOGENEOUS AND HETEROGENEOUS LIMITING CURRENT

Once the relevant boundaries have been established for a solar driven electrocatalytic system, the limiting current equations derived for homogeneous and heterogeneous EC' reactions (equations 5-8b and 5-12b respectively), can be directly compared. This is shown in Figure 5-5 where the shaded box contains the solar current density boundaries from Table 5-2. Four catalyst concentrations are shown for both homogeneous and heterogeneous systems. Most reported synthetic electrocatalysts exhibit TOFs within the range of 0.01–1,000 s^{-1}, however the highest values are observed with biological anaerobic enzymatic catalysis.[32] These results are insightful in the design and application of new electrocatalysts for creating solar fuels. They illustrate the importance of matching the current supply and consumption in an electrically driven process. In the case that the TOF is slower than required, the catalysis will be the slowest

process, and will therefore be unable to consume all of the current produced at a PEC device. This will result in a decrease of the overall solar energy conversion efficiency. It is then possible to use the limiting current of the electrocatalyst to determine the TOF (as long as all assumptions are valid). In the case that the TOF is faster than required, the catalytic process will consume all of the PV current. The efficiency can only be further increased by reducing η, thus increasing the PV current by lowering the total voltage requirement as shown earlier in Table 5-2. Since the catalyst is now electron starved, the TOF cannot be derived from the above equations. If the concentration is decreased sufficiently it is possible to reenter a catalytic rate limiting region and calculate TOF by these methods. An external power source can also be used to push the catalyst to the current limit. A central goal is to increase the TOF and simultaneously reduce η. High concentrations of catalyst decrease the demands on TOF in both homogeneous and heterogeneous systems. But this approach may not always be practical. The maximum Γ_C due to the physical size/packing in the heterogeneous case, or the solubility limit for [**C**] in the homogeneous case may limit the accessible range.

5.8 CONCLUSION

In summary, homogeneous systems have both diffusional effects from the catalyst and the substrate, whereas for a heterogeneous system only the substrate is free to diffuse. By making certain assumptions the flux of the relevant electrocatalyst species can be derived for both systems. The resulting current relationships are independent of time. In

the current ranges of the solar flux, homogeneous and heterogeneous systems require a similar TOF. At current densities greater than those expected from the AM 1.5G solar flux, heterogeneous systems requires a lower TOF than the corresponding homogeneous system. In either case, if a catalyst is used that exceeds the required TOF, overpotential must be decreased the while maintaining the TOF to improve the current density and the overall efficiency.

The ability to produce fuels using CO_2 and H_2O as energy carrier precursors is an attractive solar energy storage solution. The great challenge for scientists and engineers is to drive these reactions in a sustainable process solely by captured solar energy. Homogeneous and heterogeneous electrocatalysis continues to be investigated as a potentially efficient and scalable solution. Other methods which do not have the same light absorber and electrode surface area, as in the case of PEC may yield more efficient conversion systems. Further work may also improve the technology for solar conversion efficiencies. Solar concentration may be incorporated and photovoltaic driven electrolyzer systems may be investigated as potential solutions. Each of these possibilities may result in higher current densities, and therefore increase the demand on TOF. Additional research is need for increasing the TOF, decreasing the η, all while remaining stable and yielding the desired hydrocarbon products.

5.9 ACKNOWLEDGMENTS

Chapter 5, in part, is a reprint of material that has been submitted to the Journal of Physical Chemistry C Letters, entitled, "Kinetics and Limiting Currents of Homogeneous and Heterogeneous Electrocatalytic EC' Systems for Solar Generated Fuels," written by Aaron J. Sathrum and Clifford P. Kubiak. The dissertation author was the primary investigator and author of this material.
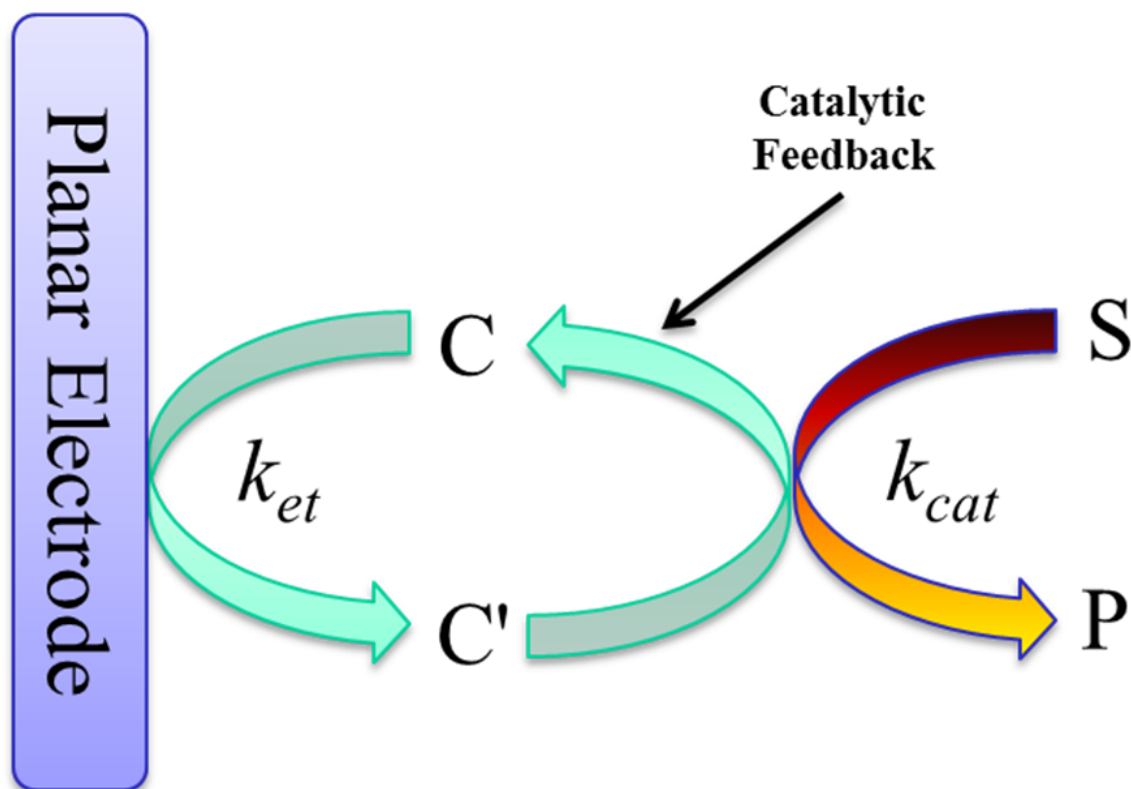
Figure 5-1 Simple scheme for a homogeneous electrocatalytic EC' system. *n* electrons are transferred from the electrode surface to the catalyst C to form C', followed by a subsequent chemical reaction of C' with the substrate S to make the product P and regenerate the catalyst precursor C.

Figure 5-2 Variations of turnover frequency with the limiting current density plotted at several homogeneous electrocatalyst concentrations, according to equation 5-8b, (n = 2, $D_C = 8.1 \times 10^{-6}$ cm^2 s^{-1}). The demand on the turnover frequency increases rapidly as the current density increases. However by increasing the catalyst concentration the TOF requirement is relaxed.

Figure 5-3 Simple scheme for a heterogeneous electrocatalytic EC' system. n electrons are transferred from the electrode to the surface bound catalyst C to form C', followed by a subsequent chemical reaction of C' with the substrate S to make the product P and regenerate the catalyst precursor C.
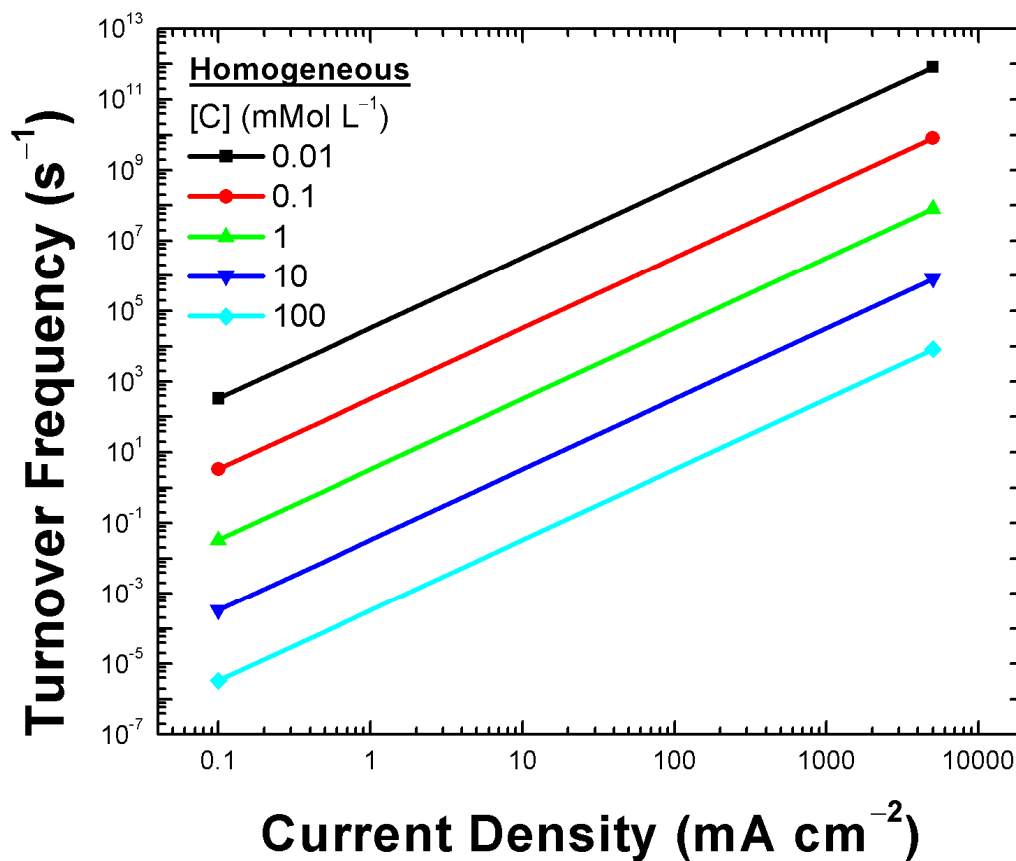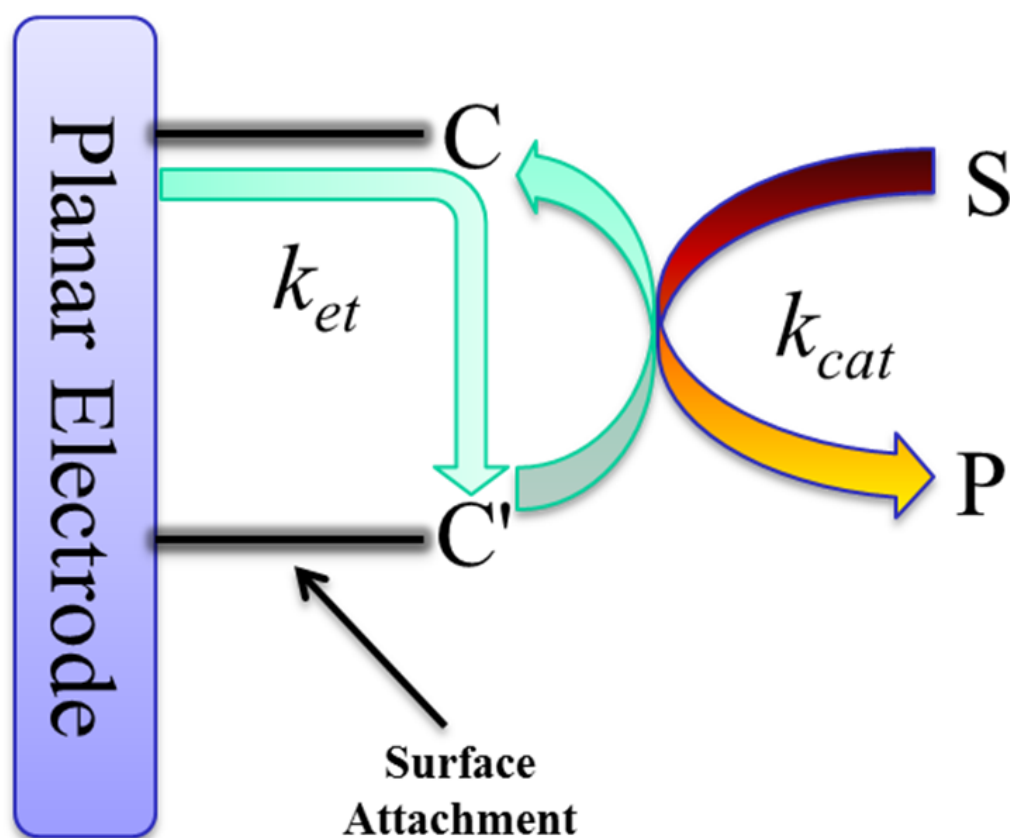
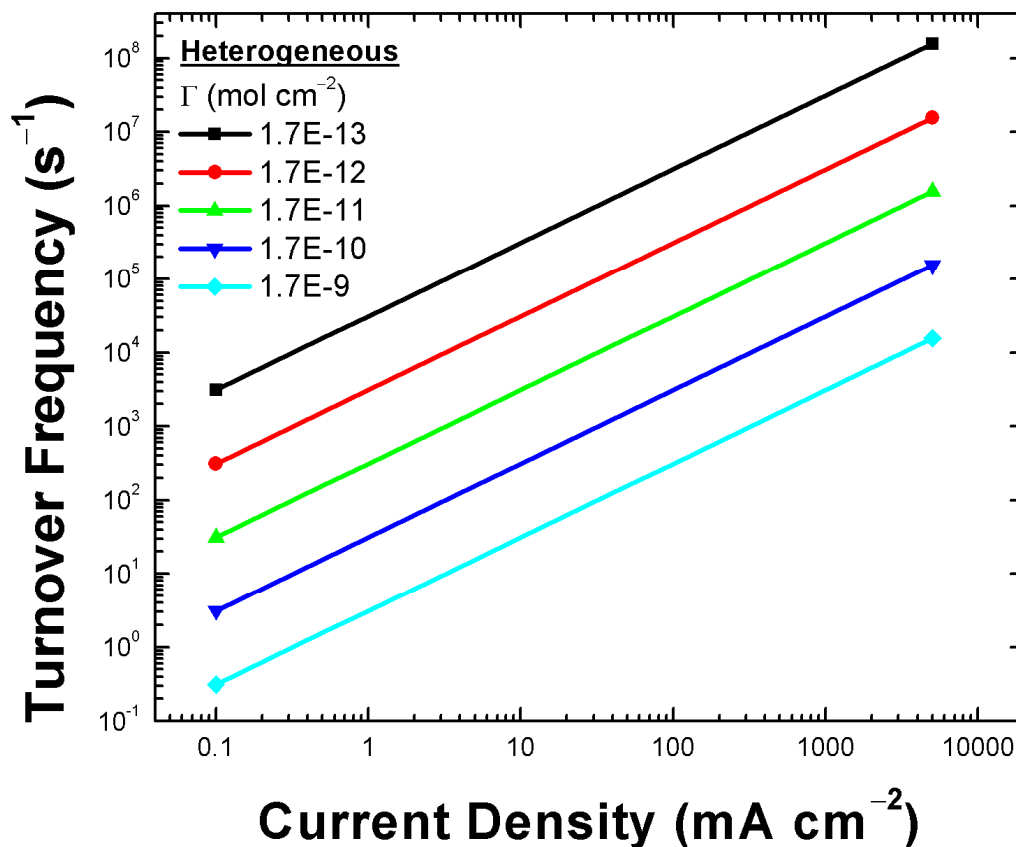**Figure 5-4** Variation of turnover frequency with the limiting current density plotted at several heterogeneous electrocatalyst surface concentrations, according to equation 5-12b, ($n = 2$). The demand on the turnover frequency increases with a slope half that of the homogeneous case. Larger catalysts decrease the possible surface coverage Γ, resulting in a higher demand on turnover frequency.

Table 5-1 Common surface concentration unit notations and relevant values[a]

Area (nm^2)	molecules cm^{-2}	mol cm^{-2}	pmol cm^{-2}
1000	1.0E+11	1.66E-13	0.166
100	1.0E+12	1.66E-12	1.66
10	1.0E+13	1.66E-11	16.6
1	1.0E+14	1.66E-10	166
0.1	1.0E+15	1.66E-09	1660
0.01	1.0E+16	1.66E-08	16600

[a] *The area is estimated from the molecular radius. This conversion assumes a 100% packing efficiency. Note, for a 2-D square or a hexagonal closed pack lattice the maximum packing efficiency is 78.5% and 90.7% for circular projections respectively.*

Table 5-2 Current density values for total applied voltage at various solar efficiencies[a]

	More efficient solar panels →					
	Thin Film		Poly–Si		c–Si	
PV Efficiency (%)	10.0%	12.5%	15.0%	17.5%	20.0%	22.5%
Voltage (V)	j, Current Density (mA cm^{-2})					
1.25	8.0	10.0	12.0	14.0	16.0	18.0
1.5	6.7	8.3	10.0	11.7	13.3	15.0
1.75	5.7	7.1	8.6	10.0	11.4	12.9
2	5.0	6.3	7.5	8.8	10.0	11.3
2.25	4.4	5.6	6.7	7.8	8.9	10.0
2.5	4.0	5.0	6.0	7.0	8.0	9.0
2.75	3.6	4.5	5.5	6.4	7.3	8.2
3	3.3	4.2	5.0	5.8	6.7	7.5

Lower η electrocatalysts ↑

[a] *Under one sun AM 1.5G peak solar flux (1000W m^{-2}), with PV area equal to the electrode area, and power matched PV operation (no voltage conversion losses) using power = current x voltage.*
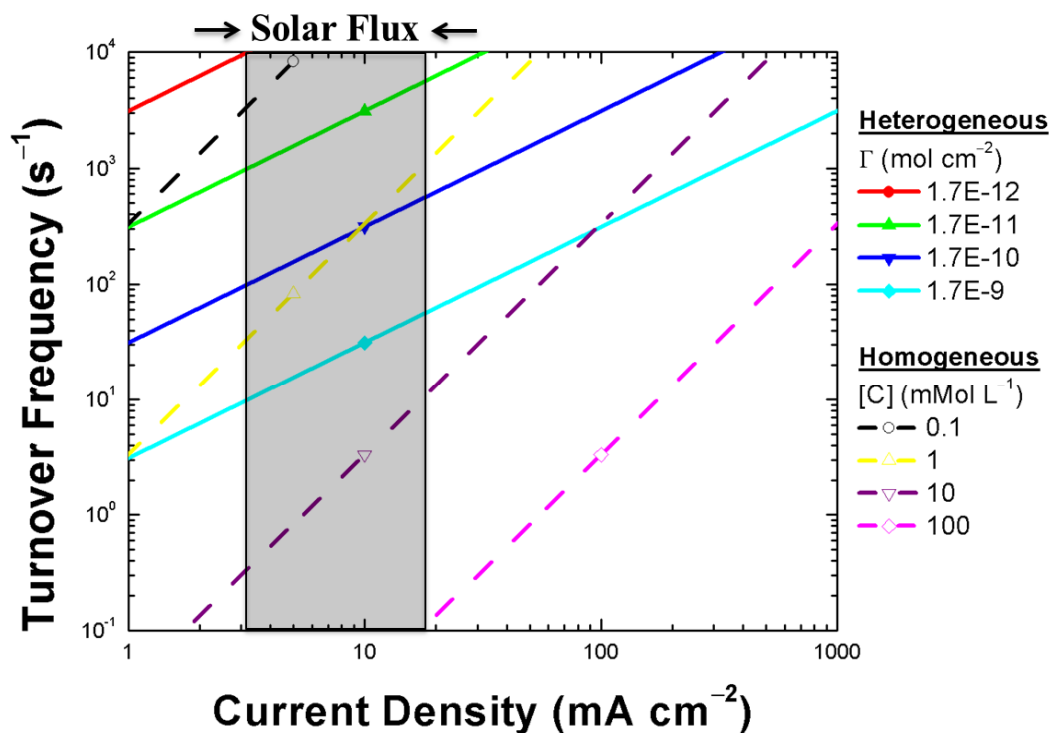
Figure 5-5 Comparison of the homogeneous and heterogeneous relationships over relevant current densities expected from the solar flux. The upper and lower boundaries of the shaded region come from Table 5-2. The demand on the TOF can be relaxed by increasing the surface or solution concentration of the system.

5.10 REFERENCES

(1)   Grunes, J.; Zhu, J.; Somorjai, G. A. Catalysis and Nanoscience. *Chem. Comm.* **2003**, 2257-2260.

(2)   Benson, E. E.; Kubiak, C. P.; Sathrum, A. J.; Smieja, J. M. Electrocatalytic and Homogeneous Approaches to Conversion of CO_2 to Liquid Fuels. *Chem. Soc. Rev.* **2009**, *38*, 89-99.

(3)   Miyasaka, T. Toward Printable Sensitized Mesoscopic Solar Cells: Light-Harvesting Management with Thin TiO_2 Films. *J. Phys. Chem. Lett.* **2011**, *2*, 262-269.

(4)   Kamat, P. V.; Tvrdy, K.; Baker, D. R.; Radich, J. G. Beyond Photovoltaics: Semiconductor Nanoarchitectures for Liquid-Junction Solar Cells. *Chem. Rev.* **2010**, *110*, 6664-6688.

(5)   Hodes, G.; Cahen, D.; Manassen, J. Tungsten Trioxide as a Photoanode for a Photoelectrochemical Cell (PEC). *Nature* **1976**, *260*, 312-313.

(6)   Heller, A. Hydrogen-Evolving Solar Cells. *Science* **1984**, *223*, 1141-1148.

(7)   Nicholson, R. S.; Shain, I. Theory of Stationary Electrode Polarography. Single Scan and Cyclic Methods Applied to Reversible, Irreversible, and Kinetic Systems. *Anal. Chem.* **1964**, *36*, 706-723.

(8)   Savéant, J. M.; Vianello, E. Investigations of the Catalytic Currents in Oscillographic Polarography with Linear Voltage Sweep. Theoretical Study. *Advan. Polayog., Proc. Intern. Congr., 2nd, Cambridge, Engl., 1959* **1960**, *1*, 367-374.

(9)   Testa, A. C.; Reinmuth, W. H. Stepwise Reactions in Chronopotentiometry. *Anal. Chem.* **1961**, *33*, 1320-1324.

(10)   Bard, A. J.; Faulkner, L. R. *Electrochemical Methods, Fundamentals and Applications*, 2nd Edition ed.; John Wiley & Sons, Inc., 2001.

(11)   Savéant, J. M. Catalysis of Chemical Reactions by Electrodes. *Acc. Chem. Res.* **1980**, *13*, 323-329.

(12)   Savéant, J.-M. Molecular Catalysis of Electrochemical Reactions. Mechanistic Aspects. *Chem. Rev.* **2008**, *108*, 2348-2378.

(13)   Hawecker, J.; Lehn, J. M.; Ziessel, R. Photochemical and Electrochemical Reduction of Carbon Dioxide to Carbon Monoxide Mediated by (2,2′-Bipyridine)tricarbonylchlororhenium(I) and Related Complexes as Homogeneous Catalysts. *Helv. Chim. Acta* **1986**, *69*, 1990-2012.

(14)   Delahay, P.; Stiehl, G. L. Theory of Catalytic Polargraphic Currents. *J. Am. Chem. Soc.* **1952**, *74*, 3500-3505.

(15)   Savéant, J. M.; Vianello, E. Potential-Sweep Chronoamperometry. Kinetic Currents for First-Order Chemical Reaction Parallel to Electron-Transfer Process (Catalytic Currents). *Electrochim. Acta* **1965**, *10*, 905-920.

(16)   Lewis, N. S. An Analysis of Charge-Transfer Rate Constants for Semiconductor Liquid Interfaces. *Annu. Rev. Phys. Chem.* **1991**, *42*, 543-580.

(17)   Cottrell, F. G. The Cut Off Current in Galvanic Polarisation, Considered as a Diffusion Problem. *Z. Phys. Chem.* **1903**, *42*, 385-431.

(18)   Smieja, J. M.; Kubiak, C. P. Re(bipy-tBu)(CO)$_3$Cl–improved Catalytic Activity for Reduction of Carbon Dioxide: IR-Spectroelectrochemical and Mechanistic Studies. *Inorg. Chem.* **2010**, *49*, 9283-9289.

(19)   Whipple, D. T.; Kenis, P. J. A. Prospects of CO_2 Utilization via Direct Heterogeneous Electrochemical Reduction. *J. Phys. Chem. Lett.* **2010**, *1*, 3451-3458.

(20)   Sucheta, A.; Cammack, R.; Weiner, J.; Armstrong, F. A. Reversible Electrochemistry of Fumarate Reductase Immobilized on an Electrode Surface. Direct Voltammetric Observations of Redox Centers and their Participation in Rapid Catalytic Electron Transport. *Biochem.* **1993**, *32*, 5455-5465.

(21)   Armstrong, F. A.; Heering, H. A.; Hirst, J. Reactions of Complex Metalloproteins Studied by Protein-Film Voltammetry. *Chem. Soc. Rev.* **1997**, *26*, 169-179.

(22)   Tender, L.; Carter, M. T.; Murray, R. W. Cyclic Voltammetric Analysis of Ferrocene Alkanethiol Monolayer Electrode Kinetics Based on Marcus Theory. *Anal. Chem.* **1994**, *66*, 3173-3181.

(23)   Otoole, T. R.; Sullivan, B. P.; Bruce, M. R. M.; Margerum, L. D.; Murray, R. W.; Meyer, T. J. Electrocatalytic Reduction of CO_2 by a Complex of Rhenium in Thin Polymeric Films. *J. Electroanal. Chem.* **1989**, *259*, 217-239.

(24)   Chen, Z.; Concepcion, J. J.; Jurss, J. W.; Meyer, T. J. Single-Site, Catalytic Water Oxidation on Oxide Surfaces. *J. Am. Chem. Soc.* **2009**, *131*, 15580-15581.

(25)   Murray, R. W. Chemically Modified Electrodes. *Acc. Chem. Res.* **1980**, *13*, 135-141.

(26)   Murray, R. W.; Ewing, A. G.; Durst, R. A. Chemically Modified Electrodes - Molecular Design for Electroanalysis. *Anal. Chem.* **1987**, *59*, 379A-390A.

(27)   Matson, R. J.; Emery, K. A.; Bird, R. E. Terrestrial Solar Spectra, Solar Simulation and Solar-Cell Short Circuit Current Callibration - A Review. *Sol. Cells* **1984**, *11*, 105-145.

(28)   Standard Tables for Reference Solar Spectral Irradiances: Direct Normal and Hemispherical on 37° Tilted Surface. *ASTM G173 - 03* **2008**.

(29)   Butler, M. A. Photoelectrolysis and Physical-Properties of Semiconducting Electrode WO_3. *J. Appl. Phys.* **1977**, *48*, 1914-1920.

(30)   Gibson, T. L.; Kelly, N. A. Predicting Efficiency of Solar Powered Hydrogen Generation using Photovoltaic-Electrolysis Devices. *Int. J. Hydrogen Energy* **2010**, *35*, 900-911.

(31)   Boettcher, S. W.; Warren, E. L.; Putnam, M. C.; Santori, E. A.; Turner-Evans, D.; Kelzenberg, M. D.; Walter, M. G.; McKone, J. R.; Brunschwig, B. S.; Atwater, H. A.; Lewis, N. S. Photoelectrochemical Hydrogen Evolution Using Si Microwire Arrays. *J. Am. Chem. Soc.* **2011**, *133*, 1216-1219.

(32)   Jeoung, J.-H.; Dobbek, H. Carbon Dioxide Activation at the Ni,Fe-Cluster of Anaerobic Carbon Monoxide Dehydrogenase. *Science* **2007**, *318*, 1461-1464.